Overview Experimental Diagnostics for Rarefied Flows – Selected Topics

Stefanos Fasoulas, Georg Herdrich, Stefan Löhle
Institute of Space Systems (IRS)
University of Stuttgart
Pfaffenwaldring 31
70569 Stuttgart, Germany

fasoulas@irs.uni-stuttgart.de

ABSTRACT

This article gives an overview about experimental diagnostic techniques for the investigation of rarefied flows with a special focus on techniques applicable to high-enthalpy flows occurring e.g. in electrical thrusters or plasma wind tunnels. Classical intrusive techniques like Pitot, heat flux, and enthalpy probe as well as mass spectrometry are introduced as well as non-intrusive methods like emission and absorption spectroscopy and laser-induced fluorescence (LIF) measurements. Here, main emphasis is laid on the methods applied at the IRS in order to illustrate the methods by sample results.

1.0 INTRODUCTION

The dream of every scientist and engineer dealing with rarefied, usually high-enthalpy and non-equilibrium flows is a (preferably single) diagnostic method capable to measure the distribution functions of every single degree of freedom (translational and internal, including excitation) for each appearing species, including eventually ions and electrons, and, of course, at every local position and at every time. If this method existed, the huge efforts spent for the theoretical and numerical simulation of such flows would most probably be obsolete, except maybe for cost reasons. Unfortunately (or fortunately), this method does not exist. The available techniques, the keys to the secrets of rarefied flows, give us just some selected, in most cases macroscopic information about temperatures, species, heat fluxes, etc. Many of these measurement data give therefore simply some macroscopic information about the occurring effects and often one has to solve a so-called inverse problem in order to achieve some insight into the origins of these phenomena. In addition, many methods require some assumptions about the distribution of the energy into the different degrees of freedom or in some cases also about the certain distribution function itself. As the nature of rarefied flows shows in the most interesting locations a more or less stronger deviation from an equilibrium Maxwellian distribution function, these assumptions may lead to significant systematic measurement errors.

This article intends to give a first overview about these “keys” to the secrets of rarefied flows, with emphasis given to the methods developed and applied at the IRS, especially designed for the characterisation of flows produced by electrical thrusters and within the plasma wind tunnels for re-entry simulation. A similar article has been presented in [2] – here, some additions concerning newly developed methods and strategies are summarized.

For engineering purposes it is in many cases sufficient to obtain the information about the distribution of the available energy into the different degrees of freedom, i.e. one has to measure as much as possible values incorporated in the equation

$$\underbrace{h_{tot}}_{\text{total enthalpy}} = \underbrace{\frac{1}{2}v^2}_{\text{kinetic}} + \underbrace{\sum_i \xi_i c_{p,i} T_i}_{\text{thermal}} + \underbrace{\sum_i \xi_i h_i}_{\text{chemical}} + \underbrace{\sum_i \xi_i h_{el,i}}_{\text{ionised}} \quad , \tag{1}$$

where h_{tot} denotes the total enthalpy, v the macroscopic velocity, ξ_i the mass fraction, $c_{p,i}$ the specific heat capacity, and T_i the temperature of species i, respectively. An overview about some of the available methods assigned to their measurement focus is given in Fig. 1. Generally, the tools can be divided into intrusive and non-intrusive methods. Some of them (shadowed) are briefly introduced in the following sections.

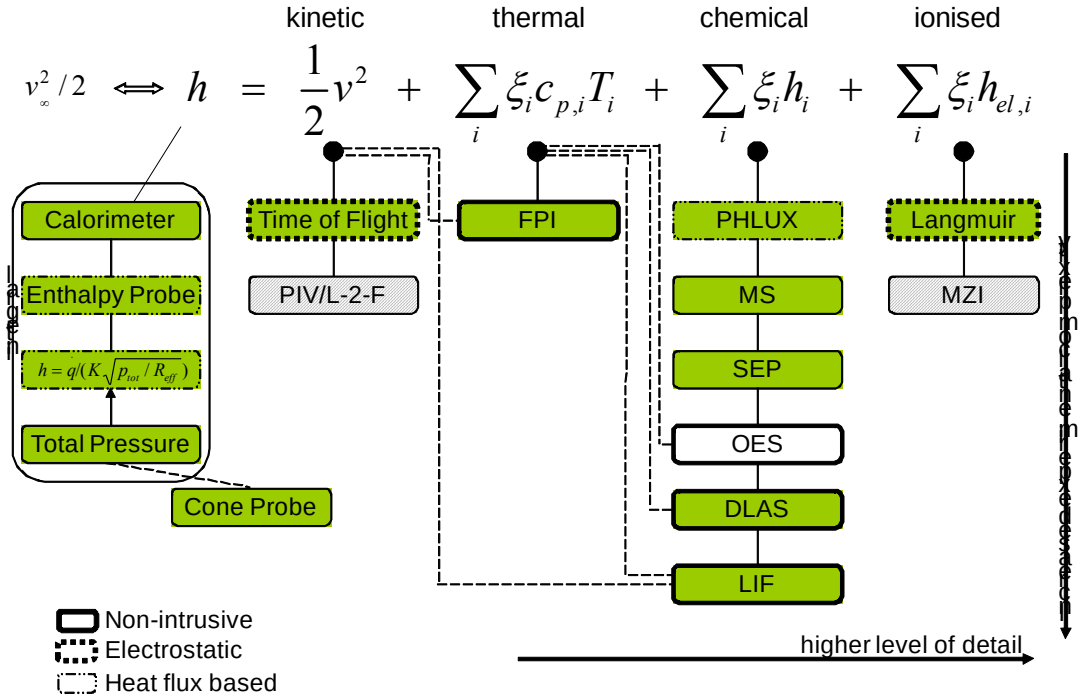

FPI: Fabry-Perot-Interferometry
L-2 F: Laser 2 Focus
MS: Mass Spectrometry
OES: Optical Emission Spectroscopy
LIF: Laser-Induced Fluorescence
PIV: Particle Image Velocimetry
PHLUX: Pyrometric Heat Flux
SEP: Solid Electrolyte Probe
DLAS: Diode Laser Absorption Spectroscopy
MZI: Mach-Zehnder-Interferometry

Figure 1: Overview experimental methods and their applicability.

2.0 INTRUSIVE MEASUREMENT TECHNIQUES

Mechanical probes, mass spectrometry, and electrostatic probes belong to the group of intrusive measurement techniques. They are all suitably constructed probes being mounted in the stream to be investigated. This differs from the optical measurement techniques which are described in the next section.

Probes applied at the IRS can essentially be divided into their measurement goal, i.e.

- Pressure probes for total and static pressure
- Aerodynamic wedge probes for static pressure and Mach number in supersonic flows
- Heat flux probes
- Enthalpy probes
- Solid-state electrolyte probes for oxygen partial pressure
- Mass spectrometry for species densities and energy distribution
- Electrostatic probes for plasma potential, electron density, temperature and energy distribution, ion temperature, flow velocity and direction
- Radiometer probes for radiation heat flux

In practice, these supposedly simple measurements techniques are already very difficult. A more or less complex theory is hidden between determining the basic parameters and ascertaining the parameters which are actually of interest, especially in the case of enthalpy and heat flux. A brief overview of each technique is given in the following.

2.1 Pressure Probes

With Pitot probes it is possible to measure the dynamic or total stagnation pressure of the flow by connecting them either to a differential pressure gauge inside or to a total pressure gauge outside of the vacuum tank. Fig. 2 depicts the 'spherical head' Pitot probe which has an identical geometry as a material support system used for the investigation of candidate thermal protection materials, and Fig. 3 a miniaturized probe which is used for local measurements at very high heat fluxes of more than 10 MW/m^2, e.g. also in electrical thrusters [3].

When using Pitot probes, one must generally differentiate between two cases: measurement in a subsonic or a supersonic flow. In the first case, the conditions are relatively simple. The Bernoulli equation is valid whereby the simple equation

$$p_0 = p_\infty + \frac{\rho_\infty}{2} v_\infty^2 \tag{2}$$

at Mach numbers of $Ma > 0.3$ must be replaced by the Bernoulli equation for compressible flows. If friction effects are neglected and assuming that the changes in the condition run lengthwise isentropically along the lines, the following connection exists between the flow parameters:

$$p_0 = p_\infty \left(1 + \frac{\kappa - 1}{\kappa} \frac{\rho_\infty}{p_\infty} \frac{v_\infty^2}{2} \right)^{\frac{\kappa}{\kappa - 1}} , \tag{3}$$

whereby κ means the averaged adiabatic exponent, p_0 represents the pressure in the stagnation point and p_∞, ρ_∞, v_∞ the quantities of the undisturbed flow. With that one can, for example, deduce the density from the pressure measurement when the speed and κ are known.

In supersonic flows a compression shock forms in front of the probe which results in a loss of total

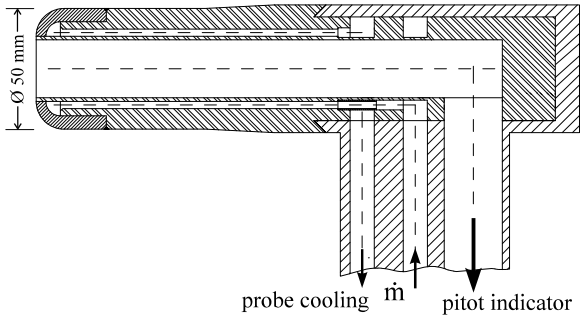

Figure 2: 'Blunt' Pitot probe.

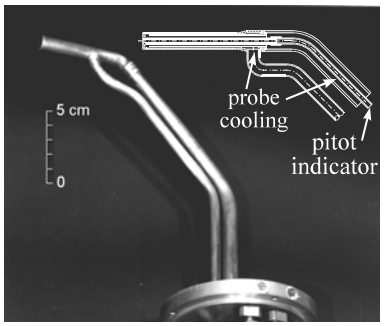

Figure 3: Miniaturized Pitot probe.

pressure. The probe measures the total pressure p_0 after the shock. Assuming that the compression shock runs perpendicular to the initial direction of flow and the changes in the condition run isentropically in front of and behind the shock, then the following is valid for p_0:

$$p_0 = \frac{\kappa - 1}{2} Ma^2 \left[\frac{(\kappa+1)^2 Ma^2}{4\kappa Ma^2 - 2(\kappa - 1)} \right]^{\frac{1}{\kappa - 1}} p_\infty \quad . \tag{4}$$

Here Ma is the Mach number in front of the shock and κ, on the other hand, is the averaged adiabatic exponent. If the Mach number is additionally determined, e.g. with a wedge probe, then the average adiabatic exponent can be calculated from this last equation.

The equations presented so far are derived under the assumption of a continuum flow. A variety of error sources can then be identified if the flow shows a strong deviation from thermodynamic equilibrium or as soon as rarefaction becomes dominant. Among those source are for example:

- Thermal diffusion effect: High temperatures near the probe bore hole can affect the pressure by thermal diffusion. However, most probes are fully cooled and wall temperatures can be expected to be below 350 K due to the very high heat conductivity of the material (usually copper).
- Fluctuations: So far, no attempt has been made as the information is too uncertain. Similar situations can be considered for the acoustic response of the measurement system (the probe, tubing, and pressure gauge volume). No analysis of this effect is possible for supersonic turbulent flow. Estimates give a potential error in the order of 10% as a border line [1].
- Viscous and rarefied flow effects: The total pressure measurements are affected by low density or low probe Reynolds numbers. Correspondingly, corrections are often given as semi-empirical relations that either depend on the Knudsen number or on the Reynolds number. To distinguish between the continuum application and the rarefied flow case, the probe is then named Pattarson-probe, indicating also that other equations are valid than the abovementioned.

The latter of the mentioned effects is a decisive parameter for the measurement of Pitot pressure. For the analysis with respect to the significance of viscosity, the Knudsen number Kn or the Reynolds number is often used. The former describes the ratio of mean free path λ of the flow particles and a characteristic length L of the measurement problem, such as the bore hole diameter. However, many authors do not distinguish between different probe designs i.e. different probe geometries such as spherical or cylindrical and the dependence on the Mach number is not reported. A deeper analysis with respect to an analysis of the significance of probe geometry is made in [1]. For understandable reasons the authors switch to a depiction depending on the Reynolds number. The general outcome is that there is a wide spreading of data as the relation now depends on Reynolds and Mach numbers. Simultaneously, the data vary due to the differences in probe geometry.

2.2 Heat Flux, Catalysis and Enthalpy Probes

Heat transfer to a body exposed to high-enthalpy, plasma flow is of special interest for re-entry simulation. However, for the heat flux measurement the material of the probe itself is also important because the heat transfer may vary depending on the catalytic activity of the surface material. Also, the surface temperature of the probe may change the result since it affects the recombination rate and the emission coefficient. Copper is mostly used as a standard reference material for heat flux probes as it has a relatively high catalytic efficiency. However, it is not an ideal material because in an oxidizing atmosphere it forms different oxides with different catalycity leading to an almost unpredictable amount of the chemical energy portion which is converted to measurable heat flux. Indeed, even with a relatively high catalytic efficiency of the surface, it is not guaranteed that the equivalent "fully catalytic" heat flux is measured under all conditions.

Both, stationary and transient heat flux measurement devices are used at the IRS (Figs. 4-5). The actual probes are inserts in the front plate of a water-cooled support system, consisting of either a water-cooled tube or a Gardon Gauge for stationary or a heat sink slug for transient measurements. The probes can be coated and the slug can be made of copper or other materials like tungsten or SiC to investigate the influence of the surface catalytic activity [5, 6].

2.2.1 Stationary Heat Flux Measurement

Two different principles are in use for stationary heat flux measurement: Calorimetric and Gardon gauge probes. With the calorimetric method the heat flux to a water-cooled, relatively cold surface is measured (Fig. 4). From the heat which is carried off by the cooling water, one obtains the heat flux $\dot{q}$ onto the front surface A_s by measuring the temperature difference ΔT between the in- and outlet of a cooling mass flow rate $\dot{m}_c$ with a specific heat capacity c_c according to

$$\dot{q}=\frac{\dot{m}_c}{A_s}c_c\Delta T \ . \tag{5}$$

While operating the probe, the cooling flow rate should be high enough to guarantee sufficient cooling but low enough to keep the temperature difference between the in- and outlet in a measurable level.

With the other method, the Gardon gauge named after its inventor Robert Gardon, the heat flux is determined from the temperature gradient which forms between the centre and the edge of a circular foil. It consists of a heat sink in form of a hollow cylinder usually made of copper and a foil attached to the front side typically made of constantan. The constantan foil is connected with a copper wire in the centre (Fig. 6). If the heat sink is kept at a constant temperature, for example by embedding it in a water-cooled sample, a radial temperature drop forms on the foil. Assuming that the front and back sides of the foil do not release any heat and that temperature gradients across the thickness s of the foil are negligible, the following equation results from the parameters depicted in Fig. 7 for stationary temperature distribution:

$$\frac{\dot{q}}{s\lambda}+\frac{1}{r}\frac{dT_{stat}}{dr}+\frac{d^2T_{stat}}{dr^2}=0 \ . \tag{6}$$

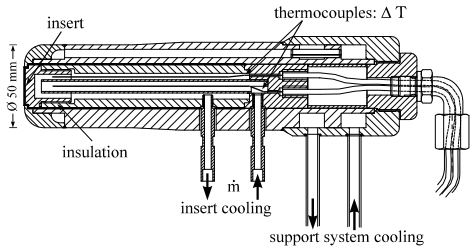

Figure 4: Stationary heat flux probe.

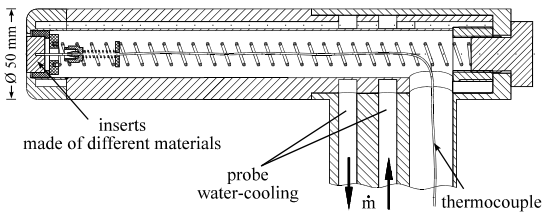

Figure 5: Transient heat flux probe.

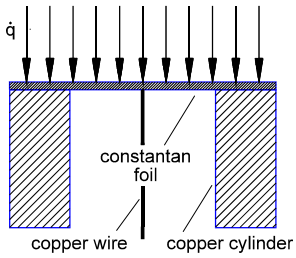

Figure 6: Gardon gauge setup.

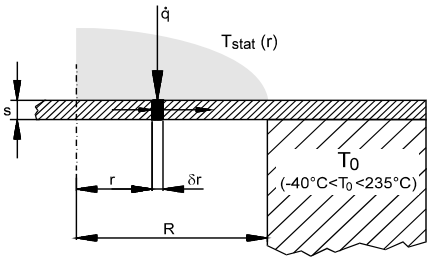

Figure 7: Geometric relations.

Here T_{stat} is the stationary temperature of the foil at the radius r and λ is the heat conductivity of the foil. Because the heat conductivity increases linearly with temperature according to $\lambda = \lambda_o\left(1+\alpha\left(T-T_o\right)\right)$, the solution of the above differential equation is

$$\Delta T\left(1+\frac{\alpha}{2}\Delta T\right)=\dot{q}\frac{R^2}{4\lambda_0 s} \quad , \tag{7}$$

where ΔT represents the temperature difference between the centre and the edge of the foil. With the values for λ_0 and α one obtains for constantan:

$$\dot{q}=\frac{1}{2026.25}\frac{s}{R^2}\Delta T\left(1+0.00115\Delta T\right) \quad \left[\frac{W}{m^2}\right]. \tag{8}$$

The dependence of the temperature difference on the heat flux to be measured is obviously not linear. This disadvantage can, however, be compensated because two thermal element transitions form in the center and at the edge of the foil where the copper cylinder or rather the wire and the constantan foil are connected. The temperature difference calculated above exists between the two contact points leading to a resulting thermal voltage which can be expressed for a copper-constantan combination by

$$U=0.0381\Delta T\left(1+0.00117\Delta T\right) \quad \left[mV\right]. \tag{9}$$

The figures in brackets of the last two equations are practically identical so that the measured thermal voltage becomes directly proportional to the heat flux:

$$U\approx 77.2\frac{R^2}{s}\dot{q} \quad \left[mV\right] \quad . \tag{10}$$

An advantage of the Gardon gauge is the compact design. The dimensions are usually only a few mm in diameter so that several sensors can easily be integrated into a probe. Also, the response times are very short so that fast heat flux fluctuations can be detected.

At the IRS, these heat flux sensors are equipped with surface layers of different materials to study catalytic effects. However, the reduction of the heat flux from measured data is not as easy as for the copper-constantan case anymore.

2.2.2 Transient Heat Flux Measurement

If one avoids a radial heat transport as in the stationary case, the axial heat flux can be calculated from the one-dimensional Fourier equation

$$\frac{\partial T}{\partial t}=a\left(\frac{\partial^2 T}{\partial x^2}\right) \quad . \tag{11}$$

The boundary conditions, with x denoting the distance from the surface in axial direction, are

$t < 0$: temperature of the probe = $T_{w0} = const.$, heat flux $\dot{q} = 0$ (12)

$t > 0$: $T=T(x,t)$, $T(x=0, t) = T_w(t)$. (13)

Two different methods, the thin wall and the thick wall method exist. They differ from each other in the realization of the necessary boundary conditions.

With the thin wall method the heat flux is assumed to be constant throughout the entire thickness of the probe, i.e.

$$\dot{q}_{x=0}=\dot{q}_{x=s} \quad . \tag{14}$$

The solution to the Fourier equation can then be simplified for Fourier numbers $Fo = \frac{at}{s^2} > 0.3$. If the temperature rise is measured, the heat flux can thus be directly determined by

$$\dot{q}=\rho c_p s\frac{dT}{dt} \quad . \tag{15}$$

The ρ and c_P represent the density and specific heat capacity of the material, respectively. With a probe body made of copper with a thickness of 10 mm, the condition $Fo > 0.3$ is for example fulfilled after a measurement time of $t_{min} > 0.27$ s. Although the theory of the non-stationary thin wall method neglects heat fluxes in a radial direction, in practice this condition cannot be completely fulfilled. A simple estimate shows, however, that these heat fluxes do not interfere with the measurement as long as the heating of the body does not last longer than a certain maximum time t_{max}:

$$t_{\max} << \left| \frac{\dot{q}}{\frac{d\dot{q}}{dy}_s} \right| \frac{s^2}{a} \quad . \tag{16}$$

With the non-stationary thick wall method one assumes that the temperature on the back side of the sample body does not rise during the measurement. The solution to the Fourier equation while keeping this boundary condition in mind is then

$$\dot{q}(t)=\sqrt{\frac{\rho c_p \lambda}{\pi}}\left[\frac{T(t)}{\sqrt{t}} + \frac{1}{2}\int_0^t \frac{T(t)-T(\tau)}{(t-\tau)^{3/2}} d\tau\right] \quad . \tag{17}$$

Assuming that the heat flux is constant over time, the solution to the Fourier equation for this case is

$$T(x=0,t)-T_{w0}=\frac{2}{\sqrt{\pi}}\dot{q}\sqrt{\frac{t}{\rho c_p \lambda}} \quad . \tag{18}$$

In contrast to the thin wall method, there is no demand for a minimum test time t_{min}. On the other hand, it is only valid as long as the temperature increase has not spread over the entire measurement element. That is $T(\infty,t)$ is no longer equal to T_{w0}.

The thin wall method requires the knowledge of the material constants ρ and c_p only, whereas the thick wall method needs also the heat conductivity λ of the sample body. Because this parameter is very difficult to determine, it can be viewed as a disadvantage. On the other hand, the thick wall method offers the possibility to measure the entire profile at once while passing through the stream because the heat flux $\dot{q}(t)$ can be calculated from the temperature-time dependency. This is impossible with the thin wall method, where an existing profile must be detected by individual measurements at various positions.

A recently developed new method of heat flux measurements based on the solution of the inverse heat conduction problem uses the basic principle of automatics and control that a source leads to a measurable

result depending on a distinct transfer function. For the inverse heat conduction problem this transfer function is based on non-integer derivatives [68]. The source for the measurable signal is the net surface heat flux. The measurable signal is the temperature of an in-depth sensor. For many known problems, e.g. semi-infinite, cylindrical, spherical, the transfer function is of the following form:

$$\sum_{L_0=0}^{L} \alpha_n \mathrm{D}^{n/2} V(t) = \sum_{M_0=0}^{M} \beta_n \mathrm{D}^{n/2} \varphi(t) \text{ , avec } \alpha_0 = 1 \qquad (19)$$

For many applications, this equation holds, too. And it turned out that only very few parameters (the order of 5) are needed to characterize a sensor system. The parameters α_n and β_n are identified during a calibration step. This is realized using known heat fluxes provided by diode laser systems [69, 70]. The method is therefore based on non-integer system identification (NISI) giving the name for this heat flux method. The following two figures show a miniaturized NISI heat flux probe and a calibration measurement.

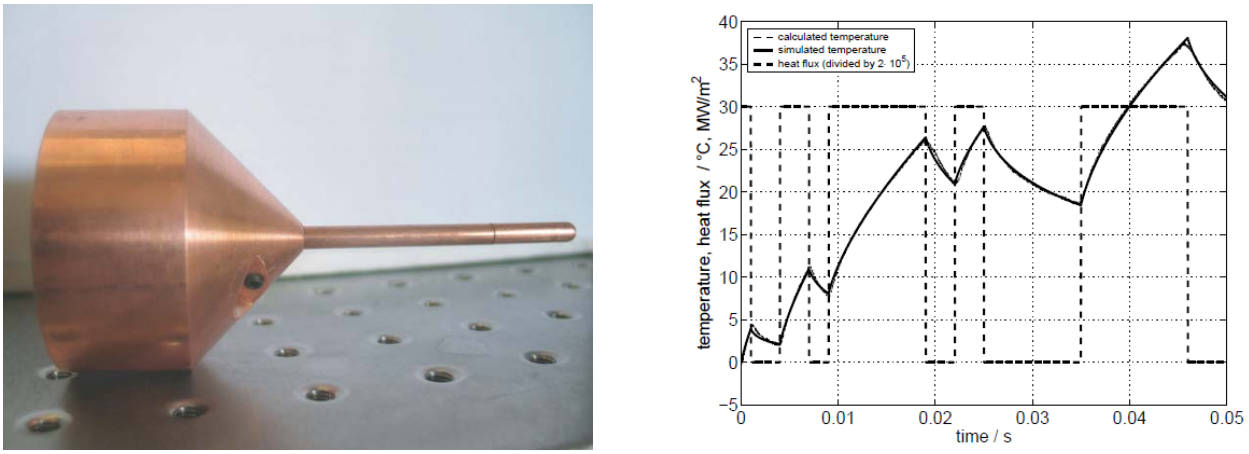

Figure 8: Miniaturized heat flux sensor based on the Non-Integer System Identification (NISI) Method (left) and calibration data of the sensor (right) [71]

2.2.3 Influence of Surface Catalycity on Heat Flux Measurements

Apart from uncontrolled heat losses, there is a far more important factor which can considerably influence the heat flux measurement results: the surface catalycity of the sample.

The heat flux on a sample in a dissociated gas (while neglecting the radiation portion) which is not chemically balanced consists of two parts joined together. The first part is supplied by the normal, molecular heat conductivity. The second forms when atom pairs recombine directly on the surface. Hence, they release some of their recombination energy to the sample. The quantitative relationship between the two parts, heat conductivity and recombination, depends on the duration that the recombination partners are in the boundary layer. If the potential reaction partners need a longer time for their way to the sample surface than the time needed for the recombination reaction, then a *balanced boundary layer* exists. In this case, the surface catalycity is not important because the particles already recombine in the flow releasing their recombination energy to the gas mixture. The surface catalycity becomes important as soon as a more or less *frozen boundary layer* prevails. Then, the recombination time is much longer than the diffusion time through the boundary layer. All potential reaction partners enter therefore the boundary layer and reach the surface of the sample. If the nature of the surface encourages recombination (heterogeneous catalysis), then the reaction energy will be released directly on the surface and the heat flux will increase. However, if the surface is not conducive to recombination, then the particles leave the boundary layer again without any reaction. This characteristic is quantitatively expressed by the so-called recombination coefficient of a material γ. Here $\gamma = 1$ means that all of the atoms impinging on the surface will recombine

(fully catalytic behaviour), and $\gamma = 0$ a non-catalytic behaviour).

As an example, Fig. 9 depicts the results of heat flux measurements that were performed with probes made of different materials. The surface catalycity can increase the heat flux by more than a factor of 2!

Based on the heat flux difference and a characterization of the plasma to a maximum extend, boundary layer models can then be used to derive the recombination coefficient γ. For the stagnation point situation even algebraic models such as the boundary layer model of Goulard [15] can then be used [16]. The characterization of the material requires however a good knowledge of other material properties such as heat conductivity or emissivity in order to enable an adequate assessment of the heat flux information at relevant wall temperatures. This is eventually needed as the recombination itself is a strong function of the temperature. In contrast to Fig. 9, wherein the depicted heat flux was measured calorimetrically with cold walls, Fig. 10 depicts results for heat fluxes derived from probes equipped with a pyrometer that allow the derivation of the heat flux at relevant wall temperatures.

Clearly, the significance of such data has to be considered carefully also if the methodology of determining catalysis is concerned. A review of relevant methodologies concludes that a data base type assessment of the available methodologies and the respective data is needed in order to consider systematic differences in the data [18]. With the data obtained at IRS, an inverse method was developed, qualified and applied that makes use of the heat flux differences on materials with different but known catalytic activity in order to determine the degree of dissociation degree. This led to the development and flight qualification of PHLUX (Pyrometric Heat fLUx eXperiment) for the ESA capsule EXPERT [18]. Besides the proof of concept of this system a comparison with data from plasma probes, diode laser absorption spectroscopy and laser induced fluorescence was performed successfully [19].

2.2.4 Enthalpy Measurements

Two different enthalpy probes are used depending on the pressure level at IRS. In one case it is tried to suck out the boundary layer of a high-enthalpy flow and in the other case a cooling gas is injected. In addition to this, the specific enthalpy is calculated from the heat flux and total pressure measurements.

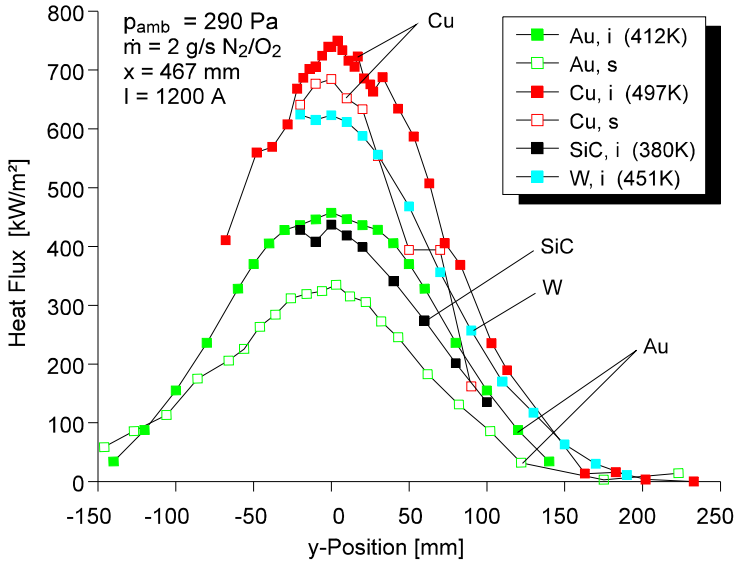

Figure 9: Results of heat flux measurements with various samples

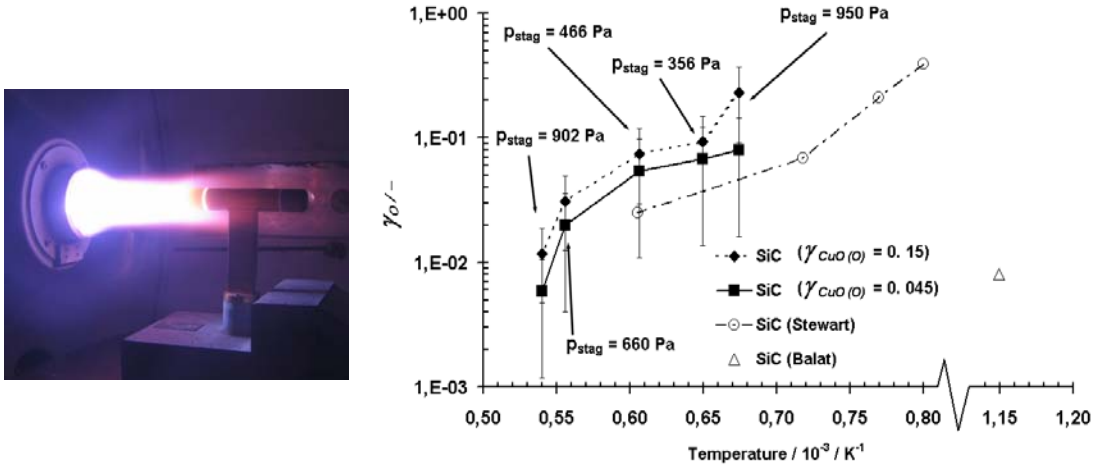

Figure 10: Catalysis probe to derive heat flux at relevant wall temperatures in operation (left) and recombination parameter for candidate materials (right) [17].

If the total pressure is high enough, then the local specific enthalpy and the local mass flow rate of a supersonic flow can be determined by suctioning out mass using the probe shown in Fig. 11. The mass flow which corresponds to the probe opening is suctioned out by a pump and the mass flow rate $\dot{m}_g$ and the gas temperature $T_{g,2}$ at the end of the probe and consequently the total enthalpy of the gas can be determined. The suction power has to be adjusted so that the compression shock which forms in front of the probe is perpendicular to the inlet opening so that a mass escape or additional in-flow is avoided. The amount of heat which is carried off by the cooling water is measured with and without suction allowing thus to determine the amount of heat extracted from the gas flow by the difference. The energy balance reads

$$\dot{m}_g h_{t,1} = \dot{m}_W c_W \left(T_{W,outflow} - T_{W,\inf\,low}\right)\big|_{V.open} - \dot{m}_W c_W \left(T_{W,outflow} - T_{W,\inf\,low}\right)\big|_{V.closed} + \dot{m}_g c_p T_{g,2}\,. \qquad (20)$$

Thus, the unknown total enthalpy $h_{t,1}$ can be obtained. Errors appear as soon as the specific enthalpy and thus the suction speed are very high. Furthermore, within low pressure conditions problems arise with a very low mass flow rate and with a certain minimum pressure difference needed for the pump.

Instead, the mass injection enthalpy probe, which has been developed at the IRS [7, 8], can also be used for flows at low pressures. The measurement principle is based on the reduction of the heat flux to the wall due to mass injection through the surface of the probe (Fig. 12).

The surface heat transfer in a viscous non-equilibrium high enthalpy flow is for this case obtained by

$$\dot{q}_w = \underbrace{\left(\lambda \frac{\partial T}{\partial y}\right)_W}_{conduction} + \underbrace{\left(\rho D_{12} \sum_i h_i \frac{\partial c_i}{\partial y}\right)_W}_{diffusion} + \underbrace{\dot{q}_R}_{radiation}\,, \qquad (21)$$

where the heat flux due to radiation is often negligible. Now, a mass injection through the wall into the boundary layer influences the layer and the transferred heat flux. It leads to a decrease of the temperature gradient on the surface and therefore to a decrease of heat flux due to conduction. Indeed, when the injection rate is high enough, the viscous layer is blown completely off the surface, and the aerodynamic convective heat transfer becomes zero. Theoretical investigations by solving the transformed Navier-Stokes equations in the boundary layer show that the heat flux $\dot{q}$ in the stagnation point of the body is dependent on the mass flow of the cooling gas which is emitted and can be expressed over a wide range of operations by

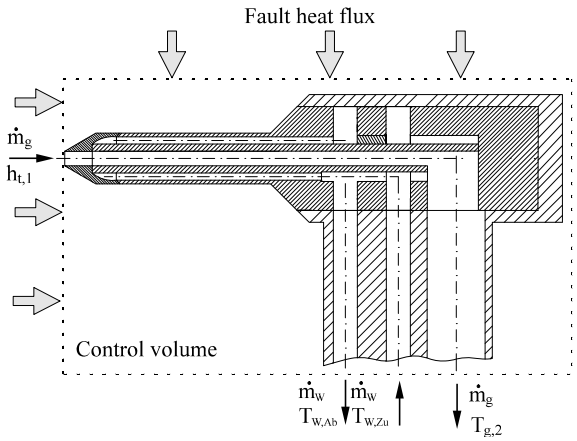

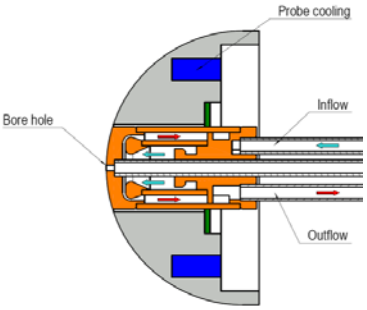

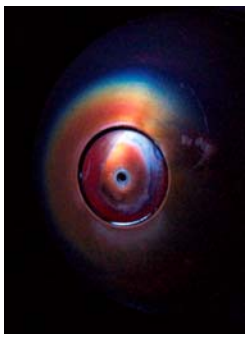

Figure 11: Set-up of a mass suction enthalpy probe.Figure 12: Set-up of a mass injection enthalpy probe.

$$\frac{\dot{q}}{\dot{q}_0} = 1 - 0.72B + 0.13B^2 \tag{22}$$

with the so-called mass addition factor B

$$B = \frac{\rho_w v_w}{\rho_\infty v_\infty St_0} = \frac{\rho_w v_w}{\dot{q}_0}\left(h_\infty - h_w\right) . \tag{23}$$

Here $\dot{q}_0$ is the heat flux and St_0 is the Stanton number without the cooling gas mass flow. The Stanton number is defined as the relation between the heat flux which appeared and the maximum possible heat flux:

$$\mathrm{St}_0 = \frac{\dot{q}_0}{\rho_\infty v_\infty \left(h_\infty - h_w\right)} \quad . \tag{24}$$

Another investigation leads to nearly identical results by solving the viscous shock layer equations [9]. By varying the specific mass flow rate $\rho_w v_w$ and measuring the heat flux ratio $\dot{q}/\dot{q}_0$ the enthalpy can be determined from the equation system above in the following way graphically: The heat flux to the probe is measured by varying the cooling mass flow rate. Then the heat flux ratio $\dot{q}/\dot{q}_0$ is plotted against the mass addition factor B as shown in Fig. 14. Adjusting this curve to the theoretical, leads then to the unknown enthalpy difference. Figure 14 shows the result of such a regression calculation for various positions in the plasma stream. It is noticeable that from a mass addition factor of B ≈ 1.2 onward a sudden deviation of the measurements appears. Numerical simulations have shown that at this point the emission speed of the cooling gas reaches sonic speed. Here, effects obviously appear that cannot be explained by the theory applied. However, this is not really important for determining the specific enthalpy because the upper portion of the curve is sufficient for the regression analysis.

The local distribution of the specific enthalpy can also be determined from measurements of the local heat flux and total pressure distribution. For this purpose, Fay and Riddell [10] reformed the laminar boundary layer equations for chemically reactive flows. By comparing with experimental results, semi-empirical equations could be formed for the following three cases:

- boundary layer in chemical equilibrium (independent from the surface catalycity),
- frozen boundary layer with a fully catalytic surface,
- frozen boundary layer with a non-catalytic surface.

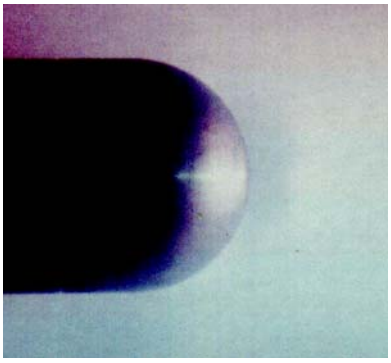

Figure 13: Cold boundary layer.

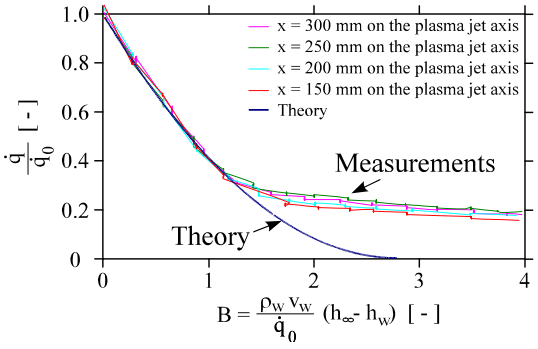

Figure 14: Enthalpy determined by adjusting the measurement curve to the theoretical.

As an example, the equation for the heat flux on a fully catalytic surface is given by

$$\dot{q}_{fc} = 0.763 \mathrm{Pr}^{-0.6} \left(\frac{\rho_w \mu_w}{\rho_\infty \mu_\infty}\right)^{0.1} \sqrt{\rho_\infty \mu_\infty \beta} \left(h_\infty - h_w\right) \left[1 + \left(\mathrm{Le}^{0.63} - 1\right)\left(\frac{h_D}{h_\infty}\right)\right]. \tag{25}$$

Thus, the local enthalpy in the flow h_∞ can in principle be determined by measuring the local heat flux. However, the density ρ_∞, viscosity μ_∞, dissociation energy h_D, Prandtl number Pr, Lewis number Le and velocity gradient β at the stagnation point have to be known as well.

In the case of a chemically frozen flow, an approximate solution is given in literature [13], which only requires the Pitot pressure and the heat flux to be known in order to calculate the enthalpy, i.e.

$$h_\infty = \frac{\dot{q}_{fc}}{K \sqrt{\frac{p_{tot}}{R_{eff}}}} \quad . \tag{26}$$

Here K is a constant which is given with a value K = 108 W/(MJ/kg bar$^{0.5}$ m$^{1.5}$) for nitrogen, R_{eff} is the effective leading edge radius of the probe which can be estimated to $R_{eff} = 2.9\ r_N$ (r_N: real leading edge radius) for the relatively low Mach numbers in the plasma wind tunnels. Here $\dot{q}_{fc}$ represents the fully catalytic heat flux. For copper up to a specific enthalpy of approximately 50 MJ/kg it can be calculated from the actual heat fluxes $\dot{q}_{fc}$ with the help of measurements from Pope [14] and Goulard [15]. However, it should be noted that, considering all the simplifications, this method serves just as an estimation of the specific enthalpy.

2.3 Mass Spectrometry

Mass spectrometry allows in principle the determination of particle densities and energy distributions of neutrals and ions in a free stream plasma. At IRS, it has been used to determine the plasma flow composition [20, 21] as well as to investigate the erosion behavior [22, 23] and catalytic effects [5, 24] of typical heat protection materials.

The mass spectrometer used at the IRS is based on a VG Quadrupole [25] SXP300/CMA500 and consists of an open electron impact ion source, a cylindrical mirror energy analyzer (CMA, 0 - 50 eV), a triple filter quadrupole (0 - 300 amu) and a channeltron (Fig. 15). An ion transfer optic (ITO) is installed in front of the ion source, a small aperture lens, with which external ions can be focused into the CMA while the ion source is switched off. In the case where neutrals are detected, a reflecting potential for positive ions is applied to the ITO and the ion source is switched on. Thus, mass scans at a constant energy and energy scans at a constant mass can be carried out for neutral as well as ionized plasma particle.

As a typical result, the composition of a nitrogen plasma at a stagnation pressure of 1.3 mbar measured with a one-stage configuration is shown in Fig. 16. One-stage configurations of different shapes were also used for the investigation of catalytic effects [24]. They allow an operation at different surface temperatures and with different coatings of the orifice region. Fig. 16 (right) shows the distribution of nitric oxide with different coatings and configurations is shown as an example.

For measurements at higher ambient pressures, a two-staged system MS-II was designed for pressures up to 1 kPa shown in Fig. 17. The inlet system was built with an additional pumping stage between the tungsten orifice and the spectrometer housing. With this two-stage design it was possible to increase the orifice diameter. This configuration was used for catalytic investigations with different orifice materials.

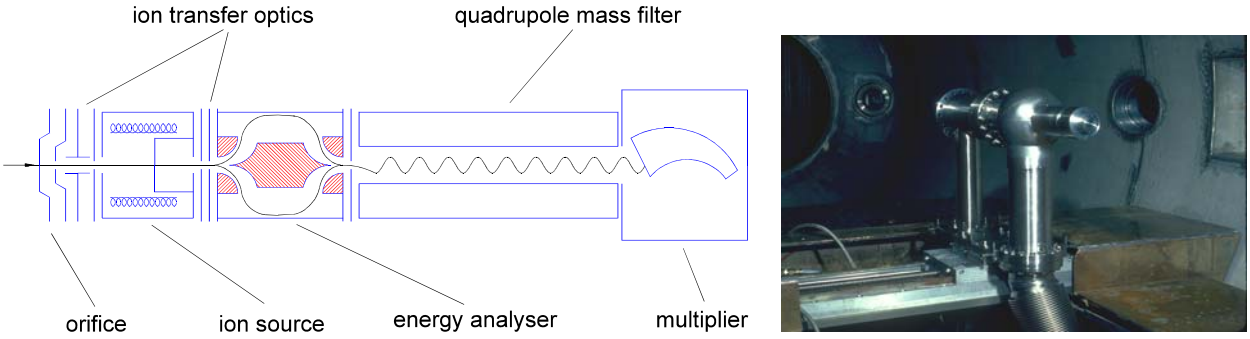

Figure 15: Set-up of the mass spectrometer (left) and mass spectrometer probe inside the plasma wind tunnel (right).

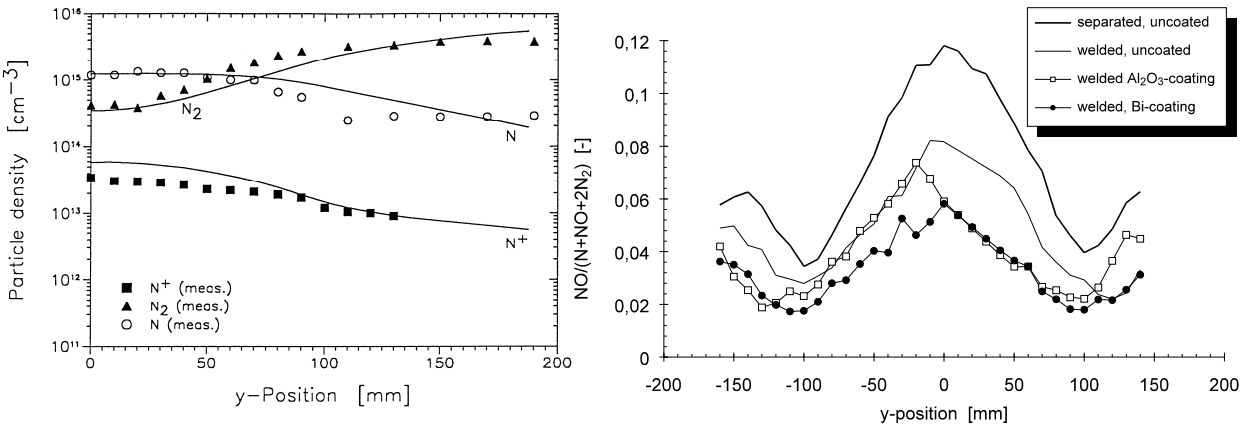

Fig. 16: Comparison of mass spectrometric data and results of the numerical simulation of the 1.3 mbar test case [24] (left) and Distribution of nitric oxide with different cooling heads and coatings in an air plasma (right)

Fig. 18 shows exemplary results for the ratio of NO/N_2 with a tungsten and an SiC orifice, respectively.

Another configuration was finally used to examine the erosion behavior of ceramic heat shield materials. For this purpose, the material sample has to be arranged uncooled just in front of the orifice (Fig. 19) [26, 27]. The erosion products are extracted by the same pinhole diameters as in the one stage configuration. This configuration has been used for the on-line investigation of the erosion behavior of different coatings as well as for the investigation of the passive/active transition of the oxidation of SiC. Fig. 20 e.g. shows the time dependence of the ion percentage of mass 28 which represents Si and CO using a coated C/C-SiC sample (heated up to 1670°C). After 15 s at a temperature of about 1400°C, a rapid increase of the signal can be seen. A surface temperature of 1670°C was reached after 30 seconds when the steep decrease of the signal occurs.This release of Silicon is due to the transition of the sample into the active oxidation mode and was in a later campaign confirmed using an advanced spectroscopic plasma probe.

This example illustrates also one challenge of the mass spectrometer: to distinguish between gas species with equivalent mass. Many other are also present, beside the challenge to operate a highly sophisticated measurement technique directly in a very harsh environment. One of the key challenges is related to catalysis, i.e. occurring chemical (gas phase), catalytic reactions or reaction during the ionization process may "falsify" the measurement leading subsequently to an inverse problem which should be solved in order to obtain the interesting information. Unfortunately, this inverse problem has also several solutions. Nevertheless, mass spectrometry is a very valuable technique for the examination of rarefied flows, at least for qualitative investigations.

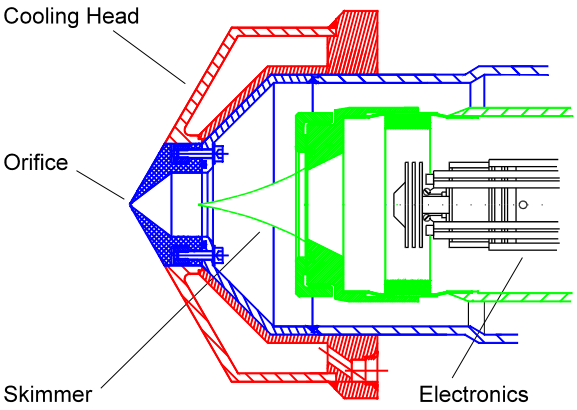

Figure 17: Two-stage inlet system

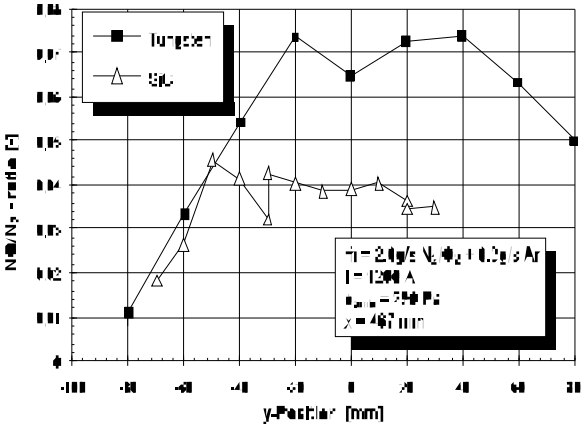

Figure 18: NO/N_2-ratio measured with a tungsten and a SiC-orifice, respectively.

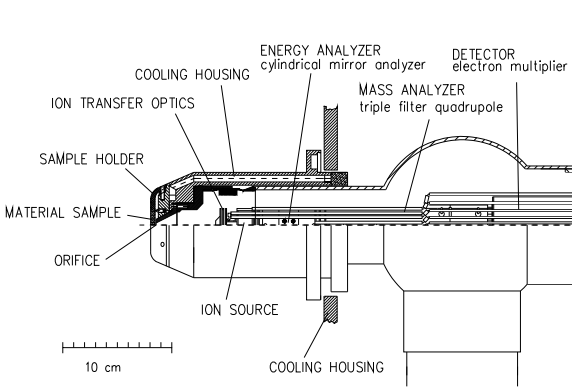

Figure 19: MS configuration for erosion investigation

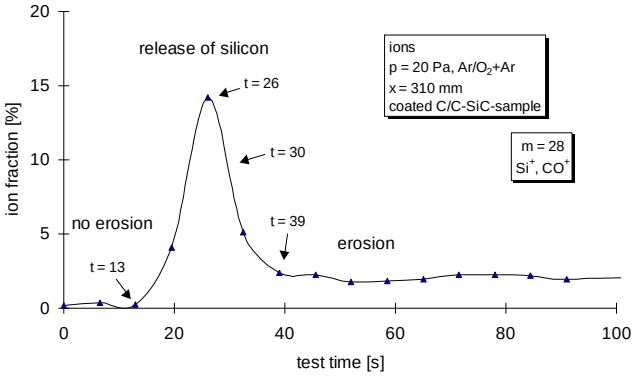

Figure 20: Erosion behaviour.

2.4 Solid State Gas Sensors

2.4.1 Introduction

Almost two decades of research and development activities have been performed at Stuttgart University and TU Dresden on the topic of measuring oxygen partial pressures for various space applications using solid electrolyte gas sensors [28-34]. The sensors have been applied for example to measure the oxygen amount inside the plasma wind tunnels, Figs. 21-23 [28, 29]. In parallel, different flight experiments were performed to measure the residual oxygen partial pressure in higher altitudes onboard of ballistic sounding rockets, which served mainly as precursor experiments for an experiment on-board the International Space Station ("FIPEX on ISS"). The latter should measure the natural and induced environment (atomic / molecular oxygen) [28, 30, 31, 33, 34] and was installed on the outer platform EuTEF (European Technology Exposure Facility) of the European module "Columbus" on the ISS in February 2008 [34]. During 572 days of operation, the instrument FIPEX provided the first time resolved measurement of the residual atomic and molecular oxygen in the higher atmosphere along the ISS orbit.

Basically, "FIPEX on ISS" has been also the stimulus for the new sensor development, because commercially available sensors did not fulfill the requirements for the space application. Very inspiring was also the high interest which simultaneously arose from industry and science for a variety of terrestrial applications, e.g. for environmental and combustion control [32, 38], medicine [39, 41, 42], and vacuum applications [28, 34, 40]. The reasons were mainly the miniaturized design and other features of the new sensor elements, e.g. their capability to detect different gas species like O_2, H_2, CO, CO_2, etc. Modern production techniques and innovative materials were also introduced to allow for high quality, reliable, and miniaturized sensor element design (Fig. 24). Another feature, which resulted from the sensor miniaturization, is the possibility to simultaneously measure other physical properties, e.g. total flow rates and to some extent also total pressures. These characteristics made the new sensor elements even more attractive for a variety of applications on ground and in space.

For example, for many manned space missions, and especially on the ISS, there is a need for a small, light-weight, portable, potentially body-mounted, metabolic gas analyzer with which periodic fitness or scientific evaluations on the astronauts could be performed. Hence, the development of dedicated sensor elements was initiated which are suitable to monitor a time resolved oxygen and carbon dioxide concentration change also under ambient pressures as needed for the human respiratory analysis for medical and fitness purposes. In parallel, the FIPEX sensors have also been adapted to measure oxygen in vacuum and plasma applications, for example in magnetron reactive gas sputter plants for float glass coating [40]. Furthermore, sensors for the measurement of residual oxygen in pure hydrogen or residual

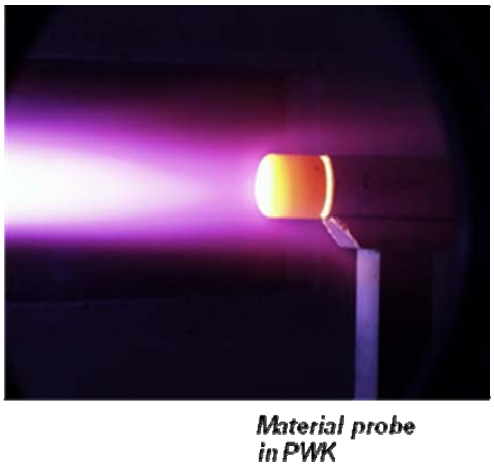

Figure 21: Material probe in the PWK

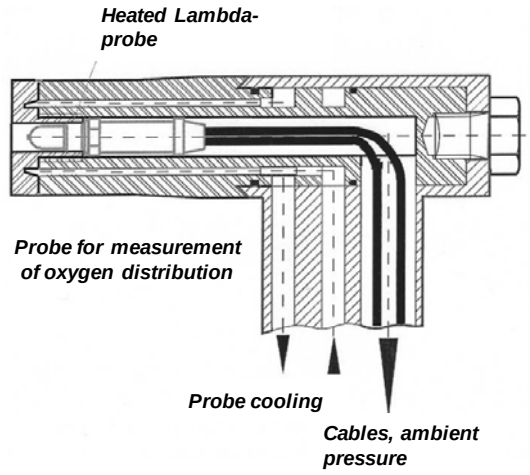

Figure 22: Set-up for the "lambda"-probe inserted as a "gas-specific" Pitot probe.

hydrogen in pure oxygen, as needed for example in fuel cell systems, were investigated. Another example for the challenging terrestrial applications is the use of such sensors for the detection of incomplete combustion (carbon monoxide).

In the following, a brief summary of the measurement principles, the design of the oxygen sensors and some selected remarkable results, especially for rarefied flows, are given. A summary for the other applications is given in [43].

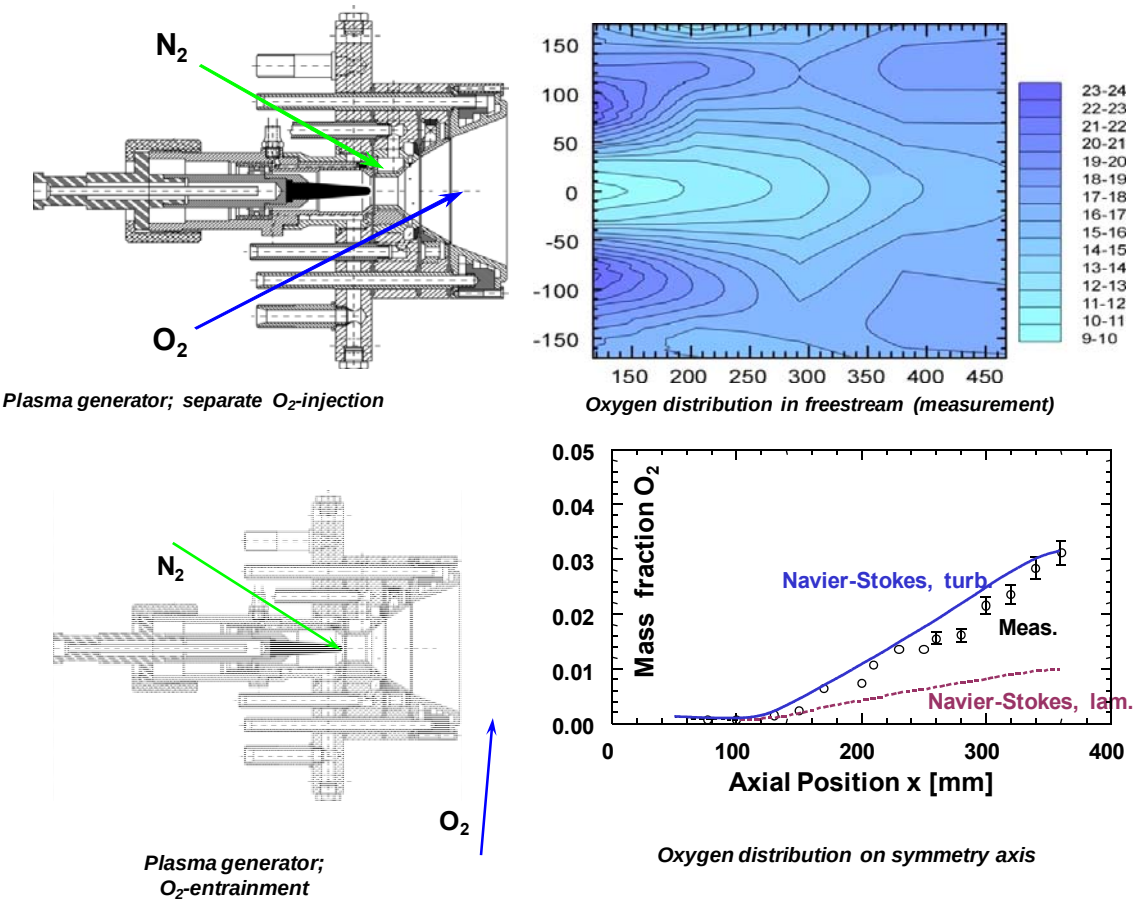

Figure 23: Some results obtained in the plasma wind tunnel applying a "classical" lambda probe (solid electrolyte probe) [28, 29].

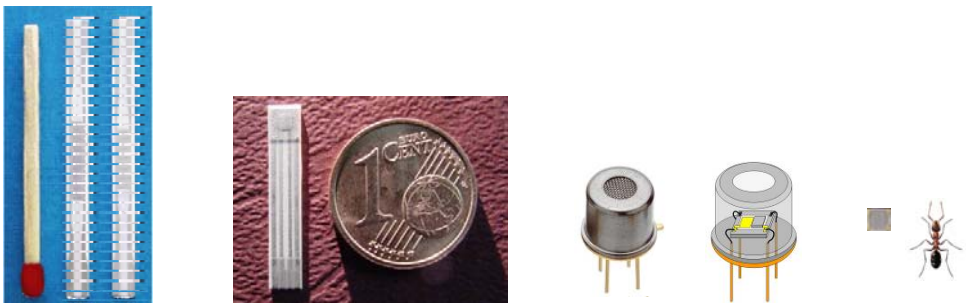

Figure 24: Produced sensor sizes: Typical oxygen sensors for ultra high vacuum applications (left), medical and environ-mental application (mid), ongoing miniaturization (right).

2.4.2 Measurement Principles and Sensor Development

The working principle of the sensors is based on solid state electrolysis using either a potentiometric or an amperometric measurement principle with different electrolytes and electrode materials. Sensitivity and selectivity of the sensors are mainly controlled by geometry, materials, and the manufacturing strategy of the sensitive parts, i.e. screen printing processes that influence the performance of the electrodes and the electrolyte. The sensors are manufactured by screen printing and subsequent sintering of several metallic and ceramic layers on a ceramic substrate. The screen printing technique allows for reproducible, large series of low-cost sensor elements. Fig. 25 shows the design of the multi-layer sensor elements in principle, comprising for example a diffusion layer, sensitive layers, inner and outer electrodes, solid state electrolyte (ionic conductors), an alumina insulator acting as carrier substrate, a heater to control the temperature and a resistance temperature sensor that is separated by an isolation layer.

Of course, the sensor signal depends also on the working temperature in a relatively complex manner, e.g. by the temperature dependencies of the adsorption and desorption processes on the electrodes, the ionic conductivity of the electrolyte, and by several other occurring physical phenomena that are relevant for the sensor signal. Thus, the heater design itself is optimized to obtain a uniform temperature distribution and to induce only a minimum thermal stress on the sensor element.

The development of the sensors is an iterative and hardly predictable process because minimal changes in each layer composition and/or sintering procedure may lead to very different results. Therefore, hundreds of sensor configurations have been designed, manufactured, and analyzed. This optimization process resulted in a remarkable improvement of the sensitivity and stability of the measurement, leading to almost ideal characteristics. Different tests demonstrated the good sensitivity e.g. to oxygen and the exceptionally fast response to oxygen changes.

For the oxygen sensors, yttria-doped zirconia (YSZ) is used as electrolyte, the electrochemical properties of which have been studied already since the last century when Nernst investigated its ionic conductivity [36]. YSZ selectively conducts oxygen ions at higher temperatures (above about 450°C) and the sensor has therefore to be heated up to a constant working temperature. An ideal electrochemical cell, as sketched in Fig. 26, leads then to an Electro Motive Force generated across the solid electrolyte caused by oxygen concentration differences. This leads to a potential difference to be measured as sensor voltage U_S between the electrodes in the so called *potentiometric measurement principle*:

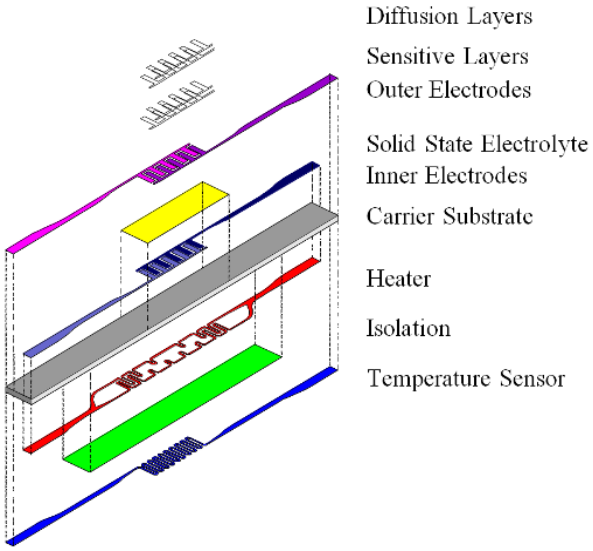

Figure 25: Principle design of multi-layer sensor elements manufactured by screen printing and subsequent sintering.

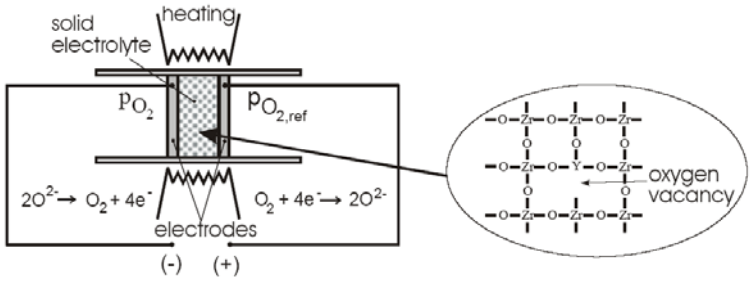

Figure 26: Ideal potentiometric electrochemical Nernst cell and oxygen vacancy of the YSZ structure.

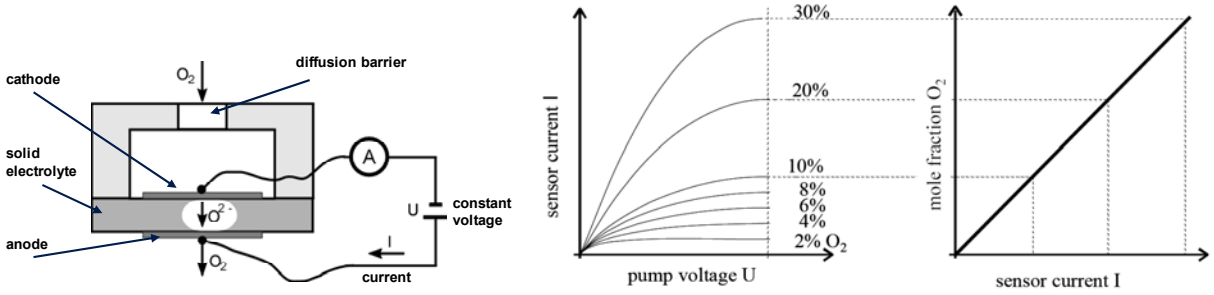

Figure 27: Sketch of the amperometric measurement principle with sensor current limiting diffusion barrier.

$$\Delta U_S = U_0(\Delta T) + \frac{\Re T_s}{nF} \ln \frac{p_{o_{2,ref}}}{p_{o_{2,meas}}} \quad . \tag{27}$$

Ö ª ˇß˘ ℜ is the universal gas constant, T the electrode temperature, F the Faraday constant, n the valence of the ions involved in generating the potential, $p_{O2,ref}$ the O_2 partial pressure in a reference chamber and $p_{O2,meas}$ the O_2 pressure in the measurement chamber. The offset voltage U_0 originates from a temperature difference ΔT between the two electrodes, e.g. due to forced convection, insufficient heating, asymmetric sensor geometry and/or catalytic combustion at one electrode. The need of a hermetically sealed reference chamber with constant $p_{O2,ref}$ makes clear that the potentiometric measurement principle, as used for example for different commercially available λ-probes, is not very well suited for the use in the harsh environment in space. Hence, the *amperometric principle* with reference electrodes has been chosen for the further oxygen sensor development. The amperometric principle makes also a flat sensor design and the fabrication by thick film technologies possible. As a side effect, a miniaturization in scale, mass, and power demand is achievable.

In the *amperometric principle* and flat design, the oxygen concentration is then determined by measuring the current that is conducted through the electrolyte at a constant applied voltage (Fig. 27). Here, the measured current I_{sen} is directly related to the number of oxygen ions conducted through the electrolyte. Consequently, if a diffusion barrier limits the oxygen flux from the ambient air to the cathode, the resulting electrical current depends linearly on the ambient oxygen concentration $c_{environment}$ (every oxygen at the cathode is transported through the electrolyte; the oxygen concentration at the cathode $c_{O2,\ cathode}$ becomes zero, $\Delta c = c_{environment} - c_{O2,\ cathode}$), i.e.

$$I_{sen} = nFD \frac{c_{environment}}{L} Q_{diff} \quad , \tag{28}$$

where D is the diffusion constant, L a diffusion length, and Q_{diff} a diffusion area. Now, in order to achieve very short response times, the length of the diffusion barrier should be as small as possible. Thus, in the applied planar design, the screen-printed electrolyte itself is one part of the diffusion barrier and some

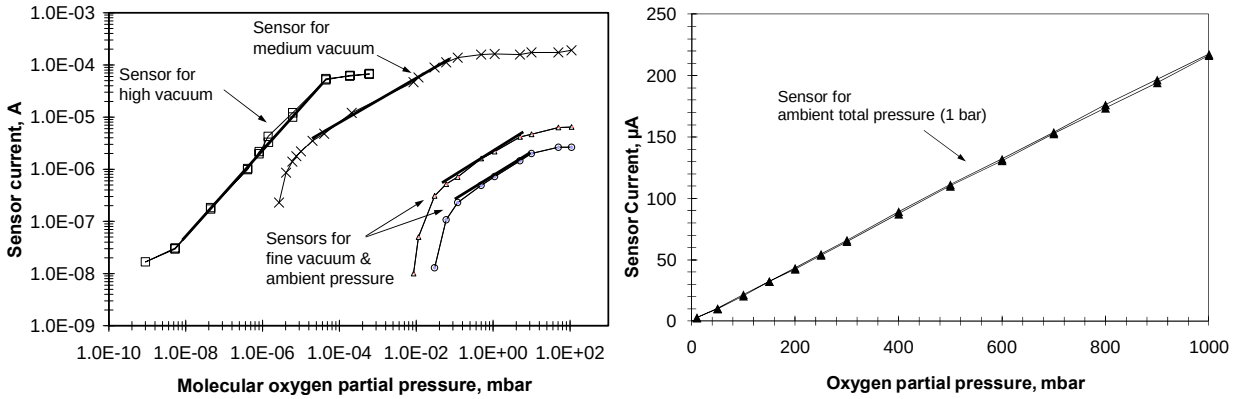

Figure 28: Oxygen partial pressure range for sensors with different diffusion layers and active electrodes areas for different high vacuum, medium vacuum (left) and ambient pressure conditions (right).

additional layers above the electrolyte assist in adjusting the required porosity. Diffusion layers with a low diffusion constant are then needed under low pressure conditions because the O_2 molecule flux is naturally limited by effusion. The resulting sensor current is very low (nano- to some microampere) caused by the naturally very low oxygen concentration. Also, in order to control occurring overpotentials at the cathode, an additional reference electrode is used and the resulting three electrode configuration leads to the required low response times and sensor signal stability, especially at very low O_2 partial pressures.

The oxygen sensor measurement range and the maximum detectable oxygen partial pressure can be adapted by adjusting the overall porosity of the diffusion layers, the active electrode areas, and the number of adsorption places for the oxygen molecules at the electrodes that allow for an electron transfer reaction. Fig. 28 illustrates the ranges for different sensor designs - the left part depicting the remarkable wide range of detectable oxygen partial pressure, the right part showing the characteristics of a full range oxygen partial pressure sensor as developed for medical and environmental applications under ambient pressure conditions (1 bar).

2.4.3 Space Experiment FIPEX on ISS

Space vehicles in low altitudes, orbit the Earth with a velocity of about 8 km/s in a highly rarefied atmosphere. Above the mesopause (from about 85 km) the molecular oxygen is dissociated because of the solar radiation in the UV-regime. Subsequently, atomic oxygen dominates above this altitude up to about 1000 km compared to oxygen and nitrogen molecules. Because drag of space vehicles in low Earth orbit is mainly influenced by the density of the flow, it is important to know the conditions on hand relatively exact. However, because the atmosphere's composition is influenced by the solar radiation and the Earth's magnetic and gravitational field, the exact constitution at a given point depends upon many different parameters, which include long-term, short-term and spatial variations. Many different semi-empirical models were developed in the past with which it is possible to calculate the data for any spatial position at a given time. However, the results of these models may differ by more than one order of magnitude. Thus, the prediction of total density and gas partial pressures for satellites and the International Space Station flying at these altitudes is insufficient.

Especially the flux of atomic oxygen is of general importance as it shows different interactions with spacecraft surfaces, e.g. erosion of the surface material. With the FIPEX micro-sensor experiment the atomic oxygen in the surrounding of the International Space Station was measured. FIPEX sensors are able to distinguish and measure molecular and atomic oxygen at very low ambient pressures (Fig. 28 (left) shows sensor characteristics for molecular and Fig. 29 for atomic oxygen). The behaviour of the sensor is manipulated by using different electrode materials, i.e. if the cathode is made of a material with negligible dissociative absorption of molecular oxygen, only atomic oxygen can be detected. The main objectives of

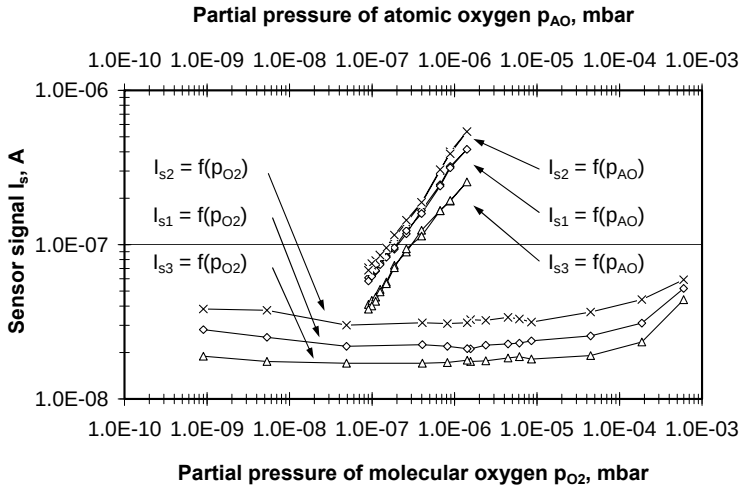

Figure 29: Atomic oxygen sensor signal depending on atomic and molecular oxygen partial pressures.

FIPEX have been in summary:

- Time resolved measurement of atomic oxygen flux in low Earth orbit over a long period of time.
- Verification of atmosphere models.
- Investigation of the Space Station contamination in thrusting periods and during proximity operations of the logistic vehicles. This experiment can give a time resolved determination of the contamination of satellite structures in space.
- Investigation of the behaviour of the ceramic solid electrolyte and the different electrode coatings during exposure to the space environment.

The FIPEX flight experiment consists of three separate parts, two Sensor-units and one Electronics-box. The two Sensor-units contain 6 sensors each and are mounted onto the Electronics-box, one into RAM (flight) direction measuring the dynamic pressure and one into ZENITH direction measuring the static pressure of the atomic and molecular oxygen. The main electronic box houses the sensor control, the experiment command and data handling, the power control and the thermal control system. The complete space qualification of the experiment according to ECSS-standards had been conducted at the TU Dresden with high involvement of students. FIPEX was launched on STS-122 (1E) Shuttle flight on 7 February 2008 and was mounted on the COLUMBUS external payload facility EuTEF having a free field of view into flight and zenith direction of the International Space Station (Fig. 30). During the 572 days FIPEX

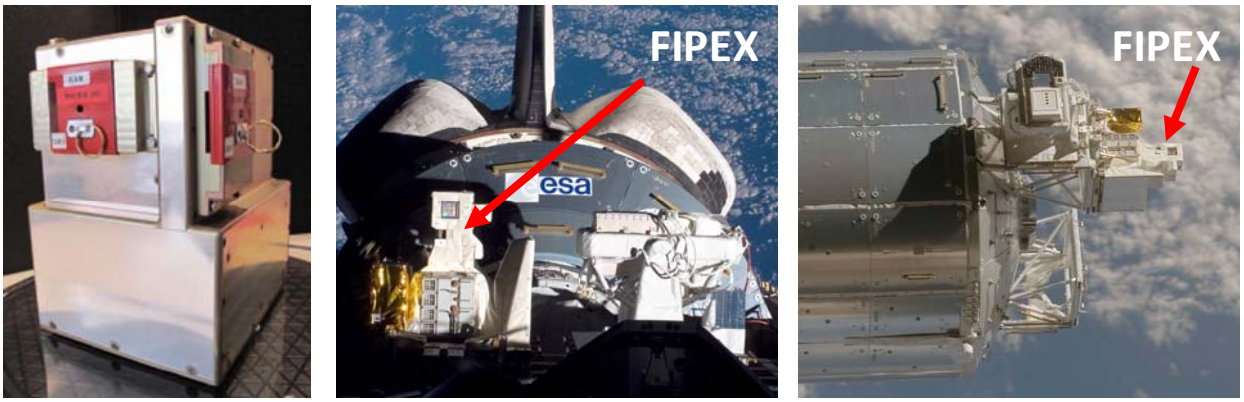

Figure 30: FIPEX flight model (sensor unit are saved by remove-before-flight caps) (left), FIPEX integrated on Shuttle STS-121 (1E), FIPEX mounted on COLUMBUS module

operation in orbit, the experiment was directly commanded and scientific data was obtained by the FIPEX User Home Base at the TU Dresden, Germany.

First results of the sensor currents versus the prediction of atomic oxygen using the atmosphere models are illustrated in Fig. 31. These first results show deviations of the transient behavior of AO compared to the prediction of the higher atmosphere models NRLMSISE, MET and DTM (NRLMSISE is an empirical model of the temperatures and the densities of the atmosphere's components: US Naval Research Laboratory Mass Spectrometer and Incoherent Scatter Radar Exosphere, MET: Marshall Engineering Thermosphere Model, DTM: Density Temperature Drag Model). The results show an increase of AO after local sunrise when ISS orbits from south to the equator followed by a decrease when continuing the orbit to higher latitudes. Some minutes before the ISS exits the local eclipse phase, the AO level reaches its minimum.

FIPEX on ISS provided the first long time and time resolved measurements of atomic oxygen along the ISS orbit. Exact results will be published after processing of all data and the sensor post calibration. The time resolved data can be used to correlate the models of the higher atmosphere and to improve the prediction of the atomic oxygen flux during a space mission, hence the erosion of the surface materials.

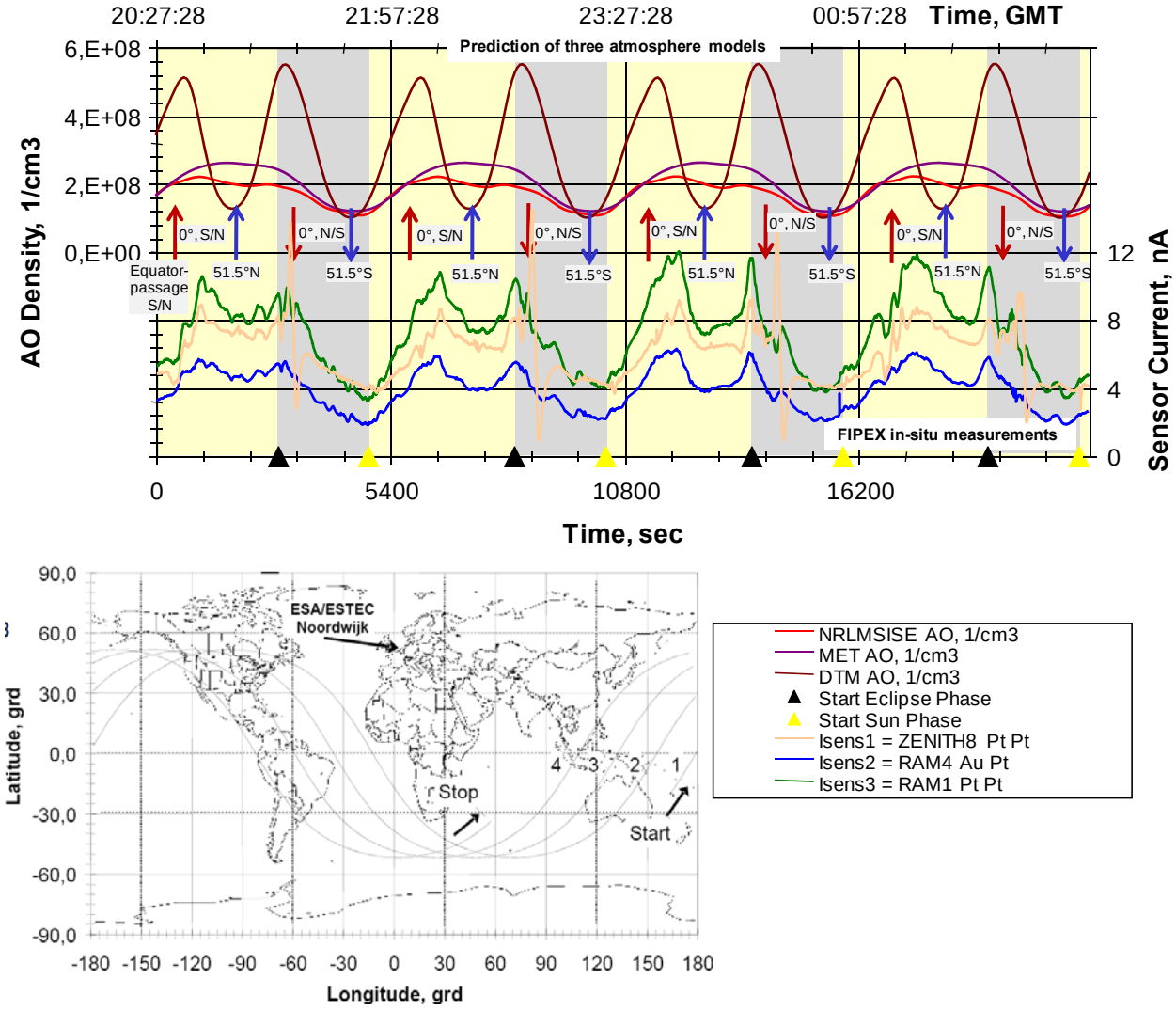

Figure 31: ISS ground track during the first four FIPEX orbits and FIPEX sensor signals (3 sensors) versus predictions of atomic oxygen using the atmosphere models from 16-17. April 2008.

2.4.4 Terrestrial Vacuum Applications

Glass is the major cause of heating and cooling losses of buildings. 30% of all heat losses are due to old glass. Coated heat protection glass reduces heat losses by about 60% compared to uncoated isolation glass. The energy saving potential is 20 liters of heating oil corresponding to 50 kg carbon dioxide per year per square meter glass. A uniform color and reliable heat protection requires homogeneous coating and high production line reproducibility. Based on FIPEX, the VacuSen sensor was further developed for vacuum and plasma technology application. Its purpose is to provide an easy, low cost, time resolved in-situ process control e.g. directly in a magnetron reactive gas sputter plant for float glass coating. The goals are to measure the total or oxygen partial pressures, to optimize the coating process and to enhance the quality of the coating using the robust solid electrolyte gas sensor technology.

The design of the VacuSen sensor is straight forward for simplicity in function, small size and projected low cost. The geometry is 20x3.5x0.5mm, resulting in a reduced heater power of around 2W at 660°C. Commercially available oxygen partial pressure measurement devices are flange mounted, because they need direct contact to the outer "reference" atmosphere. Due to the space driven miniaturization and the reference-free measurement principle, VacuSen can also be mounted freely inside a vacuum chamber, exactly where the process takes place and the relevant parameters have to be monitored. This is advantageous, especially for application in a reactive gas magnetron sputter plant where the typical dimensions of float glass are up to 6x3.5m. During the coating process, the glass passes through different sputter chambers, each of them separately controlled with Argon and Oxygen as reactive gas. In order to guarantee equal reaction process conditions in each chamber along the length and width of the float glass and hence, a uniform coating quality, several VacuSen sensors can be positioned directly inside the chambers for continuous in-situ process control and optimization. The nominal operation point for the coating plant is at a total pressure of around $1 \cdot 10^{-3}$ mbar.

The characteristics of 20 VacuSen-systems around this working point are shown in Fig. 32. The measurement range is at total pressures of $1 \cdot 10^{-5}$ - $1 \cdot 10^{-2}$ mbar, corresponding to oxygen partial pressure of about $2 \cdot 10^{-6}$ - $2 \cdot 10^{-3}$ mbar. A linear characteristics in double logarithmic scale follows $I_{sens}=b \cdot p_{tot}{}^{m}$ (I_{sens} in µA, p_{tot} in mbar) with a constant slope of around m=0.8±0.05 and a sensor specific y-axis intercept b. b can be obtained by an easy one-point calibration routine around the nominal operation point.

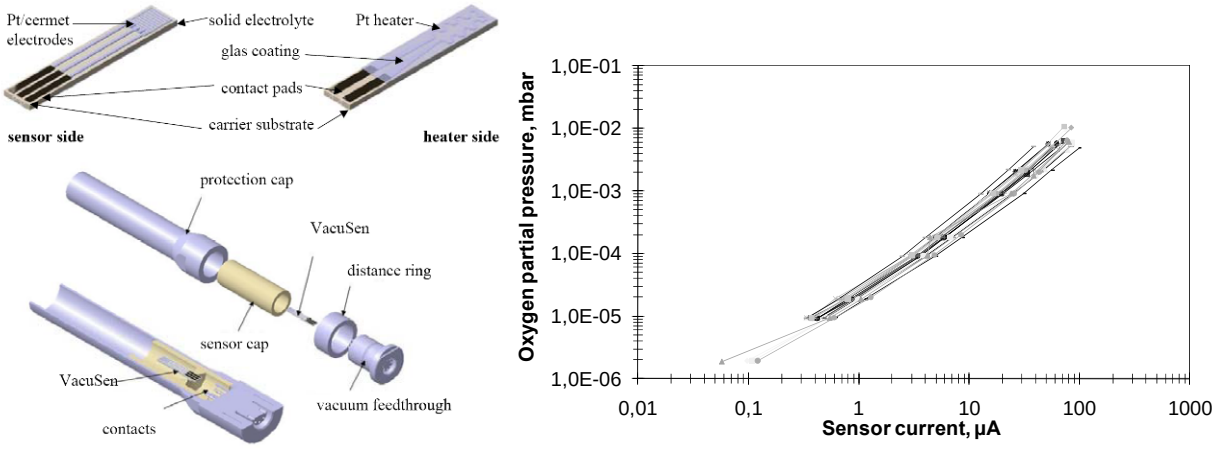

Figure 32: VacuSen characteristics of 20 sensors between $p_{tot}=1 \cdot 10^{-5}$ to $1 \cdot 10^{-2}$ mbar, corresponding to $p_{O2}=2.1 \cdot 10^{-6}$ to $2.1 \cdot 10^{-3}$ mbar.

2.5 Electrostatic Probes

Electrostatic probes normally used in plasma wind tunnels and for the investigation of electrical thrusters consist of up to three electrodes which are electrically insulated from each other and from mass and are exposed to the plasma. By recording current-voltage characteristics or current-time developments, the various parameters of the plasma such as plasma potential, electron temperature and density, flow direction, electron energy function, plasma velocity or ion temperature can be determined at the position of the probe electrodes [4, 44].

If one moves an electrostatic probe into a plasma beam, a plasma boundary layer forms around the probe. This layer can be altered by varying the bias voltage across the probe. Important plasma parameters can be deduced from the probe signal. For this purpose, the boundary layer must be described theoretically.

When moving a probe into a plasma assumed to be quasi-neutral, a negative charge of the probe takes place across from the surrounding plasma. This is because the higher thermal moveability of the electrons causes more electrons than ions to reach the probe electrode surface. The negative charge causes a repulsion of further electrons in the area around the probe. Therefore, a positive space charge layer forms which disturbs the ionization-recombination equilibrium. The higher ion density in the space charge layer around the probe, compared to the electron density, causes the formation of an electric field which decreases as the distance to the probe surface increases.

As a result of the recombinations on the probe surface, charge carriers from the quasi-neutral, undisturbed plasma have to subsequently be delivered to the space charge layer. This charge carrier drift requires the existence of a weak remaining field which must also be present outside of the space charge layer in the so-called transition region. Fig. 32 shows the development of the potential in the entire plasma surface layer.

The thickness of the space charge layer is given by the Debye length λ_D which is dependent on the electron temperature and density by means of the equation

$$\lambda_D = \sqrt{\frac{\varepsilon_0 k T_e}{e^2 n_e}} \quad . \tag{29}$$

Fig. 33 shows that, for example, in MPD tunnels the Debye length is several mm. In the adjacent transition region, a slight charge carrier concentration decline still exists which affects the drift. Despite the small, remaining electric field in the transition region, the plasma can be considered as quasi-neutral for the theoretical treatment. For additional increasing distances from the probe surface, the undisturbed, quasi-neutral plasma with the potential V_{PL} is finally reached. The border of the space charge layer is determined by the so-called Bohm criteria according to which the charge carriers entering the space charge layer have

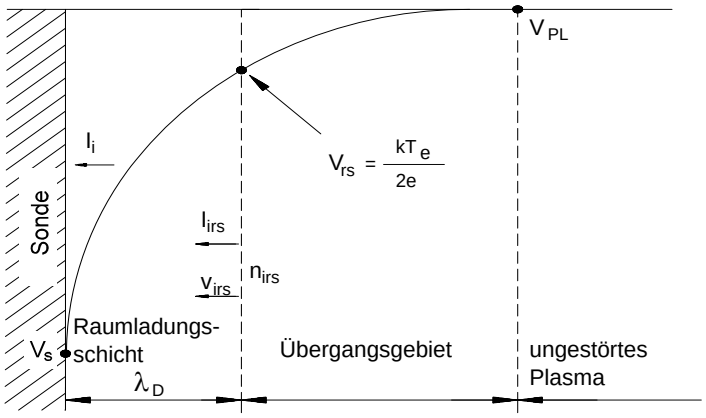

Figure 33: Potential development in the plasma surface layer.

to apply the energy of

$$eV_{rs} = \frac{kT_e}{2} \tag{30}$$

Moreover, for the theoretical description of the boundary layer, the smallest mean free path is of importance. It is the mean free path due to electron and ion collisions:

$$\lambda_{ei} = \frac{16\pi(\varepsilon_0 kT_e)^2}{e^4 n_e In\Lambda} \tag{31}$$

with

$$\Lambda = 12\pi \frac{(\varepsilon_0 kT_e)^{3/2}}{n_e^{1/2} e^3} \quad . \tag{32}$$

As can be seen in Fig. 34, in the MPD tunnels it is expressed in mm.

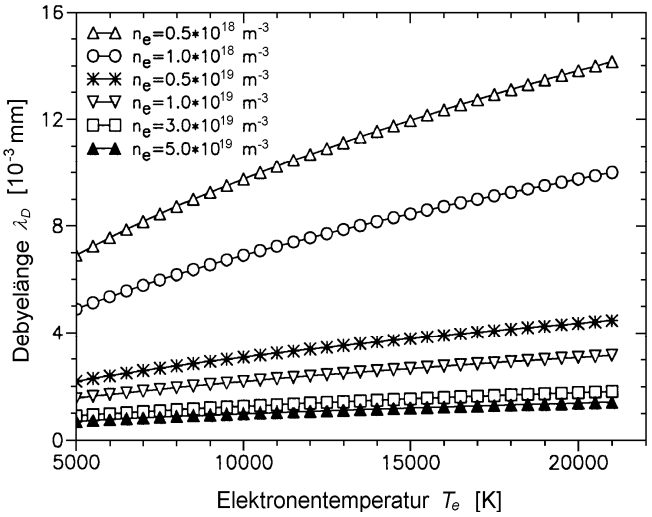

Figure 34: Debye length as a function of n_e and T_e.

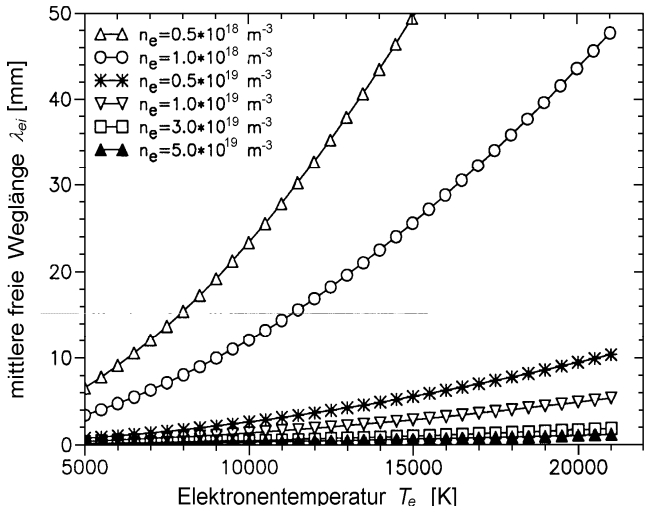

Figure 35: Mean free path as a function of n_e and T_e.

The current flowing to a probe's surface depends on the mean free path λ_{ei} of the charge carrier and the Debye length λ_D in the space charge layer and on the probe radius r. The relationships between these parameters determine whether the movement of the charge carriers in the space charge layer is influenced by a shock. If the probe radius can be chosen so that

$$\lambda_{ei} >> r >> \lambda_D \tag{33}$$

is fulfilled, then a so-called conventional shockless thin space charge layer can be assumed.

In an MPD tunnel partial densities of the charged particles in the investigated regions of the air plasma flow, ranging from x=50 mm to 500 mm axial distance to the MPG, are in the range of $n_e=10^{17}$ to 10^{21} m^{-3}. With electron temperatures T_e of 5000 to 30000 K, this results in Debye lengths of λ_D < 40 µm. The Coulomb mean free paths are in the range of $\lambda_{ei} \geq$ 1 mm.

The shockless theories developed for stationary plasmas and cylindrical probes can also be applied to flowing, shockless plasmas when the cylindrical probes with a length l are aligned with the plasma flow and $l/\lambda_D >> 1$ is fulfilled. In the case of larger Debye lengths the plasma layer is enlarged at the front surface of the probe. And the ion current to this surface compared with the ion current to the cylindrical surface of the length l can no longer be neglected. The ratio l/λ_D is proportional to the so-called end effect parameter τ_l which is a criterion for the portion of current to the front surface of a cylindrical probe aligned with the plasma flow. For $\tau_l > 50$ this amount of current is negligible.

Table 1 gives an overview of the kinds of probes that are typically used for plasma diagnostics and the plasma parameters which can be determined with each one.

Probe	**Parameters**
Single probe	Electron temperature T_e, electron density n_e, plasma potential, electron energy distribution
Double probe	Electron temperature T_e, electron density n_e
Triple probe	Electron temperature T_e, electron density n_e
Time of flight probe	Plasma velocity
Electrostatic angle probe	Plasma flow line
Rotation electrostatic probe	Plasma flow line
Electrostatic crossed probe	Plasma velocity at known ion temperature Ion temperature at known plasma velocity

Table 1: Mean free path as a function of n_e and T_e.

2.6 In-Situ Radiometer

Radiometer probes are mainly used to determine the radiation heat flux. By using appropriate filters, however, conclusions about the gas composition can also be made. The radiation intensity of the plasma rises with the fourth power of the gas temperature when only the continuum part of the plasma radiation is taken into account. The following relation is approximately valid for the radiation heat flux, whereby the degree of emission of the plasma can be smaller than that of the thermal protection material depending on the plasma condition:

$$\dot{q}_{radiation} \sim \varepsilon_{plasma} T_{plasma}^4 - \varepsilon_{wall} T_{wall}^4 \tag{34}$$

At plasma temperatures of 10000 K and higher and at pressures of up to 100 mbar, the radiation heat flux can generally no longer be neglected and reaches the same order of magnitude as the convective part. Fig. 35 (left) shows, for example, calculated heat fluxes for the entry of the Huygens probe into the atmosphere of the Saturn moon Titan.

In ground test facilities a detector can be placed perpendicular to the plasma beam or to the shock front to measure the radiation heat fluxes. The measurement devices are then located outside of the evacuated test chamber and the optics are focused on the test point through windows or light wave conductors. This stipulates long distances to the measurement position along which radiation can be absorbed and the measurable wave length region remains limited to the transmission area of the windows or the light wave conductors.

The more direct way is to place the radiometer in a probe which is directly exposed to the plasma. For this purpose a radiometer probe, shown in Fig. 35 (right), was developed at the IRS. Various glass shields, filters and detectors can still be used as indicated. However, they limit the usable spectral region. The goal, however, of radiometric measurements is to cover the entire radiation which appears. But the detectors may not touch the plasma because they can be damaged by the heat. This can be avoided by mounting the detector deep inside the cooled probe body. The radiation reaches the detector through an optical tunnel. Here a cold, stationary gas column forms because the detector completely closes off the end of the tunnel. However, this method clearly narrows the visible solid angle. In order to get the entire radiation on the front side of the sample, the probe has to be rotated in the beam while being measured so that the complete solid angle is covered. A hemispherical numerical integration results then in the demanded radiation heat flux at the front opening of the radiometer [45].

The detector and where applicable the filters and lenses must be suited to the task. Special attention must be paid to the choice of the detector. After that the most important characteristics are compiled.

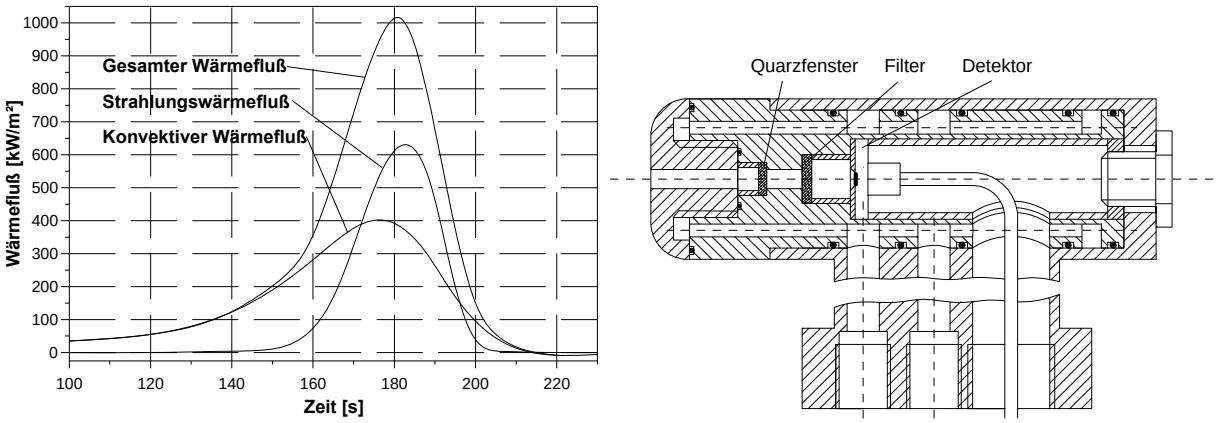

**Figure 36: Left: Calculated heat fluxes for the entry of the Huygens probe into the N_2/Ar/CH_4 atmosphere of the Saturn moon Titan (without catalytic effects) .
Right: Radiometer probe with dismountable quartz window and filter**

The signal-noise ratio and the noise equivalent power (NEP) are used to assess and compare detectors. The signal-noise ratio is the ratio between the output signal of a detector and the superordinated noise. It describes the maximum possible exactness of a measurement. With a signal-noise ratio of 100:1, the exactness of the measurement can in no case be better than 1 %.

In a radiometric detector the NEP indicates the radiation power which has to reach the detector in order to create a signal-noise ratio of 1. NEP is also the smallest measurable power which reaches the detector. The following applies:

$$NEP = \frac{I_n}{S} \tag{35}$$

Here I_n is the noise voltage or the noise current of the detector and S is the total sensitivity. Because S depends on the relative spectral intensity distribution of the radiation source, when comparing various NEP values it must be taken into account that they were recorded with the same radiation source under the same conditions. Usually a black radiator with a temperature of 500 K is used.

Additional important characteristics are:

- **Linearity:** The linearity is one of the most important specifications of a detector for radiometric measurements. Linearity exists when in a certain range the output signal of a detector is exactly proportional to the incoming radiation or when the sensitivity of the detector does not depend on the incoming power.
- **Time constant** The time constant τ of a detector reports the time that the detector signal requires to reach 63% of the final value after constant radiated power suddenly appears on the detector.
- **Total sensitivity of a detector** The total sensitivity of a detector is the ratio between the detector output signal *I* and the total incoming radiated power Φ in a certain wavelength region. It is a function of the detector, the radiation source and the transmission from windows and filters on the optical axis of the measurement arrangement. A certain detector has a different total sensitivity for each radiation source.

$$S = \frac{I}{\Phi} = \frac{\int_{\lambda_1}^{\lambda_2} \Phi_{e/\lambda}(\lambda) S_\lambda(\lambda) \tau(\lambda) d\lambda}{\int_{\lambda_1}^{\lambda_2} \Phi_{e/\lambda}(\lambda) d\lambda} \tag{36}$$

with: λ_1, λ_2 = lower or upper boundary wavelength
S = total sensitivity
I = detector output signal
Φ = total incoming radiation
$\Phi_{e/\lambda}(\lambda)$ = absolute spectral intensity distribution of the radiation source
$S_\lambda(\lambda)$ = spectral sensitivity, known from the calibration
$\tau(\lambda)$ = transmission from windows and filters

Instead of the absolute spectral intensity distribution $\Phi_{e/\lambda}(\lambda)$ the relative or normalized spectral intensity distribution can be used:

$$\phi(\lambda) = \frac{\Phi_{e/\lambda}(\lambda)}{\Phi_{e/\lambda}(\lambda_0)} \tag{37}$$

λ_0 is here the normalized wavelength. The radiation heat flux onto a detector surface A can be calculated as:

$$\dot{q}_{Strahlung} = \frac{I}{AS} \tag{38}$$

If in addition the measurement arrangement is divided by the visible solid angle, one obtains the radiation heat flux in [W/(m^{2}sr)].

Fig. 36 shows several profiles of the radiation heat flux perpendicular to the beam axis at various N_2/CH_4 plasma combinations used to simulate the entry of the Huygens probe into Titan's atmosphere. The measurement shows the significance of plasma radiation in the VUV which, by an assessment of other scientific works referenced in [45], could be assigned to nitrogen molecular transitions and atomic lines. Post flight analyses performed at IRS e.g. for FIREII could approve the significance of this spectral radiation for hyperbolic re-entries as this radiation contributes a significant fraction of the integral radiative heat flux (up to 90 %). The respective results are currently under further investigation and will be published in a future work.

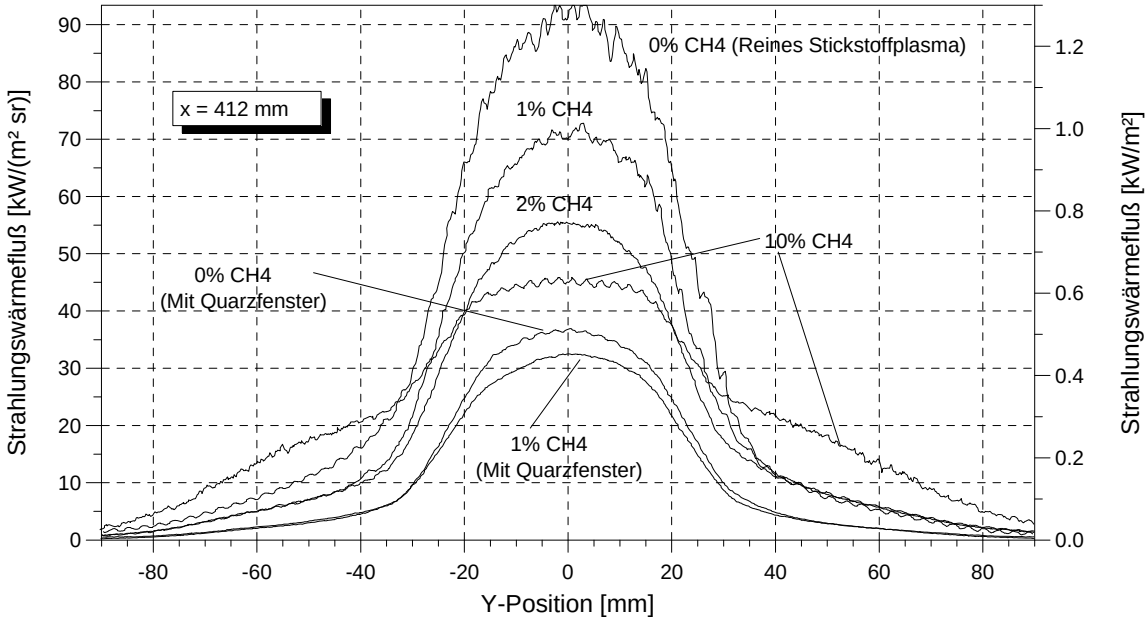

Figure 37: Radial profiles of various N_2/CH_4-plasmas with and without a protective window at a distance of 412 mm to the plasma generator

3.0 NON-INTRUSIVE MEASUREMENT TECHNIQUES

3.1 Introduction

3.1.1 General Remarks

Non-intrusive measurement techniques intend to determine flow properties from the analysis of light that is either emitted or absorbed. The physical principle to be used is based on the fact that every species can absorb or emit light at characteristic wavelengths depending on the electron configuration and the thermodynamic state of the species, because every species has characteristic discrete, quantized energy levels. Optical non-intrusive techniques have been used for many years and are state of the art particularly in combustion process diagnostics [48].

From a historical point of view, there have been three major problems at the beginning of the last century (around 1900). After the invention of the electron (found by Thomson in 1897), there were basically three physical observations not understood: the continuum radiation curve (the so-called ultraviolet catastrophy), the mystery of the photo effect (the photo current depends on wavelength and not on light intensity), and the discrete absorption and emission lines of flames and sunlight (Bunsen and Kirchhoff observed a flame with a spectrometer). It was only after the idea of Planck that energy is transferred in discrete quantums which allowed explaining all three observed phenomena [47].

Nowadays, quantum mechanics is a wide field in theoretical and experimental physics and engineers use these basic principles in order to understand rarefied gas flows *non-intrusively*, i.e. without disturbing the macroscopic characteristics of the flow.

Although not particularly useful for rarefied gas flows, pyrometry is somewhat the very first measurement technique. It means the integral measurement of electromagnetic light intensity emitted by a gas flow or a hot surface. It is based on the pure continuum radiation detection. If the radiation is recorded as a function of the wavelength, the diagnostic is named optical emission spectroscopy. Atoms and molecules have discrete, quantized energy levels. For atoms, these energy levels are only electronic (based on the electron configuration around its nucleus), while molecules have additionally rotational and vibrational energy levels. If certain selection criteria are met - which is a result of quantum mechanical considerations – atoms and molecules can undergo a transition ongoing with the emission of light at a certain wavelength. The observed transition line has a characteristic line form depending on the thermodynamic state of the gas species. From an analysis of the rotational, vibrational and electronic emission lines of a species, the thermodynamic state of the gas can be identified and qualitative information about the composition of the gas can be drawn. If an emission line can be resolved with a high resolution using interferometry, temperatures and even flow velocity can be measured. At IRS, Fabry-Perot interferometry is applied.

Again a more complex optical diagnostic technique became useful with the invention of lasers. Laser light, which is tuned to wavelengths such that the species of interest interacts with it, results either in scattering or absorption of the laser light energy. Since this lecture focuses on rarefied gas flows, only measurement techniques that are applicable to this low pressure regime are discussed. The effective cross sections of scattering processes are relatively small and therefore not applicable to low pressure flows.

Since all of the non-intrusive optical diagnostic techniques are derived from the same physical principles, the mathematical background is summarized first. Then, every measurement technique is discussed separately.

3.1.2 Plasma state

For plasma flow diagnostic, the plasma state and its definition are of basic importance. The state of *complete thermodynamic equilibrium* means each elementary process (e.g. ionization) is in equilibrium with its complementary (in this case recombination). The numbers of both processes per unit time are

equal. The most important properties of plasma in complete thermodynamic equilibrium are:

- The spectral distribution of the emitted radiation is that of a black body radiator and follows Planck's Law.
- The velocities of all particles follow *Maxwell's distribution function* with a common temperature T

$$f(v) = \frac{1}{N}\frac{dN}{dv} = \frac{4}{\sqrt{\pi}} v^2 \left(\frac{m}{2kT}\right)^{\frac{3}{2}} \exp\left(-\frac{mv^2}{2kT}\right) \tag{39}$$

  v is the velocity value, m the particle mass and N the number of particles per volume unit.
- The ratio of the number of particles in an excited state $n_{i,n}$ and the number of all particles of the regarded species n_i is given by a *Boltzmann-distribution*. For this case, the Boltzmann equation

$$\frac{n_{i,n}}{n_i} = \frac{g_{i,n}}{g_{i,0}} \exp\left(-\frac{E_{i,n}}{kT}\right) \tag{40}$$

  is valid. The quantities $g_{i,n}$ and $g_{i,0}$ are the statistic weights of the different excitation levels of the regarded ionization stage. They are always integers and can be derived from quantum mechanical laws or taken from spectroscopic tables. $E_{i,n}$ is the energy of the excited state n.
- The chemical equilibrium which is also a part of the complete thermodynamic equilibrium is defined by the *law of mass action*. A reaction A + B $\Rightarrow$ C is described by:

$$\frac{n_A n_B}{n_C} = K(T) \tag{41}$$

  Here, n_A, n_B and n_C are the concentrations of the reacting components and K is the velocity constant of the particular reaction. K is a function of the temperature and has to be determined experimentally.
- The last important requirement is a relation for the ionization-recombination equilibrium which is given by the *Saha-Eggert equation* which is in fact the law of mass action for the ionization reaction. Limiting the possible ionization stages to 1 yields for the degree of ionization α for an atomic gas:

$$\frac{\alpha^2}{1-\alpha^2} = \frac{(2\pi m)^{\frac{3}{2}}}{ph^3} (kT)^{\frac{5}{2}} e^{-\frac{E_i}{kT}} \tag{42}$$

  Here, E_i means the energy of ionization and p is the pressure of the plasma.

In a real plasma there are always differences from complete thermodynamic equilibrium. If those differences are moderate and limited to single processes, the plasma state can often be described as close to equilibrium. There are several possibilities to access the parameters of those plasma states but the most important one is probably the LTG-model (*local thermal equilibrium*). In this case, all properties of the complete thermodynamic equilibrium, with the exception of the requirement of a Planck distribution for the radiation, remain valid.

If we regard the energy equations, the influence of this difference on the particle densities can be neglected if the important processes such as excitation and heat transfer processes are dominated by collisions and not by radiation. For this reason a sufficient particle density of colliding particles is necessary. Due to their higher mobility in comparison to that of the heavy particles, electron number density is the important quantity. The electron number density required for LTG depends on the temperature and the excitation state up to which the LTG should be valid. Additionally, the highest

ionization stage that is regarded is important. For example, a typical minimum electron density for LTG for argon up to complete single ionization and at a temperature of $T = 20000$K is given by $n_e = 4 \cdot 10^{17} \mathrm{cm}^{-3}$.

Regarding extremely rarified plasma states, not even LTG can be expected in every region of the jet and the plasma is in thermal and thermodynamic non-equilibrium. Here, thermal non-equilibrium means that the temperatures of the electrons and the heavy particles are different and that the molecules have different values for rotational, vibrational and electronic temperatures.

Even in these non-equilibrium cases, the Boltzmann distribution for the rotational and vibrational energy can be valid with the corresponding temperature T_{rot} or T_{vib} as the determining parameter for the distribution function. In thermodynamic non-equilibrium, the chemical composition of the plasma does not correspond to the equilibrium composition because the changes in temperature are often so fast that the chemical reactions cannot follow.

Depending on the plasma state, non-intrusive diagnostics can be applied to detect and characterize the plasma state. The quantities as e.g. the rotational or vibrational temperatures of a plasma molecule, cannot be accessed with probe measurements, because the plasma state would be changed by the probe. Therefore, non-intrusive diagnostics are an enormous asset for the characterization of plasma flows particularly at low pressures.

3.2 Theoretical Basics

In gases and plasmas at low pressures which are excited to emit light, the emission is mainly caused by single atoms and molecules. Thus, the properties of the emitted radiation allow conclusions to be drawn about the emitting particles. In this case, radiation occurs mainly at single discrete wavelengths - the so-called spectral lines. The number of lines for molecules of one species normally outnumbers the number of lines caused by a certain atom. The resulting intensity distribution as a function of the wavelength is called emission spectrum. There are several possibilities to excite atoms and molecules to emit radiation:

- In flames, light arcs and sparks, the atoms are excited by collisions due to their high thermal energy.
- In discharges, the excitation is caused by collisions with electrons and ions which possess high kinetic energy due to acceleration processes within an electric field.
- Excitation induced by radiation at short wavelengths such as UV or Röntgen-radiation.

Since a plasma jet of a plasma thruster is already excited, emission spectroscopic methods are rather easily applicable. However, beginning in the order as stated in the general remarks, one has to consider first the origin of electromagnetic radiation. And this is rather simple: Each body with a surface temperature above 0 K emits electromagnetic radiation. Measurement instruments that determine the surface temperature from this thermal radiation are called radiation thermometers or pyrometers. The observed wavelength region reaches from 10^{-7} to 10^{-5} m, which also covers the narrow region of visible light.

The basic quantities are the *radiant energy flux* ϕ given by the emitted energy dW during the time dt

$$\phi = \frac{dW}{dt} \tag{43}$$

and the *radiant exitance* M which describes the radiation that is emitted by the surface element dA into a solid angle of 2π:

$$M = \frac{d\phi}{dA} \tag{44}$$

If the *radiant exitance* is observed at a single wavelength *spectral radiant exitance* M_λ is obtained which can be calculated using *Planck's law*:

$$M_{\lambda S} = \frac{2\pi c^2 h}{\lambda^5 \left(e^{\frac{ch}{\lambda k T}} - 1 \right)} \tag{45}$$

h: *Planck's constant* ($6.6256 \cdot 10^{-34}$ Js)
c: Speed of light in vacuum ($2.9979\ 10^{8}$ m/s)

The integration of $M_{\lambda S}$ of a black body over all wavelengths yields, according to the *Stefan Boltzmann law*, the *radiant exitance of a black body* M_S

$$M_S = \int_{\lambda=0}^{\infty} M_{\lambda S}\, d\lambda = \sigma T^4 , \tag{46}$$

with σ, the Stefan Boltzmann constant ($5.669 \cdot 10^{-8}$ $Wm^{-2}K^{-4}$). Fig. 37 shows the spectral radiant exitance of a black body for different temperatures within the important wavelength region. If a non black body is observed, the spectral radiant exitance has to be reduced according to the spectral emissivity of the observed surface. The above mentioned radiation laws already show the main problems of radiation thermometry:

- According to the *Stefan Boltzmann law*, the thermally emitted radiation remarkably decreases (proportional to T^4) with decreasing temperature.
- At low temperatures, the maximum of radiation is shifted to high wavelengths where disturbing influences on the measurement become high.
- The spectral emissivity of non black bodies depends not only on temperature and wavelength but also on the material itself.
- Besides the radiation emitted by the observed surface, disturbing radiation of reflected or transmitted radiation emitted by other radiators can influence the measurement.

If radiation interacts with a surface, reflection, absorption and transmission occur. The ratios of absorbed,

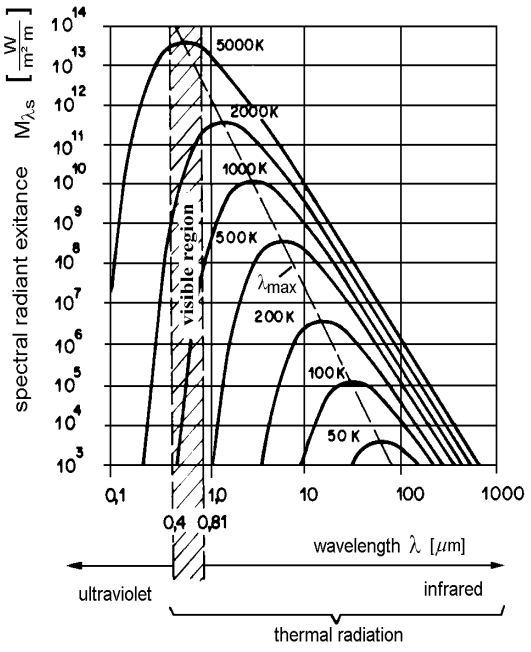

Figure 38: Spectral radiant exitance of a black body.

transmitted and reflected radiant energy fluxes to the incoming radiant energy flux are defined as (absorptance, transmittance, reflectance)

$$\alpha = \frac{\phi_a}{\phi},\ \tau = \frac{\phi_{tr}}{\phi},\ \rho = \frac{\phi_r}{\phi} \tag{47}$$

According to the above-mentioned definitions, the word spectral is added if these quantities refer to monochromatic radiation.

$$\alpha_\lambda = \frac{\phi_{\lambda,a}}{\phi_\lambda},\ \tau_\lambda = \frac{\phi_{\lambda,tr}}{\phi_\lambda},\ \rho_\lambda = \frac{\phi_{\lambda,r}}{\phi_\lambda} \tag{48}$$

They are functions of the wavelength and depend on the material, its surface structure and the temperature. They are coupled by the relation

$$\alpha + \tau + \rho = 1,\ \ \alpha(\lambda) + \tau(\lambda) + \rho(\lambda) = 1 \tag{49}$$

Additionally, according to *Kirchhoff*, the emissivity is equal to the absorptance for all bodies:

$$\varepsilon(T,\lambda) = \alpha(T,\lambda) \tag{50}$$

A black body will absorb all incoming radiation and has therefore an absorptance and due to this equation also an emissivity of 1. If one changes from the observation of a solid to a gas ensemble, i.e. going into more detail than the Planck curve (Fig.37), the problem of the discrete quantized energy level of the emitting or absorbing atom has to be considered. This is what Planck proposed in the famous formula (44). The following paragraph explains the microscopic view of the atom and molecule radiation.

3.2.1 Discrete Energy Levels of Atoms

This section gives an overview of the basic processes for the excitation of atoms [47, 46]. The emission and absorption at single lines is explained by the model of *Bohr*, who found that atoms can only exist at discrete energy values which correspond to special orbits of the electrons around the positively charged nucleus (see Fig. 38). Although his model is – from a pure physical standpoint – not correct, it is sufficient for experimenters to understand and model the problems occurring in plasma flows. The basic principle is, that Energy can be absorbed or emitted if an electron changes its orbit from one energy level to another one. In this case the energy

$$E_{nm} = h\nu = \frac{hc}{\lambda} \tag{51}$$

is either absorbed or emitted in form of electromagnetic waves of the frequency ν which is equivalent to the wavelength λ. Here, h is *Planck's constant* and c the speed of light in the observed medium. Only transitions between allowed energy values are possible. The allowed energy values are called energy levels and are characterized by the indices n and m in the above equation. This means an atom can only absorb radiation if it passes the transition from the energy level E_m to the higher energetic level E_n where its electron is at a higher energetic orbit (see Fig. 38). On the other hand, an atom at the state E_n emits radiation if its electron falls down to a lower energetic orbit with the energy E_m (see Fig. 38).

The time during which the electrons stay in the higher energetic state is limited to the life-time of the excited state which is characteristic for each excited state. This time, which is equivalent to the time between absorption and emission, is normally very short, in the range of nanoseconds and below.

The amount of radiation occurring during a transition is defined by an emission coefficient ε_ν which is defined as the energy of the radiation per time and solid angle emitted at the frequency ν by a unity volume. For a spontaneous transition of an excited electron at an energy level n to a lower level m, the emission coefficient ε_{nm} can be calculated as:

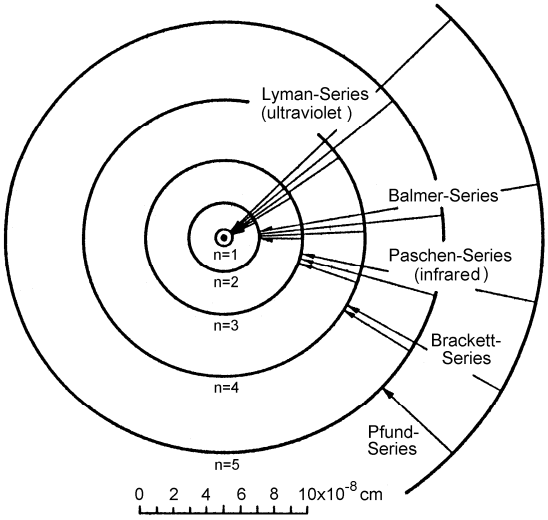

Figure 39: Bohr model of the hydrogen atom with the first five spectral series.

$$\varepsilon_{nm} = \frac{1}{4\pi} h \nu_{nm} A_{nm} n_n \tag{52}$$

Here, A_{nm} is the *Einstein transition probability* between the excited states m and n while n_n is the number density of the particles in the excited state n. The Einstein probability can be understood as the probability that a transition will occur. According to equation (50), the transition from the energy level n to a lower level m produces emission of the frequency ν. In reality, the emission occurs within a frequency interval $\delta\nu$. This phenomenon is called line broadening. Therefore, the emission coefficient ε_{nm} of a spectral line with the linewidth $\delta\nu$ has to be written as:

$$\varepsilon_{nm} = \int_{\nu}^{\nu+\delta\nu} \varepsilon_{\nu} d\nu \tag{53}$$

The different broadening mechanisms will be described in a following section.

Kirchhoff and *Bunsen*, who laid the foundation for spectral analysis, realized that each element emits its own characteristic spectrum. The spectral lines of one species can be sorted into series and are described formally by a so-called series formula. In the simplest case of the hydrogen atom with only one electron, each spectral line fulfills the equation:

$$\frac{1}{\lambda} = R_H \left(\frac{1}{n_1^2} - \frac{1}{n_2^2} \right). \tag{54}$$

Here, R_H is the so-called *Rydberg-constant* ($R_H = 2\pi^2 m_e e^4/(h^3 c) = 109677{,}581\ \mathrm{cm}^{-1}$), where the index H stands for hydrogen. n_1 and n_2 are integer numbers and represent the numbering of the energy levels where $n_1 < n_2$ and n_1 is constant within one series.

The emission spectrum of hydrogen consists of the following series (named after the scientist who found these lines (experimentally!)):

Lyman-Series (UV)	$n_1 = 1 \quad n_2 \geq 2$
Balmer-Series (visible if $n_2<8$)	$n_1 = 2 \quad n_2 \geq 3$
Paschen-Series (infrared)	$n_1 = 3 \quad n_2 \geq 4$

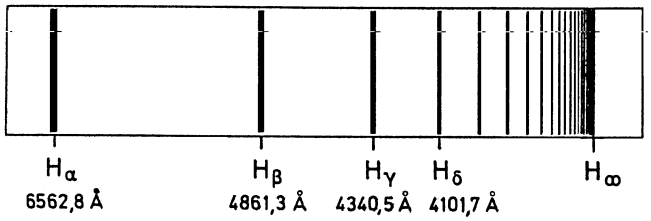

Figure 40: Balmer-series of hydrogen.

Brackett-Series	$n_1 = 4 \;\; n_2 \geq 5$
Pfund-Series	$n_1 = 5 \;\; n_2 \geq 6$

Fig. 38 explains the origin of the different series. Normal hydrogen, where all atoms are at the ground level (n=1), can absorb radiation only in the Lyman-series. The absorption at other spectral lines requires the existence of excited states which means that atoms exist where the electron already stays in the levels $n_1 = 2$ or $n_1 = 3$ and so on.

With rising n_2 the spectral distance between lines of one series decreases more and more. For $n_2 \rightarrow \infty$ the borders of the series are given by:

$$\lambda_{\infty} = \frac{n_1^2}{R_H} \tag{55}$$

Beyond this border, the spectrum is no longer characterized by single emission lines but by continuous emission. The radiation is now no longer caused by transitions of excited atoms. It originates when free electrons are captured by ions (radiation by recombination) or when ions or electrons are accelerated or decelerated by electric fields. The line emission is also called bound-bound radiation while radiation by recombination is called free-bound. Radiation caused by acceleration and deceleration processes is termed free-free. For atoms other than hydrogen the formulation of analytic series formulas that cover all possible spectral lines becomes rather complicated due to the fact that more than one electron exists. The transitions occurring in the more complex atoms are all based only on the outer electrons. All filled subshells do not contribute to the definition of transitions.

3.2.2 Energy Levels of Molecules

Additionally to the electronic transitions of atoms, molecules have the two degrees of freedom of rotation and vibration. Still, the emission occurs at discrete energies which results in an emission spectrum consisting of single spectral lines. But in comparison to the atoms, the number of transitions allowed is much higher and the spectral distance between the single lines is much smaller. A measurement of single lines is only possible with extremely high resolution spectrometers. The wavelength of each emission line is not only a function of the upper and lower electronic states of the transition but also of the upper and lower rotational and vibrational energy levels. In molecular spectroscopy usually the wave number ν which is the inverse wavelength is used to characterize the single emission lines. The corresponding wave number for a molecular transition is proportional to the total change in energy:

$$\tilde{\nu} = \frac{1}{hc}\left(\Delta E_{el} + \Delta E_{vib} + \Delta E_{rot}\right) \tag{56}$$

Here, ΔE_{el}, ΔE_{rot} and ΔE_{vib} are the changes in electronic, rotational and vibrational energy, respectively. Obviously, the more numbers of atoms the molecule has the more rotational and vibrational states are possible. For rarified flow diagnostics with high enthalpies, larger molecules are dissociated rather quickly and therefore the observation of molecules with more than two nuclei is seldom. In the following, only two atomic molecules are considered.

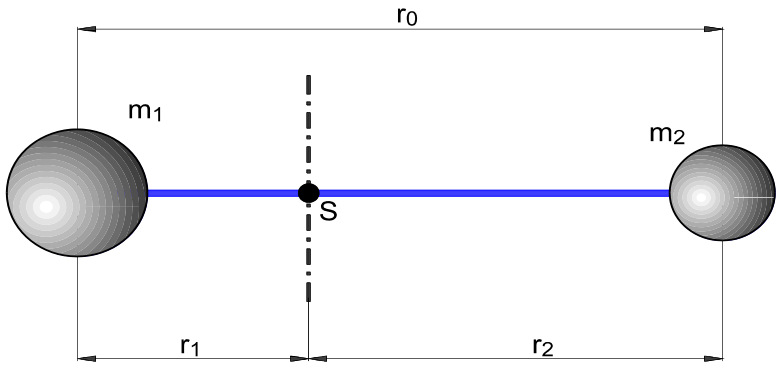

Figure 41: Molecule as rotating dumb-bell.

The effect of the electronic transition can still be reduced to the corresponding energy difference of the upper and lower electronic state and is usually taken from literature. The degrees of freedom for rotation and vibration can be described by analytical models which allow the calculation of the possible energy levels and the quantum physical interpretation of the obtained spectra.

Rotational Energy Levels

Fig. 40 shows a simple model for a two-atomic molecule which is simulated as a dumb-bell. Here, the atoms are regarded as point masses m_1 and m_2, the connection with the length r_0 is regarded as boundless, massless and rigid in a first approach. The molecule rotates around the center of mass *S*. In this system, the rotational energy can be calculated using the equations of classical mechanics:

$$E_{rot} = \frac{1}{2} j \omega^2 \tag{57}$$

Here, j is the moment of inertia and ω the angular velocity of the rotation. For the simple model of the rigid rotation, j becomes:

$$j = m_1 r_1^2 + m_2 r_2^2 \tag{58}$$

The assumption that $m_1 = m_2 = \mathrm{m}$ and therefore $r_1 = r_2$ which is actually valid for homonuclear molecules results in:

$$j = \frac{m}{2} r_0^2 \tag{59}$$

Equations of classical mechanics would say that the rotational energy can have any value. But again, in quantum mechanics only discrete energy levels exist and the fundamental description is based on the so-called *Schrödinger equation*. For the rotation this yields:

$$E_{rot} = \frac{h^2}{8\pi^2 j} J(J+1)\,. \tag{60}$$

with J = 0, 1, 2, ...

As already mentioned, h is *Planck's constant* while J is the *rotational quantum number*. In molecular spectroscopy, the energy terms are usually given in terms of wave numbers which is done by normalization by hc. Therefore, the latter equation is equivalent to:

$$F(J) = \frac{E_{rot}}{hc} = B_e J(J+1) \tag{61}$$

The rotational constant B_e is one of the most important constants in molecular spectroscopy. It is inversely proportional to the moment of inertia j and gives for a known atomic mass the bonding length of the molecule which is a fundamental variable of the inner construction of the investigated molecule. The selection rules of quantum mechanics only allow transitions with neighboring rotational quantum numbers which means the maximum change in J can be 1 or -1. The resulting series of emission lines are called branches and are named P-, Q- and R-branch. The possible changes in rotational energy become:

P-branch (ΔJ=1) $$\Delta E_{rot} = \frac{h^2}{8\pi^2 j} 2(J+1) \tag{62}$$

Q-branch (ΔJ=0) $$\Delta E_{rot} = 0 \tag{63}$$

R-branch (ΔJ=-1) $$\Delta E_{rot} = -\frac{h^2}{8\pi^2 j} 2J \tag{64}$$

If the change in the total angle remains constant within the transition, the Q-branch is not allowed. The contribution of the rotational transition to the wave number of the emission line is given by:

$$\tilde{\nu}_{rot} = \Delta F(J) = \frac{\Delta E_{rot}}{hc} \quad J = 0,1,2,... \tag{65}$$

In the model of the rigid rotating dumb-bell, the wave numbers within one branch increase linearly with a rising quantum number. This results in constant spectral differences between the single rotational lines in terms of wave numbers. In reality, the connection between the two nuclei is not rigid as assumed within the above equations. This yields a deformation of the molecule with rising centrifugal force which can be taken into consideration by implementing a second order correction term yielding the model of a non-rigid rotating dumb-bell. Here, the constant D_e is implemented which considers the extension of the distance between the nuclei with increasing rotational energy. D_e is an experimentally determined constant which varies for different species and for different electronic states. Equation (60) transforms into:

$$F(J) = B_e J(J+1) - D_e [J(J+1)]^2 . \tag{66}$$

For most experimental considerations of rarefied flows, the constants needed in the above expressions are accurately known. A large database can be found at NIST (National Institute of Standards and Technology).

Vibrational Energy Levels

In addition to the rotation around the center of mass, a vibration of both atoms along the molecular axis is possible. In the most simple way, this vibration can be described as the motion of a reduced mass μ around an equilibrium position r_0 with $\Delta r = r - r_0$. The reduced mass is defined as

$$\mu = \frac{m_1 m_2}{m_1 + m_2} \tag{67}$$

and the spring constant k the well-known differential equation of the harmonic oscillator is obtained:

$$\mu \frac{d^2(\Delta r)}{dt^2} + k\Delta r = 0 . \tag{68}$$

The solution to this equation is an oscillation with the frequency:

$$\nu_{osz} = \frac{1}{2\pi}\sqrt{\frac{k}{\mu}} . \tag{69}$$

Similar to the model of the rotating dumb-bell, the fundamental equation for quantum mechanical systems,

the Schrödinger equation, applied on the harmonic oscillator yields again quantized vibrational energies. The vibrational energy term becomes:

$$E_{vib}(\upsilon) = h\nu_{osc}\left(\upsilon + \tfrac{1}{2}\right) \tag{70}$$

with υ=0, 1, 2, ...

Again, normalization by *hc* can be done yielding:

$$G(\upsilon) = \frac{E_{vib}(\upsilon)}{hc} = \omega\left(\upsilon + \tfrac{1}{2}\right) \tag{71}$$

The energy scheme of a linear harmonic oscillator consists of equi-distant steps $h\nu_{osc}$ with a minimum energy value $h\nu_{osc}/2$. υ is the vibrational quantum number and ω represents the vibrational frequency. In contradiction to the rotation, transitions between vibrational energy levels with quantum number differences higher than 1 are also allowed. The wave numbers of pure vibrational lines (which means that both upper and lower level belongs to the same electronic state and that no change in rotational energy occurs which is equivalent to ΔJ = 0) are given by:

$$\tilde{\nu} = \frac{\Delta E_{vib}}{hc} = \frac{\upsilon_1 - \upsilon_2}{c}\nu_{osc} \tag{72}$$

From this equation, the distances between the single lines are supposed to be multiples of the ground frequency divided by *c*. Again, this expectation is not fulfilled completely in reality which can be explained by the fact that a molecule has to be seen as a so-called *anharmonic oscillator*. To illustrate this coherence, the potential curves for both harmonic and anharmonic oscillators are plotted in Fig. 41. They show the potential of the forces between the nuclei as a function of the nuclear distance. The quantisized vibrational energy levels E_{vib} can be seen as horizontal lines of constant energy as drawn in Fig. 41. In the case of a harmonic oscillator, the potential curve appears as a symmetrical parabolic function. If one nucleus is regarded as fixed, the other one would oscillate like a ball which rolls along the curve. The points where the energy levels cross the curve are the reversal points of this oscillation. This model does not agree with reality in two essential points. First, in the simple model there is no theoretical reason that the distance between the nuclei could not decrease to zero. In reality, this is physically not possible because the electrostatic forces between the two positively charged nuclei would rise very quickly. On the other hand, the potential is not allowed to rise until infinity with increasing distance between the nuclei. The force between the nuclei which is produced by the electrons is only decreasing with rising distance until the molecule becomes dissociated. As can be seen from the potential curves, reality is better represented by the model of the anharmonic oscillator. In this case, the energy levels are no longer equidistant.

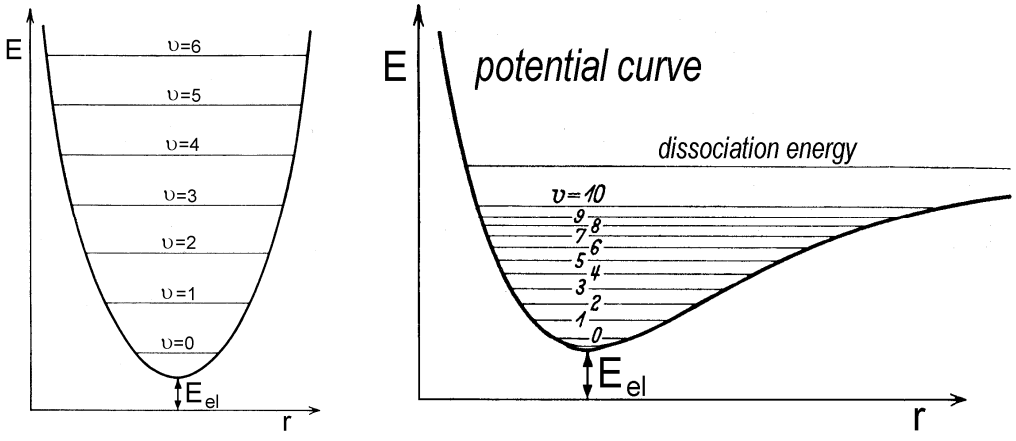

Figure 42: Harmonic (left) and anharmonic (right) oscillator.

3.3 For the experimenter: The Molecular Spectrum

The emission line in molecular emission spectra is based on the superposition of electronic, vibrational and rotational transitions. The wave number of each emission line is given by the total change in energy. Often, the upper state of a transition is characterized by ´ and the lower state by ´´. Using this nomenclature, equation (55) can be written as:

$$\tilde{\nu} = \Delta T^{el} + \Delta G + \Delta F \tag{73}$$

or

$$\tilde{\nu} = T'^{el} - T''^{el} + G'(\upsilon') - G''(\upsilon'') + F'(\upsilon', J') - F''(\upsilon'', J'') \tag{74}$$

with: T^{el} normalized electronic energy

$G(\upsilon)$ normalized vibrational energy

$F(\upsilon J)$ normalized vibrational energy

and $\Delta T^{el} >> \Delta G >> \Delta F$

Depending on the question which part of the spectra (purely rotational, rovibrational) is observed, Eq. (73) has to be reduced. Furthermore, not every combination of v' and v'' is allowed according to the quantum mechanical selection rule. A famous representation of the different emission lines is a plot of the rotational quantum numbers versus the wave number. These resulting graphs are called Fortrat parabolas. Similar to the wave number, the intensity of an emission line is represented by a superposition of electronic, vibrational and rotational transition intensity. But the amount of light absorbed or emitted by atoms or

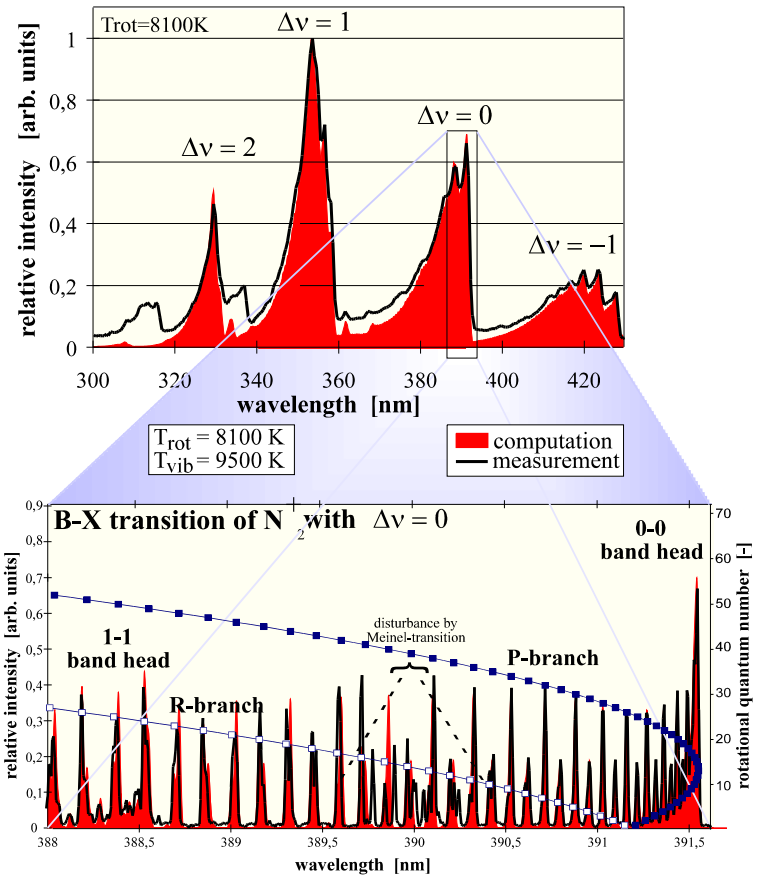

Figure 43: Band structure of the N_2^+-molecule measured in front of a hot SiC material sample (T_{Wall} = 1580 °C).

molecules depends evidently on the population in that level. If the system is in thermal equilibrium, then the populations of atoms or molecules in the energy levels follow the Boltzmann distribution:

$$N_i = N \frac{g_i e^{(-E_i/kT)}}{\sum_i g_i e^{(-E_i/kT)}} \tag{75}$$

Under the assumption of this Boltzmann distribution, the intensity of each emission line is given by:

$$I_{\upsilon'J'-\upsilon''J''} = K\nu^4 S_J f_{alt} e^{\left[-T^{el}\frac{hc}{kT_e}\right]} e^{\left[-G'(\upsilon')\frac{hc}{kT_{vib}}\right]} e^{\left[-F'(\upsilon'J')\frac{hc}{kT_{rot}}\right]} \tag{76}$$

Here K is a function of the electronic transition moment and the partition functions for the electronic, vibrational and rotational transition and therefore of electronic, vibrational and rotational temperature but not of rotational or vibrational quantum number. For a given plasma state, K is a constant.

S_J is the Hönl- London factor which describes the statistical weights for the transition. It is a measure how the radiation energy is distributed over the different rotational modes. To illustrate the appearance of a molecular spectrum according to this theory, Fig. 42 shows the N_2^+ First Negative band system in low resolution with the different band heads and the fine structure of the Δν=0 band in high resolution including the 0-0 and the 1-1 band head. The dark line represents a measurement in front of a hot material sample that reached a steady state wall temperature of 1580 °C; the gray areas are a numerical simulation of the emission. The Fortrat parabolas for the 0-0 vibrational transition are added to the fine structure diagram. The molecular band is divided into different parts which are formed by single rotational lines. In the case of N_2^+ these bands are degraded to the violet which means that rotational lines with rising rotational quantum number are shifted to lower wavelengths. All rotational lines which result from the transition from the vibrational level 0 to the vibrational level 0 lie close together and form the 0-0 vibrational band. The next band head at lower wavelengths belongs to the 1-1 transition. All higher vibrational transitions with Δν=0 are adjacent. Together they form the Δν=0 band system. Systems with other differences in vibrational quantum number such as Δν=-2, Δν=-1, Δν=1 and Δν=2 are similarly formed.

3.3.1 Line Broadening

All the models explained so far result in a wavelength value where the emission is expected and a value for the intensity. However, the real measurement shows a more or less broad line profile. This is due to the fact that the theoretically found value is disturbed in different ways, summed under the term Line Broadening:

The *natural line-width* in a plasma without motion at low pressure (which means that collisions between particles are rare) is determined by *Heisenberg's law of uncertainty* and is in the dimension of 10^{-5} nm which normally can be neglected in comparison to the other broadening mechanisms. This effect is always present.

The other most important processes for line-broadening are:

- Doppler effect
- Interaction with other particles (pressure broadening such as resonance, Stark and Van der Waals broadening)
- Zeemann effect caused by disturbing magnetic fields. The Zeemann effect gains importance if strong magnetic fields are used.

The Doppler and the Stark effect are used in spectroscopy to determine thermodynamic quantities. However, very highly resolved measurements are indispensable for these measurements.

Doppler Broadening

The motion of radiating particles causes a wavelength shifting of the emitted spectral line (Doppler shift). Within plasma without flow velocity, the velocity values and directions of the single particles are statistically distributed. A superposition of the different Doppler shifts yields a broadened intensity profile. If the Doppler displacement is strong in comparison to the other broadening mechanisms, the translational temperature of the emitting particles can be determined from the Doppler half width of the emission lines. For this purpose, a high resolution spectrometer is needed. A Fabry-Perot interferometer fulfills this requirement.

Broadening by Interaction with other Particles

Neutral particles, electrons and ions in the plasma surrounding the emitting particles can cause disturbances of the emission which is proportional to the partial pressures of the emitting and disturbing particles. This pressure broadening can be divided into resonance, Stark and Van der Waals broadening. To describe this procedure, the disturbing particles are mostly regarded as classical particles which move in the simplest case on straight lines with the velocity v. From a distance ρ to the emitting particle, the effect of the disturbing particle can be noticed. Therefore, the time during which the disturbance occurs is on the order of

$$\Delta t \approx \frac{\rho}{v}. \tag{77}$$

If Δt is short in comparison to the time between two disturbances, which is normally valid for fast particles such as electrons, the disturbances can be regarded as collisions and interpreted by collision theories. In this case, the emitting particle is regarded as a harmonic oscillator.

If a disturbing particle passes the emitting particle, the phase of the above-mentioned oscillation is changed. A Fourier analysis of the phase-disturbed oscillation gives a dispersion profile with the half width $\Delta\nu_H$. The maximum value of this line profile is shifted by $\Delta\nu$ compared with the profile of the undisturbed line with the frequency ν_0. At the regarded plasma states, the half-width is mainly determined by the Stark effect which covers the interaction of charged particles caused by the forces due to their electric field.

In comparison to the emission without disturbing effects caused by an electric field, the emission of atoms in an electric field of the strength E is shifted by the frequency $\Delta\nu$:

$$\Delta\nu(E) = \frac{1}{2\pi} C^* E^2 \tag{78}$$

Here, C^* is the so-called Stark effect constant. A disturbing electron in the distance r to the emitting particle produces an electric field at the location of the particle with the strength

$$E = \frac{1}{4\pi\varepsilon_0}\frac{e}{r^2} \tag{79}$$

and therefore causes a frequency displacement of the above described oscillator of:

$$\Delta\nu(r) = \frac{1}{2\pi}\left(\frac{e}{4\pi\varepsilon_0}\right)^2 C^* \frac{1}{r^4} = \frac{C_W}{r^4} \tag{80}$$

Therefore, the line broadening due to the Stark effect is proportional to $\sim r^{-4}$ with the constant C_w. So, the equations for the line displacement $\Delta\nu_V^{ST}$ and the half width $\Delta\nu_H^{ST}$ in a plasma with the electron density n_e and the average thermal velocity $\vec{v}$ can be written as:

$$\Delta\nu_v^{St} = \frac{1}{2\pi} 9.85 C_W^{2/3} \bar{v}^{1/3} n_e$$
$$\Delta\nu_H^{St} = \frac{1}{2\pi} 11.37 C_W^{2/3} \bar{v}^{1/3} n_e \qquad (81)$$
$$with\, v = \sqrt{\frac{8}{\pi} kT \left(\frac{1}{m_e} + \frac{1}{M} \right)}$$

Here, M is the molecular mass of the corresponding ion. In the above equations, only the influence of the electrons on the emitting particles is taken into account. Due to their higher mass and their therefore lower velocity, the influence of the heavy particles can often be neglected. Meanwhile, the simple model as described above has been refined by quantum mechanical considerations of the collision processes but the principal results remain valid.

Due to their large line width, especially the Balmer lines of the hydrogen atom are well-suited to determine the electron density from the line broadening due to the Stark effect. Fig. 43 shows the H_α-line at two different plasma states. The line width of the Balmer line H_β is even stronger than that of the H_β-line. At an electron density of $n_e = 10^{23}$ m^{-3} and a temperature of $T = 10000$ K the half width of the H_β-line is 45 Å.

For plasmas without hydrogen, determining the electron density from the Stark broadening is often difficult or even impossible because the effects of other broadening mechanisms (especially the effect of Doppler broadening) are stronger than the Stark effect. Sometimes, small amounts of hydrogen can be added to the plasma to enable the determination of the electron density as described above.

3.4 Emission Spectroscopy

Emission spectroscopy is one of the most important methods of plasma diagnostic measurements with the great advantage of being completely non-intrusive. The emission spectrum contains information about

- the wavelength of the emitted radiation
- its intensity
- the intensity profile of each line
- the intensity distribution of the continuous radiation

To obtain information about thermo-chemical processes, the evaluation of the measured data can become

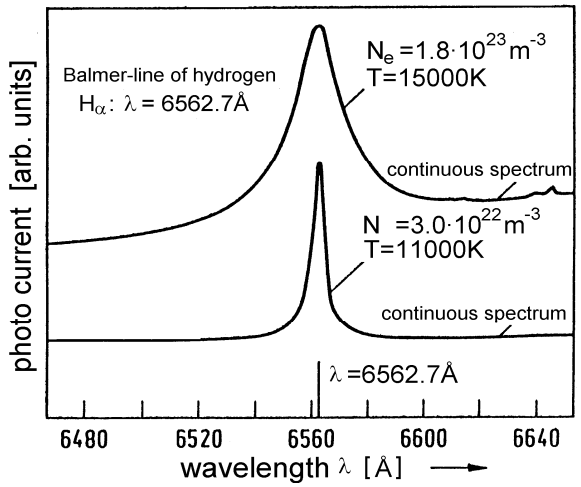

Figure 44: Line broadening due to the Stark-effect.

rather difficult. Generally, the applications of emission spectroscopic measurements can be divided into three sections:

- The identification of different atoms and molecules within the plasma
- The determination of thermodynamic quantities such as temperatures and particle densities
- Gaining information about excitation and recombination processes within the plasma

For the applicability of emission spectroscopy as a plasma diagnostic method to determine thermodynamic quantities, a particular setup and important calibration steps have to be considered. Therefore, the following section first gives an overview about the basic experimental setup and the calibration steps before some exemplary results are shown.

3.4.1 Experimental Setup

The results of emission spectroscopic measurements are influenced by different factors. Generally, the measured data cannot be used for further evaluation without any corrections. Although modern spectrometers and monochromators are normally wavelength calibrated, an additional wavelength calibration should be performed prior to each measurement because testing time is often limited and very expensive. In any case, a spectral intensity calibration (either relative or absolute) is necessary to enable a comparison of emission lines at different wavelengths or to determine thermodynamic quantities from the absolute intensity of the measured emission.

Measurements in different wavelength regions require different capabilities of the experimental set-up. For measurements of molecules in the ultraviolet wavelength region, the spectral transmittance of the optical elements of the experimental set-up and the spectral efficiency of the detector have to be optimized for utilization in the UV because at most plasma states the emission of the molecules is already weak. Fused silica lenses and windows as well as mirrors are the most commonly used optical elements. In any case, a spectral calibration of the set-up has to be done which will be described below.

At higher wavelengths up to the near infrared, the choice of materials for the optical elements is rather easy because most optical materials have sufficient characteristic properties in this wavelength region. On the other hand, most detectors suffer from decreasing efficiency close to the infrared especially if they are sensitive in the UV region. Another important disturbance is second order radiation. Due to self-absorption in air below 185 nm this effect gains importance only at wavelengths above 390 nm. To prevent the measured data from second order radiation, spectral filters are used to block radiation at

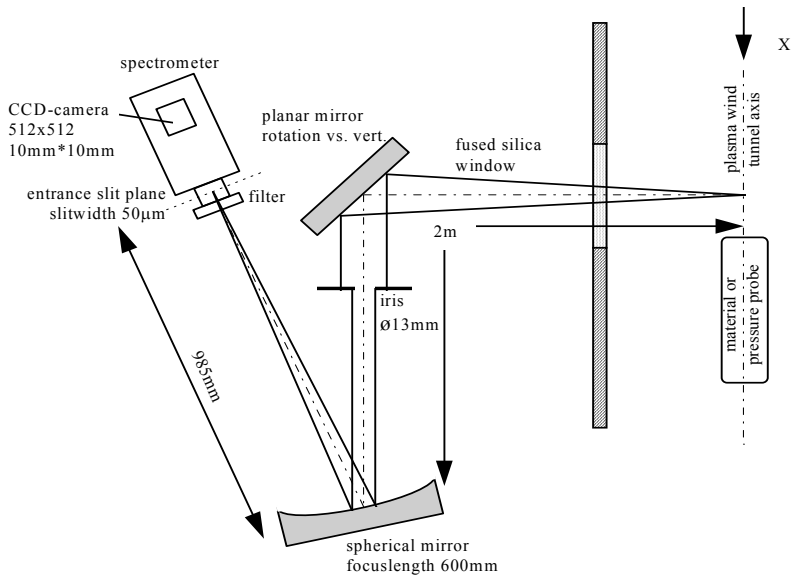

Figure 45: Typical experimental set-up for emission spectroscopic measurements [54].

wavelength below the region of interest.

Fig. 44 shows a typical setup for emission spectroscopic measurements. The emitted radiation is focused onto the entrance slit of a spectrometer where the spectral decomposition takes place. At the exit of the spectrometer, the transmitted light is collected by a detector. The focusing elements of the optical set-up have a remarkable influence on the results. In the set-up presented all lenses have been replaced by mirrors to minimize chromatic aberration which causes a shifting of the focus. If extensive wavelength ranges have to be detected, this shifting causes significant errors in the measured data. The mirrors are used for focusing and for adjusting the measurement position inside the vacuum tank. Because of the comparatively large focal length of 650 mm, a precise adjustment of the optics is an important requirement for a successful measurement. For the adjustment procedure, the detector is replaced by a laser. The laser light has to take the reverse optical path and enables both an adjustment of the optical axis and of the measurement position.

3.4.2 Wavelength Calibration

Generally, a wavelength calibration has to be done to relate the detector wavelength axis to the emission wavelength. Most spectrometer software offers a procedure to calibrate the single detector elements although a manual calibration is also possible. For this purpose, the radiation of a calibration lamp with emission lines at known spectral positions is measured. Fig. 45 shows the measured spectrum of a Hg-lamp which is one of the most commonly used calibration lamps. Usually, the spectrometer is adjusted until one of the known emission lines appears in the center of the detector array. Other known lines are used to perform a polynomial fit (second order is most sufficient) for the wavelengths of the other pixels.

3.4.3 Intensity Calibration

If the absolute intensity of the emission lines has to be detected, it is obvious that the sensitivity of the detector has to be calibrated. But even if only relative intensities have to be compared, at least a relative calibration has to be done. The calibration is done by measuring a calibration lamp with already calibrated continuous emission (e.g. a tungsten band lamp for the visible wavelength region or a deuterium lamp for the UV).

Sometimes, only the spectrometer-detector couple is intensity calibrated which is done by illuminating the whole entrance slit of the spectrometer with the light of a calibration lamp. In this case, the calibration lamp is placed directly in front of the entrance slit. The advantage is that the spectrometer-detector combination has to be calibrated only once for a given wavelength range. The disadvantage of this calibration is that all spectral transmissions of windows, filters and lenses in the optical path have to be

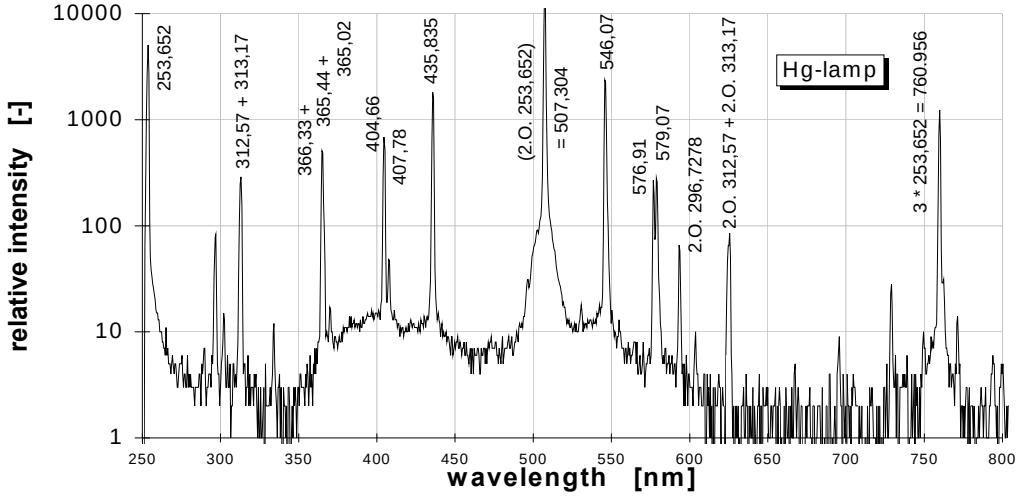

Figure 46: Spectrum of an Hg-calibration lamp.

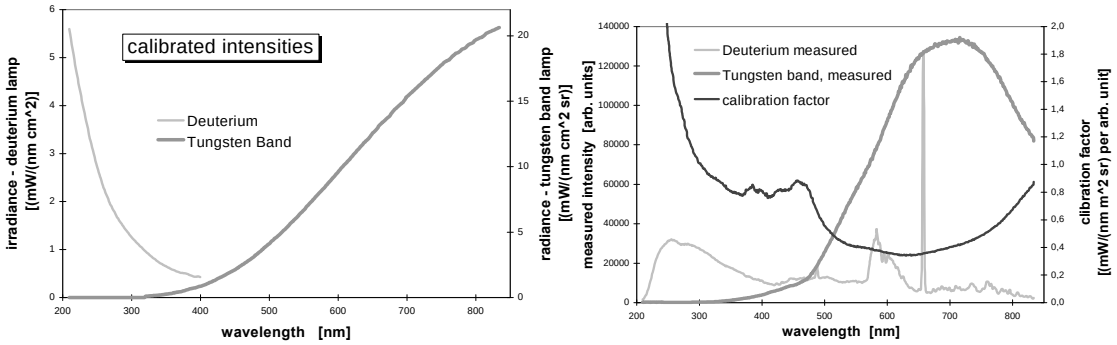

Figure 47: Calibrated intensities of the different lamps (left) and measurements (right) [54].

known accurately. Additionally, the solid angle and the imaging factor have to be included in the final evaluation.

The better but also more time consuming method is to place the calibration lamp at the measurement position and use the same optical path as in the measurement which has to be calibrated. In this case, all influences on the signal are included in the calibration procedure.

Fig. 46 shows the calibrated emission of two calibration lamps as tabulated by the manufacturer and the measured values. The correction factors for the single detector elements are included in the diagram. The emission of the tungsten band lamp drops down in the ultraviolet wavelength region where the deuterium emission is rather strong. On the other hand, the emission of the deuterium lamp is no longer continuous in the visible wavelength range. Thus, only a combined calibration using both lamps gives a valid correction factor. Since the deuterium lamp itself is calibrated to spectral irradiance, the correction factors have to be scaled by a constant factor to those of the tungsten band lamp which is calibrated to spectral radiance.

3.4.4 Determination of Local Quantities, Abel Inversion

A main disadvantage of emission spectroscopic measurements is the fact that the measured signal always consists of the integration along the line of sight as illustrated in Fig. 47.

The Abel inversion is a mathematical technique which allows a reconstruction of the local values from a vertical profile of measured (that means integrated) intensities $I(z)$ as long as rotational symmetry of the radiation within the measured volume is given.

The radiation of the plasma volume is described by the emission coefficient ε(r). The measured integrated intensity $I(z)$ is coupled to ε(r) by the *Abel equation:*

$$I(z) = 2\int_{r=z}^{R} \frac{r}{\sqrt{r^2 - z^2}} \varepsilon(r) dr \tag{82}$$

R is the radius of the measured volume while r is the local radius. Solving for ε(r) gives

$$\varepsilon(r) = -\frac{1}{\pi}\int_{z=r}^{\infty} \frac{(dI/dz)}{\sqrt{z^2 - r^2}} dz \tag{83}$$

In most cases an analytical solution is hard to find because a valid approximation of the integrated intensities is not available. Therefore, a numerical solution is used where the emission coefficient is considered to be constant over finite rings of the regarded volume. A refinement can be implemented if a linear transition between the measurement position is postulated to approximate the continuous course in the real plasma. Fig. 48 illustrates the principle of the numerical Abel inversion.

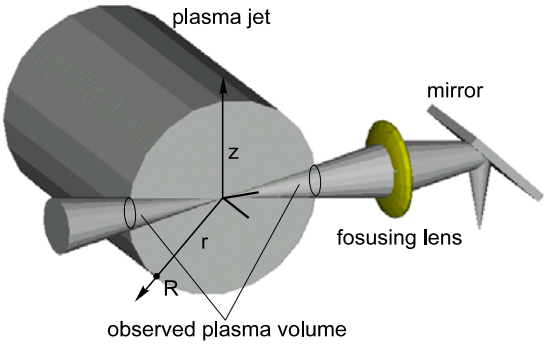

Figure 48: Typical geometrical configuration.

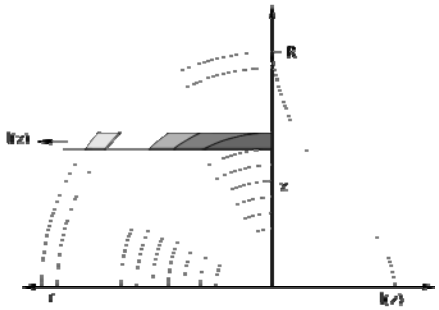

Figure 49: Principle of the Abel inversion.

Figure B2.1 shows the measured intensities I(z) and the Abel-inverted intensity i(r). The Abel-inverted intensities drop down to negative values at the borders of the plasma jet. Theoretically, this could be caused by absorption, but more likely these values are caused by numerical errors which can accumulate especially in the border region where intensities are rather low. Generally, the Abel inversion reacts very sensitively to functions which are not constantly differentiable. For this reason, a smoothing of the measured data often has to be performed first.

The principle discussed is easily applicable if the local intensity distribution within the plasma is of particular interest as it was postulated for temperature determination methods. The problem becomes more complicated if, in addition to the intensity distribution, the line profile also has to be resolved, for example to determine electron densities from Fabry-Perot measurements. Here, the line broadening changes over the cross section as the electron density changes.

The measured intensity I(z) within the Abel integral equation is not only described by the emission coefficient ε(r) but also by the line profile of the emission lines. The Abel equation becomes:

$$\varepsilon(r)\Delta\lambda_B^2(r) = \frac{1}{\pi}\int_{z=r}^{\infty} \frac{\left(d\left(I(z)\Delta\lambda_B^2(z)\right)/dz\right)}{\sqrt{z^2 - r^2}}dz \qquad (84)$$

This expression gives a relation between the integrally measured broadening $\Delta\lambda_B(z)$ of an emission line at the wavelength λ with the local broadening $\Delta\lambda_B(r)$. If ε(r) is known from a conventional Abel inversion; the local broadening can be calculated.

3.4.5 Exemplary results

The basic principles that determine the emission of atoms and molecules have been explained above. The spectrum emitted by the plasma can be regarded as a superposition of the emission of the different radiating species. Figs. 50 and 51 show the measured emission spectra of an air and a CO_2 plasma state with the most important radiating species in the wavelength region between 200 nm and 900 nm in a low

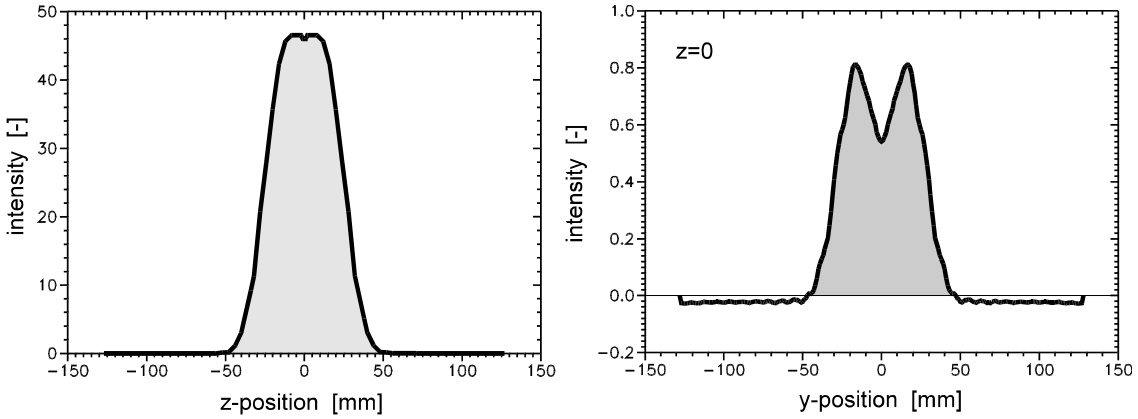

Figure 50: Exemplary measured (left) and Abel-inverted (right) intensity distribution.

resolution of 0.5 nm. The spectral emission as a function of the wavelength corresponds in the air plasma to that of an equilibrium plasma state at a temperature of T = 11700K but the emissions of the different species have been scaled by different constant factors to enable a graphical representation in a common diagram. The emissions of the atomic species have been reduced by a factor of 10^{-6} and the emissions of the molecular species NO, N_2 and O_2 have been amplified by factors of 10, 100 and 300, respectively.

Generally, the UV-region between 200 nm and 400 nm contains the radiation of most molecular species such as NO, N_2, O_2 and N_2^+ with the exception of the N_2 First Positive system. The strongest atomic radiation can be observed close to the infrared wavelength region above 700 nm. Fig. 51 shows the spectral simulation of a CO_2 plasma flow. It can be seen that the emission of CO is dominating the emission over the whole spectral range, while CN and C_2 have some spectral regions were the radiation is dominated by these species and other ranges (in the UV) where this radiation is not of importance. Here, absolute radiation quantities are shown, i.e. radiation intensity in W/(m²sr m) such that also the number densities can be analyzed [57].

3.4.6 Identification of Atoms and Molecules

Without a doubt, the identification of unknown elements using the wavelength of the emitted spectral lines is the oldest application of emission spectroscopic measurements. In plasma wind tunnels, the identification of different particles is of particular interest for:

- Proving the existence of ionized species
- Detecting erosion products of the electrodes which pollute the plasma
- Determining the plasma regions where recombination, dissociation or ionization processes occur (e.g. NO-formation due to catalytic effects).
- Detecting erosion products of the heat shield materials.

Fig. 52 shows two spectra recorded during the re-entry of the automated transfer vehicle ATV-1. It is an excellent example that the identification of atoms and molecules is of particular interest as here the main focus was to measure the distribution of the different fragments of the entering spacecraft and to find out which fragment consists in which metals, alloys or chemical hazards.

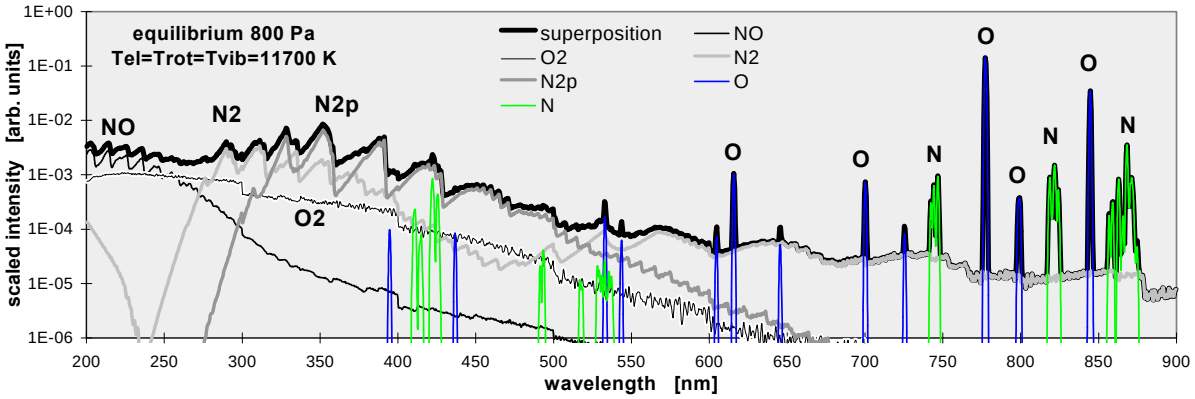

Figure 51: Superposition of the computed emission of the most important radiating species in an air plasma in the wavelength region between 200 nm and 900 nm [54].

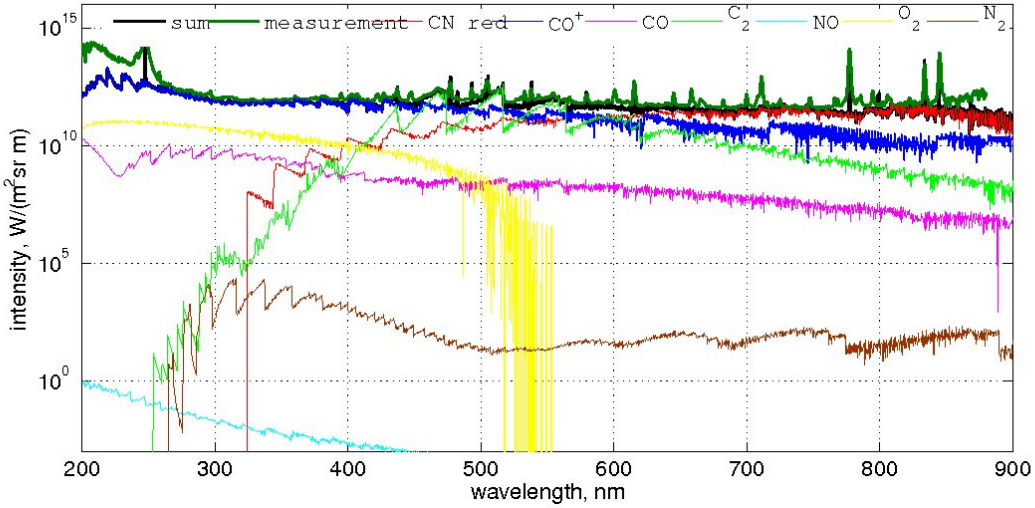

Figure 52: Superposition of the computed emission of the most important radiating species in CO_2 plasma in the wavelength region between 200 nm and 900 nm [58].

3.4.7 Temperature Determination from Atomic Radiation

The information about the plasma temperature is contained within the intensity and the shape of the spectral lines of the radiating species. Replacing the number density of the excited state n_n under the assumption of a Boltzmann distribution as introduced in equation (B2.35), the spectral emission coefficient ε_{nm} of a spectral line as introduced in equation (B2.2) can be written as:

$$\varepsilon_{nm} = \frac{1}{4\pi} h \nu_{nm} A_{nm} n \frac{g_n}{g_0} \exp\left(-\frac{E_n}{kT}\right) \tag{85}$$

If all quantities that remain constant for one species at the same plasma state are combined in the constant C which also contains common factors that influence the measured radiation such as the solid angle of the focusing system, an equation for the measured line intensity of the transition from state n to m is obtained:

$$I_{nm} = C \nu_{nm} A_{nm} g_n \exp\left(-\frac{E_n}{kT}\right) \tag{86}$$

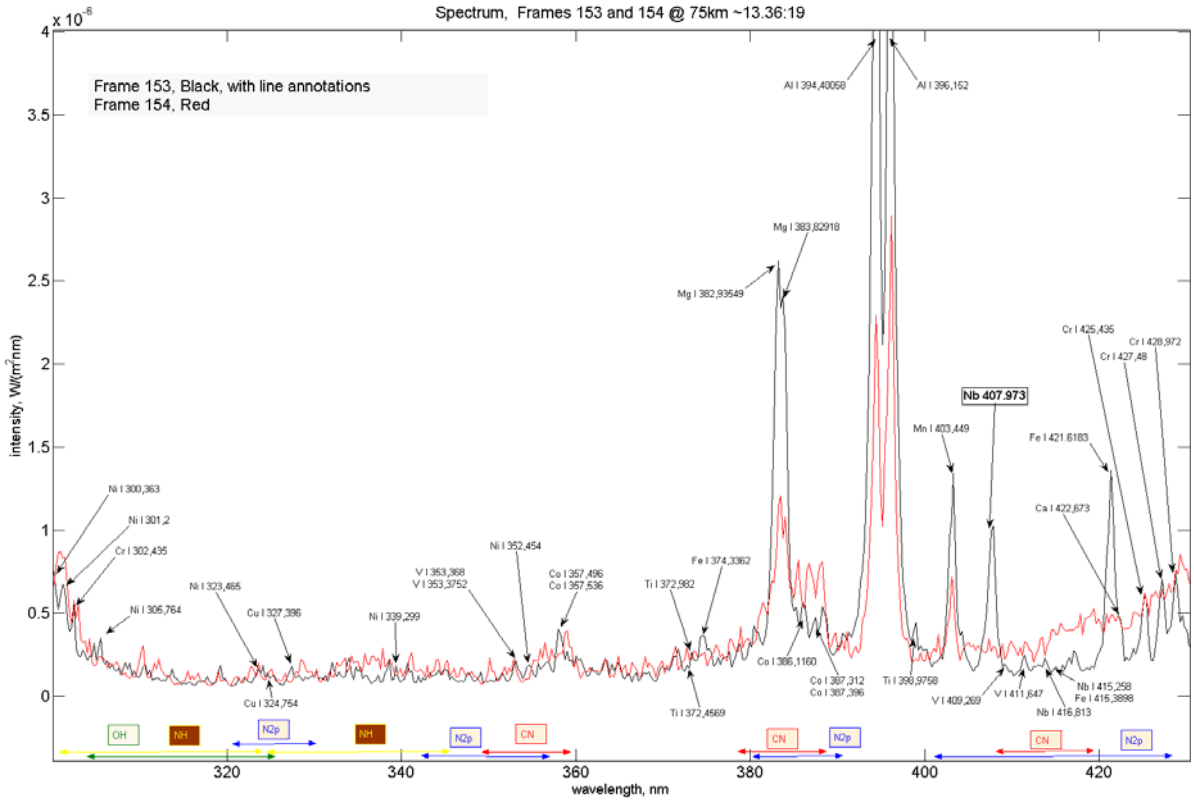

Figure 53: Emission spectra measured during the destructive re-entry of ESA ATV-1 [58].

or

$$\ln\left(\frac{I_{nm}}{\nu_{nm} A_{nm} g_n}\right) = \ln(C) - \frac{E_n}{kT} \qquad (87)$$

Even without knowledge of the particle density, a determination of the temperature by a comparison of two emission lines can be performed. For this method, the fact is applied that the above equation formally appears as a straight line equation $y = b + mx$ with y and x being the logarithmic expression and the excitation energy respectively and where the slope contains the desired temperature. With only two points which means two emission lines the slope and therefore the temperature can be determined. To increase the quality of the measurement, usually more than two lines are used. This method is called Boltzmann plot and can be used both for determining atomic and molecular temperatures as explained in detail in the following section. It should also be noted that if the two lines are energetically close to each other, the determination of the temperature is difficult. As an example, for the most commonly observed transitions of atomic oxygen at 777 nm and 844 nm, the term E/(kT)=2880/T. At temperatures above 6000 K this means that the change in T will result only in very small changes of the intensity ratio.

3.4.8 Determination of Molecular Temperatures

In most cases, the distribution of the number densities of the excited rotational and vibrational levels follows a Boltzmann distribution. If single rotational vibrational lines can be spectrally resolved within the measurements of the molecular bands, the application of a Boltzmann plot is possible to determine the molecular temperatures.

A closer look for the intensity of single emission lines gives the basic principles for temperature determination. Within one electronic transition the ratio of different emission lines is only a function of rotational temperature if the vibrational quantum number does not change.

Therefore, different rotational lines of the same vibrational transition can be used to determine the

rotational temperature. Knowing T_{rot}, emission lines of different vibrational transitions can be used to determine the vibrational temperature if absolute intensities are measured. Determining the electronic temperature is only possible if different electronic transitions of the same molecule can be detected. But even in this case, the assumption of a Boltzmann distribution for the electronic states is necessary. Contrary to the rotational and vibrational states, this assumption is seldom fulfilled and has to be verified in any case. If only emission lines of one vibrational transition are chosen, the terms which contain the electronic and vibrational quantities can be concluded in a constant *C*. Similar to the procedure in the case of the atomic radiation it can then be written

$$\ln\left(\frac{I_{\upsilon'J'-\upsilon''J''}\lambda^4}{S_J}\right) = \ln(C) - \frac{hc}{kT_{rot}}F'(\upsilon', J') \tag{88}$$

Here, $I_{\upsilon'J'-\upsilon''J''}$ is the intensity of the regarded rotational line at the wavelength λ. The *Hönl-London factor* S_J gives the statistical weights of the different transitions as corresponds to the statistical weights g_n used for the atoms. If the intensities of different rotational lines are measured and plotted over the rotational energy *F'*, in the case of a Boltzmann distribution a straight line is formed where the slope $-1/kT_{rot}$ contains the desired rotational temperature.

In Fig. 53 the application of this method to the emission of a N_2^+-molecular band is shown [54]. The theoretical linear relation can be seen clearly which validates the assumption of a Boltzmann distribution.

If the measurement of spectrally resolved lines is possible only within a limited wavelength region, equation (XX), which no longer has the formal qualities of a straight line equation, has to be used directly for evaluation. It is no longer possible to use a Boltzmann plot to determine the rotational temperature. The vibrational temperature now has to be determined using the ratios of the intensities of different emission lines. In the logarithmic form, these ratios appear as differences. Still, the constant C which now includes only the partition functions and the terms due to the electronic transition is eliminated from the equation. Solving for T_{vib} yields for two different emission lines:

$$T_{vib} = -\frac{G'(\upsilon_1') - G'(\upsilon_2')}{\frac{F'(\upsilon_1', J_1') - F'(\upsilon_2', J_2')}{T_{rot}} + \frac{k}{hc}\ln\left(\frac{I_{\upsilon'J'-\upsilon''J'',1}\lambda_1^4 S_{J,2}}{I_{\upsilon'J'-\upsilon''J'',2}\lambda_2^4 S_{J,1}}\right)} \tag{89}$$

Besides the Boltzmann plot, a low resolution temperature determination can also be done by comparing a simulation of the molecular bands with measured data. For this purpose, a simulation of the quantum mechanical processes has to be done. The spectra for different temperature couples (here T_{rot} and T_{vib}) are

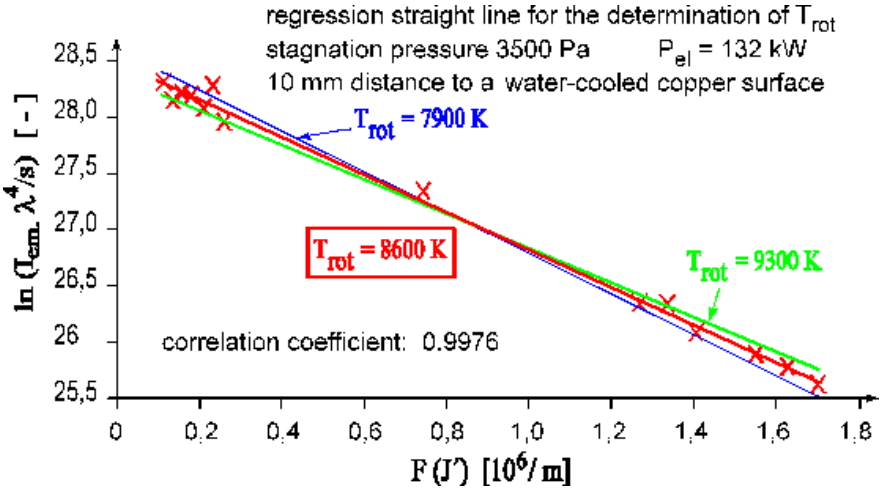

Figure 54: Typical Boltzmann plot used for determining T_{rot} [54].

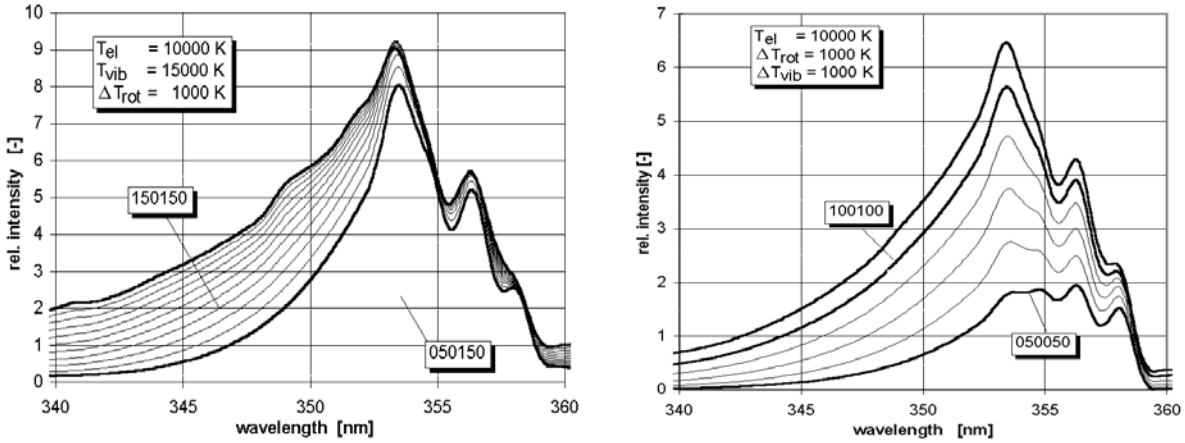

Figure 55: Influence of the different temperatures on the molecular band structure: left - variation of T_{rot}, T_{el} and T_{vib} kept const. right - variation of T_{rot} and T_{vib}, T_{el} kept const..

computed and the numerically determined data are compared with the measurement. The spectrum which shows the highest resemblance to the measured spectrum gives the desired temperatures. One important presumption is that each simulated spectrum can be accurately related mathematically to a certain couple of the parameters of the model (in this case T_{rot} and T_{vib}). Fig. 54 shows a parameter variation for the selected molecular bands. The left diagram shows a variation of rotational temperature while electronic and vibrational temperatures were kept constant. The right diagram shows a variation of both T_{rot} and T_{vib}.

The big advantage of this method compared to the Boltzmann plot is the much lower measurement time needed and the possibility for the simultaneous measurement of both T_{rot} and T_{vib}.

Applying this method using PARADE, the rotational and vibrational temperatures have been determined from the combined emission of the N_2^+ First Negative system and the N_2 Second Positive system. The temperatures presented are obtained from experiments at a plasma state with a mass flow rate of 2 g/s air and an ambient pressure of 290 Pa in front of a SiC sample at T=1280°C and in comparison to a water-cooled copper sample. Figs. 55 and 56 show the spatially resolved distributions of rotational temperature. The strongly rising temperatures in front of the probe surface result from non-equilibrium effects such as deviations from the assumed Boltzmann distributions or disturbances of the emitted spectra by molecules other than N_2^+ or N_2 which are not included in the simulation. For this reason, the temperature values close to the surface are no longer reliable but clearly show the non-equilibrium effects and thus the shape of the boundary layer. The same distributions for the vibrational temperature are also given in Figs. 55 and 56 (mid). Here, the effects of the different materials on the temperatures are even stronger. Figs. 55 and 56 show the correlation factors obtained from the measured data in front of the different surfaces. Again, the non-equilibrium effects in front of the copper surface are much stronger than in front of the SiC surface.

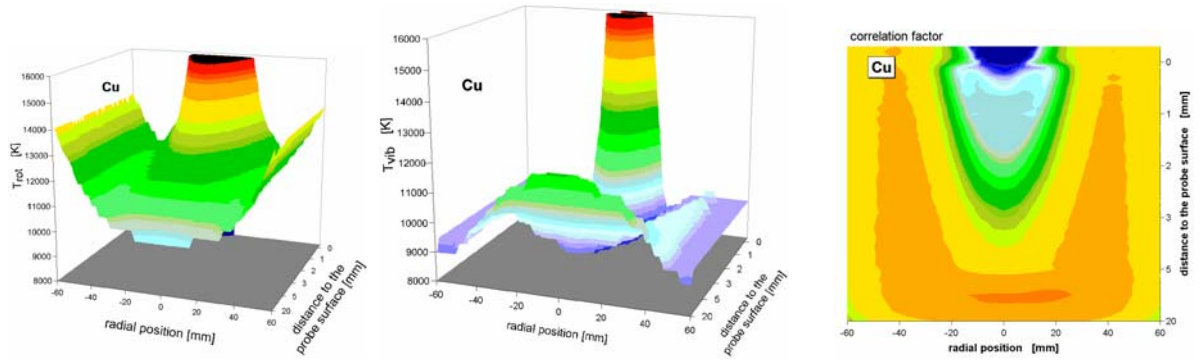

Figure 56: Rotational (left), vibrational (mid) temperature distribution in front of a water-cooled copper surface, and related correlation factors (right).

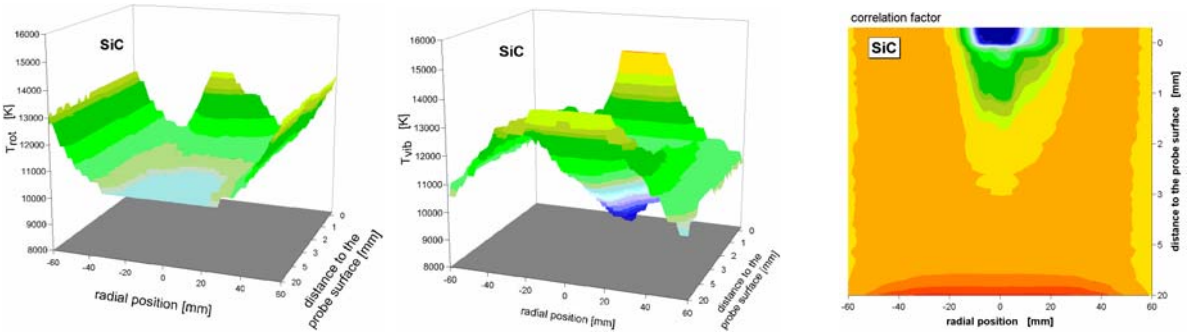

Figure 57: Rotational (left), vibrational (mid) temperature distribution in front on a SiC sample at 1280°C, and related correlation factors (right).

The boundary layer is thicker and the gradients are stronger in the case of a copper surface. As clearly seen in the temperature distributions, the effects of surface catalycity on the boundary layer shape can easily be accessed by the temperature measurements. Thus, the correlation coefficient which expresses the degree of resemblance between the measured data and the computed spectra is a well-suited indicator for the boundary layer shape.

3.4.9 Detection of Erosion Products

Strong radiation of erosion products has been detected in front of an SiC sample at 1700°C at a plasma state with a mass flow rate of 8 g/s and a stagnation pressure of 800 Pa at a distance of 368 mm to the exit plane of the plasma source.

Fig. 57 shows the measured line of sight emission of the silica emission line at 243.52 nm in the measured volume [54]. The influence of the erosion products can be detected up to a distance of roughly 8 mm to the probe.

3.4.10 Determination of Particle Densities

Generally, the determination of particle densities from the measured emission spectra is also possible. Again, the most important assumption is the Boltzmann distribution. Additionally, the corresponding

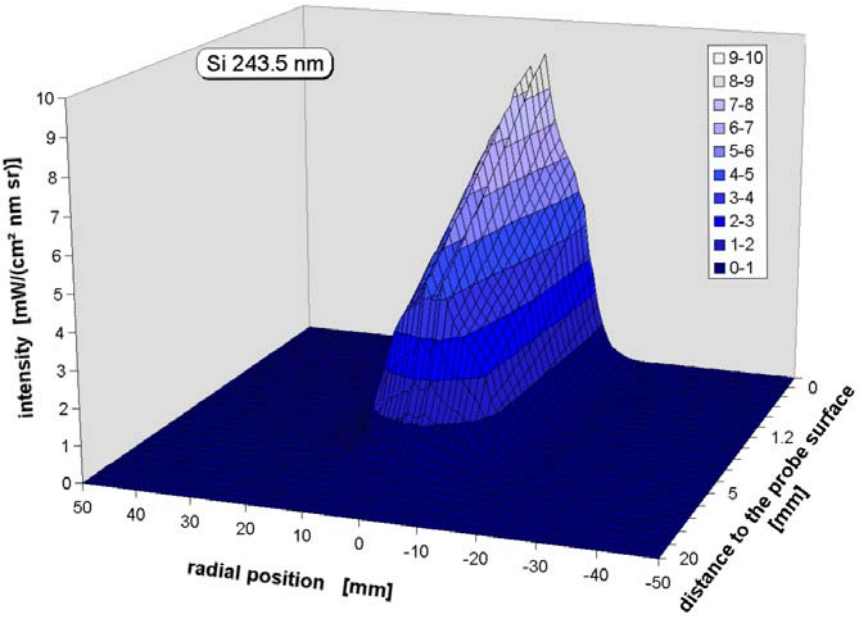

Figure 58: Si emission line intensity at 243.52 nm in the measured volume.

temperature must be accurately known and the measured data have to be calibrated to absolute intensities.

To determine atomic particle densities, the emission coefficient ε_{nm} in equation (51) has to be replaced by the intensity calibrated measured emission I_{nm} and the equation has to be solved for the particle density n:

$$n = I_{nm} \frac{4\pi e^{\frac{E_n}{kT}}}{h\nu_{nm} A_{nm}} \frac{g_0}{g_n} \tag{90}$$

Theoretically, the determination of molecular particle densities from the emission spectrum is also possible. The desired particle density is contained in the constant K in equation (38). Although the assumption of Boltzmann distributed rotational and vibrational energies is often valid, an application to the electronic levels is not necessarily possible. Therefore, the determination of molecular particle densities with other methods such as laser induced fluorescence is better suited.

3.5 Fabry Perot Interferometry

A Fabry Perot interferometer is a high resolution spectral device based on the principle of multiray interference. It can be used to measure particle speeds and translational temperatures. Axial and any azimuthal speed components of the accelerated plasma particles that appear are measured by means of the Doppler shift of their emission lines. The Doppler shift can be directly determined by simultaneously displaying the plasma line with a reference line which has not been shifted. In low pressure plasma flow, only mean velocities can be measured due to the low intensity of the spectral lines and hence rather long integration times. To determine the line shift, a high resolution spectrum is necessary. This spectrum can best be achieved by means of a so-called Fabry Perot Interferometer (FPI). Futhermore, heavy particle translational temperature can be determined from the Doppler broadening of the observed spectral line.

3.5.1 Theoretical Principles of Fabry-Perot Interferometry

The Fabry-Perot interferometer was introduced by two French opticians, Charles FABRY and Alfred

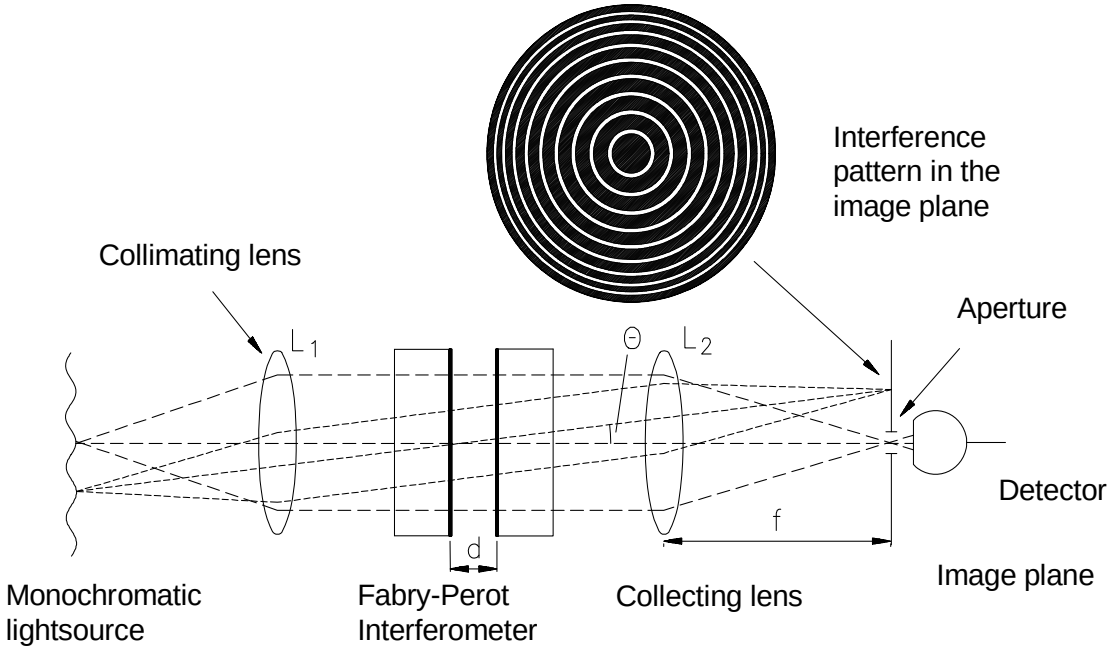

Figure 59: Schematic construction of a Fabry-Perot interferometer.

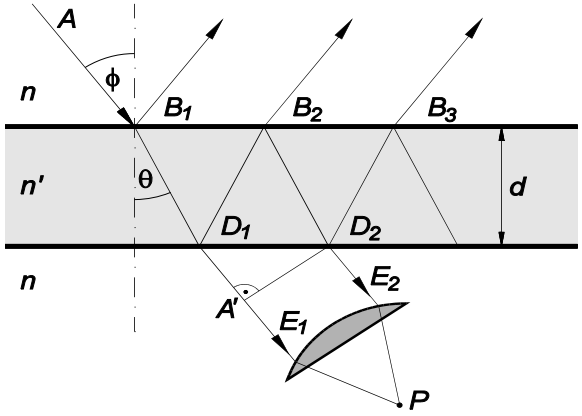

Figure 60: Reflection in a glass plate.

PEROT, in 1897. It essentially consists of two glass plates with a reflective coating on one side of each plate. The plates are positioned parallel to each other and are a few micrometers to a few meters apart.

The function of an FPI is based on the interference of a smooth wave through multiple reflections on two mirror plates. This phenomenon can also be explained by the multiple reflections in a plane parallel plate. The two possibilities to differentiate are *constructive* and *destructive* interference. Constructive interference appears when the phase shift of two overlapping, smooth waves is an integer multiple of 2π (see Fig. 58). Otherwise a destructive interference reduces the transmission light intensity.

In the case of a Fabry-Perot interferometer the multiple reflection takes place on the translucent inner surfaces of two parallel glass plates. As Fig. 59 shows, an aperature partition on the optical axis in the focal point of lens 2 has the effect that only almost parallel light ($\theta \approx 0°$) makes it through the FPI. If the medium has the refractive index n between the plates, the following condition for the intensity maximum of order m results:

$$m\lambda_{0=2nd} \tag{91}$$

The Fabry-Perot interferometer can be adjusted to a declared wavelength by varying the parameters n or d. Changing the refractive index of the medium between the plates, for example by changing the pressure, is difficult. Modern FPIs are, therefore, adjusted by changing the distance between the plates, e.g. one of the plates is shifted by means of piezoelectric. The piezoelectric elements are steered through a ramp generator and in this way they create a linear, periodic translational movement. This kind of scanning makes it possible to represent several interference arrangements of a certain wavelength or rather makes it possible for a defined, narrow wavelength area to go through.

3.5.2 The Airy Function

The intensity I_T of the waves penetrating the FPI is among other things dependent on the transmission T of an FPI. The intensity is defined as the percentage permeability in the exact resonance distance of the mirror plates for a certain wavelength λ_0, that means as a quotient of the intensities with and without FPI in the path of the detecting optics. The reduction of intensity caused by the FPI is essentially determined by the absorption and the scattering losses on the layers of the mirror-coating, expressed by the mirror depending constant A_S and the reflection degree R on the mirror layers. In order to describe the relationship of the transmitting to incoming intensity I^T/I^i, the so-called Airy function is used which is given by:

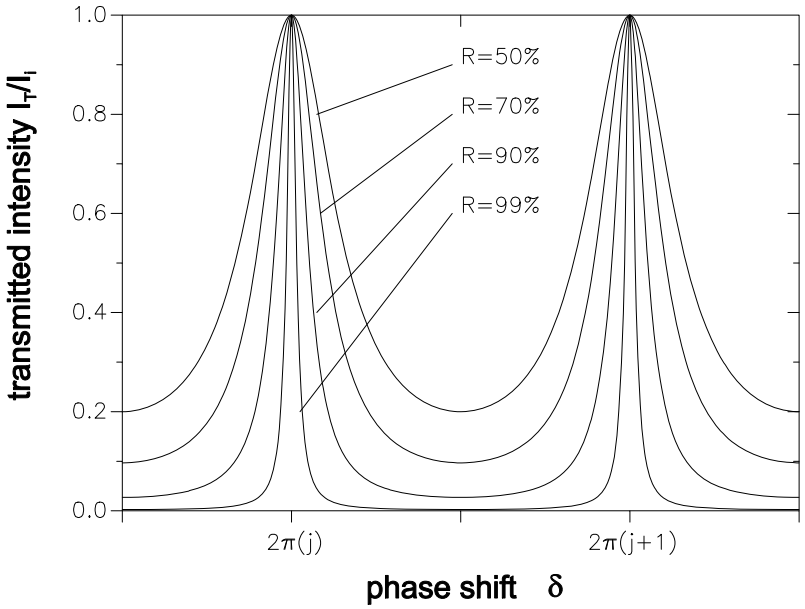

Figure 61: Intensity relationship I_T/I_i for various degrees of reflection as a function of □.

$$\frac{I^T}{I^i} = \frac{(1-R)^2}{(1-R)^2 + 4R\sin^2\frac{\delta}{2}} \quad . \tag{92}$$

Here δ is the phase shift of an electromagnetic wave, caused by the reflections on the mirrors' surfaces. If δ is a multiple of 2π, then constructive interference occurs. In this case

$$\delta = \frac{4\pi}{\lambda_0} nd\cos\theta = 2\pi \cdot m \tag{93}$$

is valid, with n as the refractive index inside the FPI, d as the spacing between the mirror plates, θ as the angle of the incoming wave, λ_0 as the wavelength of the transmitted light and m as the number of the interference order. The Airy function is shown for two orders *m* in Fig. 60 for various degrees of reflectivity of the mirrors.

For a given optical thickness *(nd)* the Airy function describes a whole system of concentric interference rings when the order *m* of the interferences is equivalent to a whole number (*m* = 1, 2,...). For small degrees of reflection *R* wide interference rings result and the contours become more and more defined as the degree of reflection increases.

A measure for the definition of the interference rings is given by the so-called half-width χ, which means the width of the profile at half the height of the intensity maximum. For an interference ring of the order m the intensity is reduced by half. Hence it follows that the half-width of the interference ring results in:

$$\chi = \frac{4}{\sqrt{\frac{4R}{(1-R)^2}}} \tag{94}$$

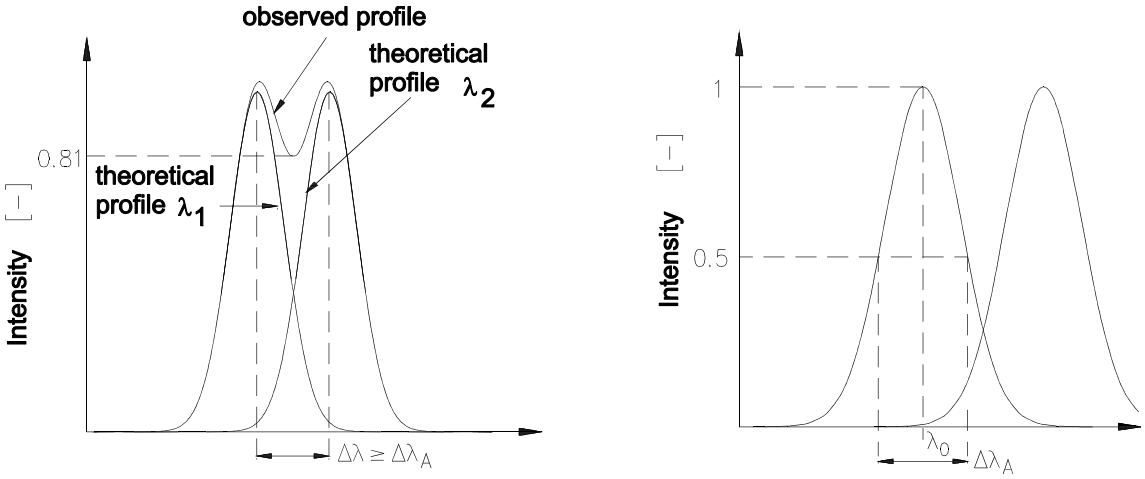

Figure 62: Separation of spectral lines.

3.5.3 Characteristic Quantities of a Fabry-Perot Interferometer

For the two applications, i.e. velocity measurements and translational temperature measurements, the FPI can be optimized with respect to the needed wavelength and wavelength shift resolution. The resolution of the wavelength shift of the FPI means the ability to separate two spectral lines which are very close together. The resolution is of great importance diagnostic application. For the practical use of the FPI for the purposes of detecting and identifying spectral lines, the Rayleigh criteria can be used. This is shown in Fig. 60. Two spectral lines must be clearly separated by means of a drop in intensity to at least 81% of the corresponding line profile maximum. To use the FPI to determine the Doppler shift and broadening an exact determination of the central wavelength λ_0 related to the maximum intensity is indispensable.

According to Fig. 61, the resolution $\Delta\lambda_A$ of the FPI is defined as the half-width of a perfectly monochromatic spectral line of the wavelength λ_0. The useful resolution $\Delta\lambda_A$ depends on two characteristic quantities of a Fabry-Perot interferometer: the usable finesse F_N and the free spectral range $\Delta\lambda_F$. $\Delta\lambda_A$ is calculated from the quotient of both according to:

$$\Delta\lambda_A = \frac{\Delta\lambda_F}{F_N} = \frac{\lambda_0^2}{2ndF_N} \quad . \tag{95}$$

3.5.4 The Finesse F_N

The quality of an FPI is described by the so-called instrumental finesse F of the interferometer. The finesse is used to measure the performance of the FPI and describes the ability to resolve the spectral lines which are very close together. The larger the finesse of an FPI, the higher the resolution. The instrumental finesse F is determined by the individual finesses of the degrees of reflection F_R and the finesse F_F of the smoothness of the mirror plates. If an FPI is operated as a spectral device, in addition to the instrumental finesse the characteristics of the collecting optics which follow the FPI must be taken into consideration. The useful finesse F_N contains in addition the finesse of the aperture partition F_P and the refraction finesse F_D. This can be calculated as follows:

$$\frac{1}{F_N^2} = \frac{1}{F^2} + \frac{1}{F_P^2} + \frac{1}{F_D^2} = \frac{1}{F_R^2} + \frac{1}{F_F^2} + \frac{1}{F_P^2} + \frac{1}{F_D^2} \quad . \tag{96}$$

As a result, the collecting optics following the FPI should be subjected to an optimization to keep the useful finesse F_N as close as possible to the value of the instrumental finesse F.

3.5.5 The Free Spectral Range

During movement of the FPI mirror plates, that is when the distance d between them is varied, the various orders of interference of the wavelength under observation move across the detection apparatus, for example across the aperture partition in front of the detector in Fig B4.2. The free spectral range $\Delta\lambda_F$ of the FPI describes the wavelength interval in which light is represented under the same order. It is given by

$$\Delta\lambda_F = \frac{\lambda_0^2}{2nd} \tag{97}$$

The free spectral range of the FPI can therefore be influenced by the variation of the distance between the mirror plates d. For a very small free spectral range, the mirror plates have to be far apart. But on the other hand, the useful total finesse F_N decreases with increasing distance [4]. The resolution finally approaches a minimum asymmetrically. It is already close to this value in the case of nitrogen (N_1) at a distance of approximately 3mm [4]. The free spectral range can be determined experimentally by measuring two orders of a monochromatic spectral line, for example of a laser with a precisely known wavelength and small bandwith.

3.5.6 Doppler Shift and Heavy Particle Speed

The Doppler effect was discovered by Christian Doppler in 1843 while investigating the propagation of sound waves. The principle effect occurs also with emission lines, to be resolved, however, only at very high speeds. If a light emitting medium is moving with a speed v and the emitted light is observed by a stationary receiver under an angle α to the propagating medium, the following equation is valid between the wavelength λ measured by the receiver and the actual emitted wavelength λ_0:

$$\frac{\lambda}{\lambda_0} = \frac{\sqrt{1-\frac{v^2}{c^2}}}{1-\frac{v}{c}\cos\alpha} \quad . \tag{98}$$

Here c represents the speed of light and α is the angle between the normal to the wave vector of the spreading light and the speed v of the emitting particle. For plasma wind tunnel applications α indicates the angle between the optical axis of the FPI and the flow vector of the plasma stream. Because v is generally very small compared to c, the root in the equation above is ~1. If the denominator in the equation above is developed in a binomic row, while neglecting the term to the second and higher orders the result is finally the following equation for the Doppler shift $\Delta\lambda_D$:

$$\Delta\lambda_D = \lambda - \lambda_0 = \lambda_0 \frac{v}{c}\cos\alpha \quad . \tag{99}$$

From this equation the plasma velocity v can be determined from the Doppler shift measurement. The chosen angle, however, must be large enough so that $\Delta\lambda_D$ is larger than the resolution $\Delta\lambda_A$ of the FPI. For the application in rarefied supersonic plasma flows, 45° have turned out to be a good trade off between available space and needed resolution.

3.5.7 Doppler Broadening and Heavy Particle Translational Temperature

While observing a plasma volume emitting radiation from any angle, a Doppler broadening of the spectral line being observed occurs due to the random thermal movement (v_{th}) of the plasma particles. This Doppler broadening $\Delta\lambda_T$ results from the overlapping of Doppler shifts $\Delta\lambda$ for which the following is valid:

$$\Delta\lambda = \pm\lambda_0 \frac{v_{th}}{c} \quad . \tag{100}$$

Contrary to the speed v in eq. (98), v_{th} is not a directed speed and the change in the wavelength is therefore also not dependent on the angle. Because, however, the thermal speed is a function of the translational temperature T_{tr} of the corresponding particle, the temperature T_{tr} can be determined by determining $\Delta\lambda_T$.

A purely thermal movement of the emitting particle corresponds to the distribution of the thermal speeds of a Maxwell distribution. The particle concentration dn with a thermal speed in the interval between *v* and *v* + *dv* is given by:

$$\frac{dn}{n} = \sqrt{\frac{m}{2\pi kT_{tr}}} \exp\left(-\frac{mv^2}{2kT_{tr}}\right) dv \quad . \tag{101}$$

Here *k* is the Boltmann constant, *n* is the concentration of the emitting particles and *m* their mean mass. If *v* is replaced by *dv* and its derivative result is:

$$\frac{dn}{n} = \sqrt{\frac{mc^2}{2\pi kT_{tr}\lambda_0^2}} \exp\left(-\frac{mc^2}{2kT_{tr}}\left(\frac{\Delta\lambda}{\lambda_0}\right)^2\right) d(\Delta\lambda) \quad . \tag{102}$$

In a so-called optically thin plasma the radiation absorption plays only a minor role and the intensities of the spectral lines being observed are proportional to the concentration of the emitting particles. In a low pressure plasma flow, an optically thin plasma can be assumed. The result for the intensity of a Doppler broadened spectral line is a distribution according to:

$$I(\Delta\lambda) = I_0 \sqrt{\frac{mc^2}{2\pi kT_{tr}\lambda_0^2}} \exp\left(-\frac{mc^2}{2kT_{tr}}\left(\frac{\Delta\lambda}{\lambda_0}\right)^2\right) \quad . \tag{103}$$

Here I_0 is the entire intensity of the spectral line and herewith $I(\Delta\lambda)$ the intensity at a distance of $\Delta\lambda$ to the unshifted center λ_0. According to the equation above this is the case when the exponential term assumes the value 1/2. Therefore

$$\Delta\lambda = \sqrt{\frac{2kT_{tr}\ln 2}{mc^2}}\lambda_0 \tag{104}$$

is valid. Because the distribution of the spectral line is symmetric under these assumptions, the entire Doppler broadening results in $\Delta\lambda_T = 2\Delta\lambda$, and herewith for the translational temperature of the emitting particles,

$$T_{tr} = \frac{mc^2\Delta\lambda_T^2}{8k\lambda_0^2 \cdot \ln 2} \tag{105}$$

is attained.

3.5.8 Experimental Set-up

One of the advanced experimental setups in use is shown in Fig. 62. It provides easy access to the light emitted by the plasma plume without intensive calibration of the optical path to the FPI. Two fiber optics can be mounted on the positioning system in the plasma wind tunnel. The optical axes of both optics are orientated under a fixed angle of α=45°. The focus of both optics is exactly at the same position in the

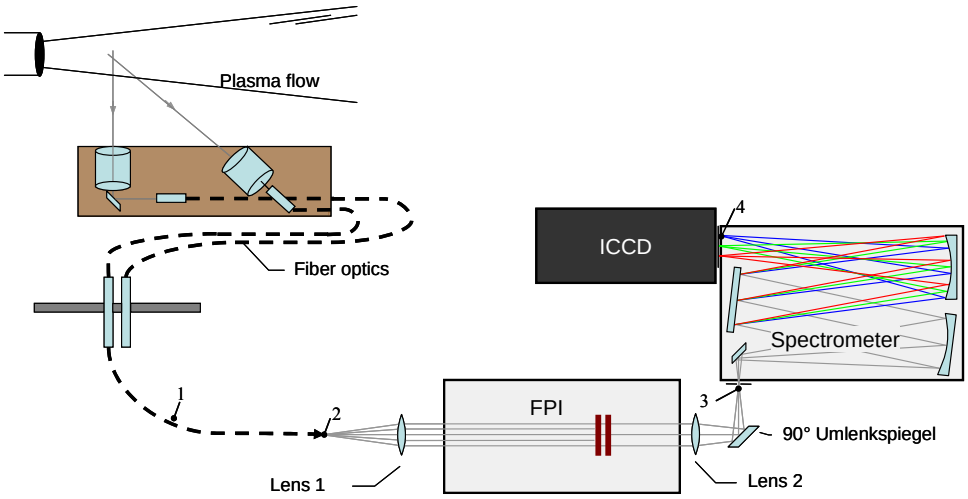

Figure 63: Experimental set-up of the Fabry-Perot interferometer.

plasma beam and can be moved to every position. Since one of the optics will always be mounted perpendicular to the plasma beam axis, the observation angle α is always 45°. A third fiber optic provides the possibility to feed laser light into the FPI for calibration purposes. Each of the three fiber optics can be plugged into an optical system which parallelizes and widens the light beam coming out of a fiber optic.

Using a fast intensified CCD Camera, the measurement of different spectral lines with one FPI application can be realized. The spectral distinction occurs in the spectrometer and the fast camera records along the FPI-axis [56].

3.5.9 Exemplary Results

To examine the Doppler effects, one has to choose an adequate spectral line emitted by the plasma. The line of interest has to be strong enough and in order to achieve high resolution, longer wavelengths are preferred. One of the strongest emission lines rises out of the transition of atomic nitrogen at λ_0=746.83 nm.

In Fig. 63, two orders of a typical shifted N_I emission line are shown. The distance between the two line maximas represents the free spectral range $\Delta\lambda_F$ =0.092 nm. There is a very small shift between the blue and the red line which is due to the view angle and leads to the measurement of the velocity. From the line broadening the temperature can be resolved.

The axial distribution of the atomic nitrogen velocity in two air plasma flows of different conditions along the plasma plume centre line axis can be seen in Fig. 64. The values are taken without Abel inversion. Due to the relatively flat velocity profile in the zone of high emission in this case, an Abel inversion does not change the result remarkably. The velocity distribution shows a “shock” behaviour with decreasing velocity in the compression zone and acceleration in the expansion area for one of the test conditions.

The resulting temperatures in a radial scan for different plasma condition are pictured in Fig. 64 again taken without an Abel inversion.

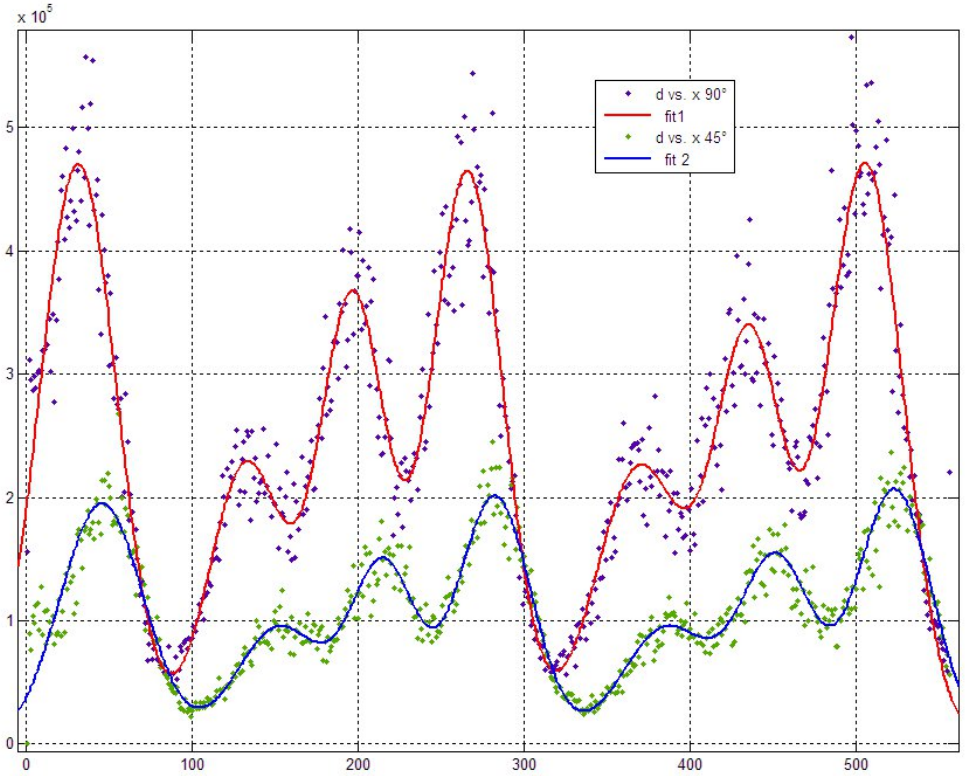

Figure 64: Doppler shifted NI emission line of an air plasma flow [57].

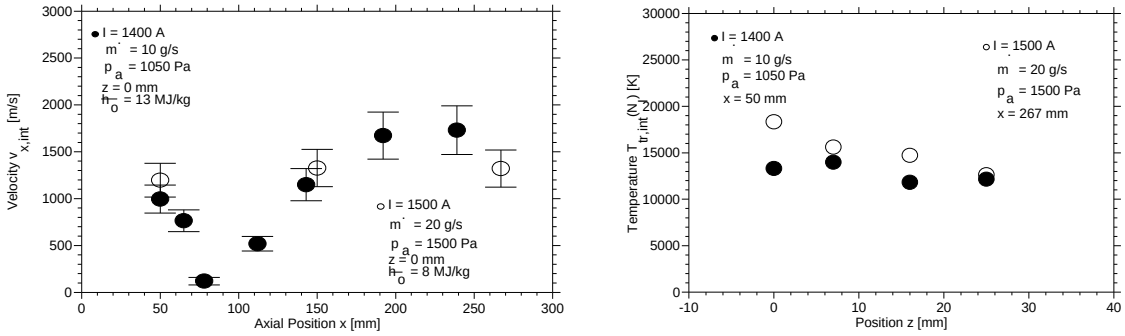

Figure 65: Axial distribution of the heavy particle velocity in air plasma flows of different conditions along the plasma plume center line axis (left) and radial temperature distribution (right).

3.6 Absorption Spectroscopy

This method is based on the same quantum mechanical processes as emission spectroscopy, only that energy is absorbed and not emitted by the plasma. Accordingly, light is absorbed at discrete lines if the radiation of a continuous light source is transmitted through a gas. These absorption lines correspond to the discrete energy levels necessary for the excitation of atoms and molecules in the gas [59]. The continuous spectrum of the calibration lamp observed through the absorbing medium (e.g. the gas or plasma) therefore shows weaker intensities at these discrete lines. If the medium is regarded rectangular to the optical axis where the continuous radiation is not visible, an emission line at the same wavelength as the absorption line is visible due to the short life time of the excited state.

3.6.1 The Coefficient of Absorption

The total amount of energy absorbed per time and volume unit can be written as:

$$e_{abs} = B_{mn} n_m I_\nu h\nu \tag{106}$$

with:

n_m	number of particles in the absorbing state per volume unit
$h\nu$	radiation energy
I_ν	spectral energy density

The factor B_{mn} is the Einstein transition probability for absorption for the transition m → n and describes the number of absorbing particles per time unit and per spectral energy density in [$m^3J^{-1}s^{-2}$]. The product $B_{mn}\, I_\nu$ is an expression for the portion of particles in the state m which absorb one photon with the energy h ν per time unit.

The total amount of energy absorbed per time and volume unit can also be expressed by the product of the number of absorbed photons and their energy:

$$e_{abs} = \kappa_{mn} n_m c I_\nu \tag{107}$$

where κ_{mn} is the coefficient of absorption. Combining both equations yields:

$$\kappa_{mn} = \frac{h\nu}{c} B_{mn} \tag{108}$$

The coefficient of absorption has the unit [m^2s] and is a measure for the amount of radiation of the frequency ν that can be absorbed by one particle.

In reality, similar to the emission lines each absorption line has a certain line width which is produced by various effects (see section B2.1.2). Basically, the expression for coefficient of absorption represents an integration over this line width and can be written as:

$$\kappa_{mn} = \int \kappa'_{mn}(\nu) d\nu \tag{109}$$

3.6.2 Diode Laser Absorption Spectroscopy

Atoms are capable of absorbing radiation in only a very narrow frequency interval. For this reason, the radiation source has to meet some special requirements. Nowadays, diode lasers are useful radiation sources. Fig. 65 shows an experimental set-up for these kinds of measurements. The plasma absorbs part of the incoming radiation at the resonant line. This part is directly proportional to the amount of particles in the corresponding state of excitation. Spectral lines that do not exist in absorption are transmitted without any reductions. Particularly in highly excited plasma flows Diode Laser Absorption Spectroscopy (DLAS) is useful. Here, diode lasers are cheap available sources for the diagnostics of excited levels. After the spectral decomposition in the monochromator, the absorption line is separated and all other emission lines are eliminated. The detector „sees" only one line. The comparison with the originally emitted line gives the absorption.

To determine n_m , the radiant energy fluxes have to be regarded. According to Lambert's law the relation:

$$\phi_{D_\nu} = \phi_{0_\theta} e^{-\kappa_{mn} n_m d} \tag{110}$$

is given, where $\phi_{D\nu}$ and $\phi_{0\nu}$ represent the spectral radiative flux prior to and after the transmission through the absorbing region of the thickness d. If d is known and κ_{mn} can be determined for the specified absorption line, the particle density in the state m (usually the ground state) is obtained from:

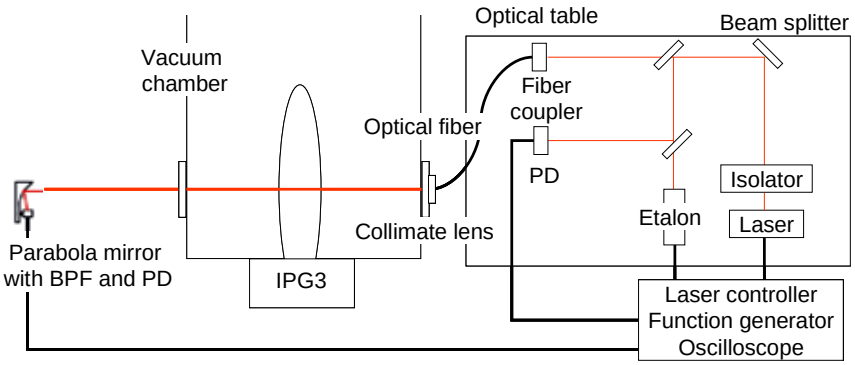

Figure 66: Experimental setup for diode laser absorption measurements.

$$n_m = \frac{1}{\kappa_{nm} d} \ln \frac{\phi_{0_\nu}}{\phi_{D_\nu}} = \frac{A}{\kappa_{nm} d} \tag{111}$$

The above equation is valid as long as the half width of the emission line of the radiation source is remarkably lower than that of the absorbing line. If not, a part of the emitted radiation at both (spectral) sides of the absorption line cannot be absorbed which influences the results. Furthermore, n_m has to remain constant over d. Otherwise, an Abel-inversion of the measured data has to be performed to obtain local particle densities.

3.6.3 Exemplary Result

A tunable diode laser with external cavity can be applied for atomic oxygen detection. The schematic of LAS system is shown in Fig. 65. The laser linewidth is less than 300 kHz. By setting a modulation frequency the difference between laser light and background can be distinguished. An etalon whose free spectral range is 1 GHz was used as a wave meter. The probe beam is usually passing through an optical fiber to the vacuum chamber wall and the transmitted signal is detected by a photo detector and appropriate band pass filters. Setups using spectrometers are also possible. Signals are usually recorded using digital oscilloscopes with rather high resolution and high sampling rates. For plasma jet applications some restrictions to absorption spectroscopic methods appear. First, in most cases the temperatures are rather high yielding a highly excited plasma. Thus, the particle densities determined by absorption spectroscopy are no longer necessarily coupled to the ground state density [60].

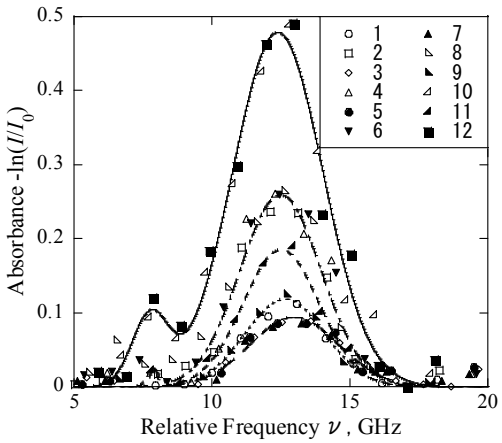

Figure 67: Absorption line profile of an atomic oxygen excited state at λ=844nm.

3.7 Laser-induced Fluorescence Spectroscopy

Laser techniques are in use in plasma wind tunnels for identifying particles, determining particle densities of atoms, molecules and electrons and for plasma velocity measurements. A big part of our knowledge of the structure of atoms or molecules could be gained by laser diagnostic measurement methods. Laser-based techniques offer the capability of performing spatially and temporally resolved. The interaction between the electromagnetic radiation of the laser and particles leads firstly to absorption and/or scattering and in consequence to emission spectra. Laser induced fluorescence measurements is a well-established, sensitive technique for detecting population densities of atoms and molecules in specific quantum states and offers the possibility of investigating species of interest in a selective way. The main advantage compared to the so-far discussed non-intrusive diagnostics is that the ground state densities are accessible and the results are absolute number densities. The main drawback is an immense experimental effort. Among other laserspectroscopic methods, laser-induced fluorescence spectroscopy represents a powerful tool in plasma diagnostics for the sensitive verification of atomic and molecular species in low-temperature plasmas. Here, laser photons are used for state-selective excitation of an atomic or molecular energy level of the respective particle species. Characteristic plasma parameters such as local particle densities, temperatures and velocities can be extracted from the detected observed fluorescence radiation.

With laser induced fluorescence, an upper electronic state is populated by a laser source with an emission frequency tuned to an optically allowed resonance between the electronically and rotationally vibrationally excited state and a discrete lower state, typically the electronic ground level. Fluorescence then denotes the following radiation emitted by molecules or atoms, decaying by spontaneous emission of a photon in an optically allowed transition from a higher to lower energy state. The fluorescence occurs parallel to other processes which act to de-excite the molecule, such as collisional energy transfer to other molecular states.

Fig. 67 shows the excitation and de-excitation processes involved in a laser-induced fluorescence process. After excitation (b_{12}), the laser-populated upper state may undergo a number of subsequent processes. Firstly, the molecule can be returned to its original state by stimulated emission (b_{21}). Secondly, absorption of an additional photon can excite still higher molecular states, including ionized levels. Thirdly, the internal energy of the system can be altered in inelastic collisions with other molecules producing rotational and vibrational and also electronic energy transfer, the latter is often referred to as quenching (Q_{ij}). Fourthly, interactions between the separate atoms of the molecule, known as internal collisions, produce internal energy transfer and dissociation of the molecule. When the dissociation is produced by a change from a stable to a repulsive electronic arrangement in the molecule, it is called predissociation. Finally, there is the fluorescence signal (A_{21}) of the originally populated state and nearby states, indirectly populated through collisions. This signal can be captured with a photodetector and can be related to specific properties of the absorbing species through modelling of these state-to-state transfer processes. The rate equations are conceptually and mathematically more traceable than the quantum approach, but fail to include possible coherence effects. Generally, the validity of the rate equation analysis holds true for laser pulses which rise slowly compared to the characteristic collision time. The time dependent

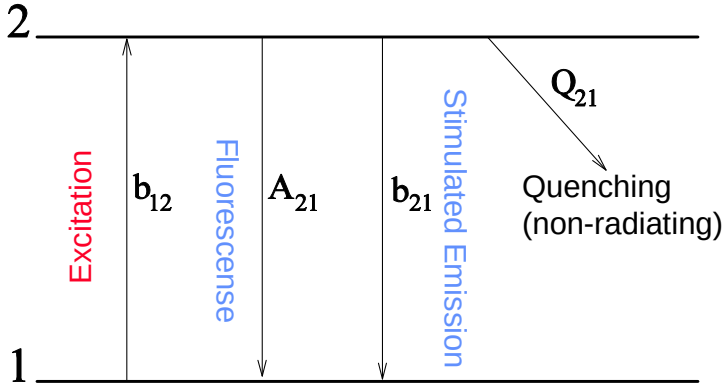

Figure 68: Simplified energy level diagram for a one photon laser-induced fluorescence process.

population N(t) of a specific energy level j among a set of other levels i can be modelled with the set of rate equations, given by:

$$\frac{dN_j(t)}{dt} = \sum_{i \neq j} \left(N_i(t) Z_{ij} \right) - N_j(t) \sum_{i \neq j} Z_{ji} \quad . \tag{112}$$

The first summation represents events which populate j while the second denotes loss processes. The total rate coefficient for all events transfering molecules from level i to j is Z_{ij} (s^{-1}). A number of distinct rate coefficients are included in this overall coefficient: the collision transfer coefficient Q_{ij} (s^{-1}), encompassing both intermolecular and internal collisions, the Einstein coefficient A_{ij} (s^{-1}) for spontaneous emission and the coefficient for laser stimulated processes W_{ij} (s^{-1}). For single photon laser stimulated absorption or emission, $W_{ij}=B_{ij}I_{\nu}$, where B_{ij} ($cm^2J^{-1}Hz$) is the Einstein B coefficient and I_ν is the laser spectral intensity. Applying equation (B5.1) for the energy levels involved gives a system of differential equations. The equations depend on the excitation and detection scheme used for a specific molecule or atom and have to be solved taking into consideration the special properties of the quantum mechanical behaviour of the particle. For a simple two level model, where only the ground (index 1) and the directly excited state (index 2) are taken into account, the system of differential equations becomes:

$$\frac{dN_1}{dt} = -N_1 b_{12} + N_2 (b_{21} + A_{21} + Q_{21}) , \tag{113}$$

$$\frac{dN_2}{dt} = N_1 b_{12} - N_2 (b_{21} + A_{21} + Q_{21}) \tag{114}$$

Here, predissociation and photoionization have been neglected and the population of the excited state prior to the laser excitation is negligible as well. The total population in the system is constant and for moderate temperatures in good approximation equal to the initial population of the ground state N_1^0 prior to laser excitation. This population can be calculated with the Boltzmann expression. The lower index of N_1^0 accounts for the state and the upper index indicates t=0, i.e. prior to the laser pulse, such that:

$$N_1 + N_2 = \text{constant} = \mathrm{N}_1^0 \quad . \tag{115}$$

The time dependent population for the excited state can then be written as:

$$N_2(t) = \frac{W_{12} N_1^0}{r} (1 - e^{-rt}) \quad , \tag{116}$$

where

$$r = W_{12} + W_{21} + A_{21} + Q_{21} . \tag{117}$$

For steady state assumption, i.e. the rates of the exciting and decaying processes reach a steady state behavior, the population in the excited state is then given by:

$$N_2 = N_1^0 \frac{B_{12}}{B_{12} + B_{21}} \frac{1}{1 + \frac{I_{sat}^{\nu}}{I_\nu}} \quad , \tag{118}$$

where the saturation spectral irradiance I^{ν}_{sat}, i.e. the laser irradiance which saturates a transition, is defined as:

$$I_{sat}^{\nu} = \frac{(A_{21} + Q_{21}) c}{B_{12} + B_{21}} \quad , \tag{119}$$

with c as the speed of light. In the saturation regime the maximum number of molecules or atoms are in the excited state. Increasing the laser irradiance will not increase the fluorescence signal any more. At low

laser excitation irradiances, i.e. $I_v << I^v_{sat}$, the fluorescence is said to be in the linear regime, namely linearly proportional to the input laser irradiance. For $I_v >> I^v_{sat}$, the saturated regime is reached, where the fluorescence signal becomes independent of quenching processes and the laser irradiance. In the saturation regime, the rates of laser absorption and stimulated emission become so large that they dominate the state-to-state energy transfer into and out of the directly pumped levels. Saturation also maximizes the fluorescence signal. However, complete saturation is not easy to achieve, especially in the wings of the laser focus and during the entire duration of the laser pulse.

In the linear regime, the fluorescence signal depends on the laser irradiance. Additionally the quenching rate can be determined experimentally in the linear regime. In low pressure regimes and low laser irradiances, the quenching rate can be measured by monitoring the exponential decay rate, i.e. the time resolved decay of the excited molecules to the ground level. An excited level has a certain molecular dependent lifetime, which is described with: $\tau=1/(A+Q)$. Here, Q stands for all de-excitation processes and A again for the spontaneous emission rate. By monitoring the time decay, one can extract the de-excitation rate, as seen in Fig. 68.

In general, the fluorescence wavelength is different from that of the incident excitation and occurs primarily, but not exclusively, at longer wavelengths. The photons emitted from the excited molecules radiate undirected. Therefore, the fluorescence signal can be detected under any angle, but it is advantageous to detect the fluorescence perpendicular to the propagation of the laser beam and perpendicular to the plasma flow under investigation because this provides the smallest observation volume and a non-Doppler shifted absorption line.

There are two ways of setting up the experimental approach. In a single point measurement, the laser is focused into the observation area and the fluorescence is detected with a one-dimensional detector, generally a photomultiplier tube (PMT). The selection of the fluorescence wavelength can be achieved either with a monochromator or with an interference filter. The output signal of the PMT is then captured with a so-called gated integrator and boxcar averager. This device is designed to recover fast analog signals from noisy backgrounds. It consists of a gate generator, a fast gated integrator and exponential averaging circuitry. The gate generator provides an adjustable delay from a few nanoseconds to 100 milliseconds to an input trigger pulse before it generates a continuously adjustable gate of 2 ns to 15 µs. The fast gated integrator integrates the input signal during the gate. Fig. 69 shows an example of setting the sampling gate of the boxcar averager (data acquisition device) in respect to the fluorescence signal. For

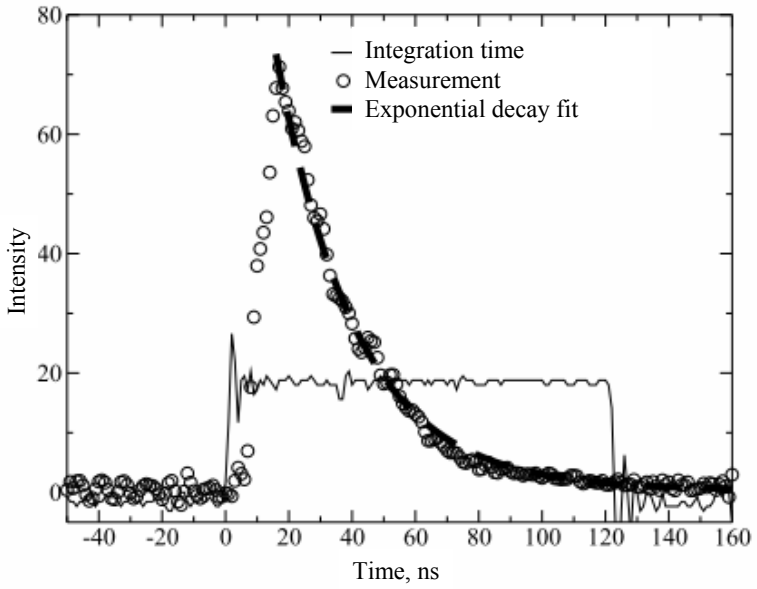

Figure 69: Lifetime measurement of NO [62].

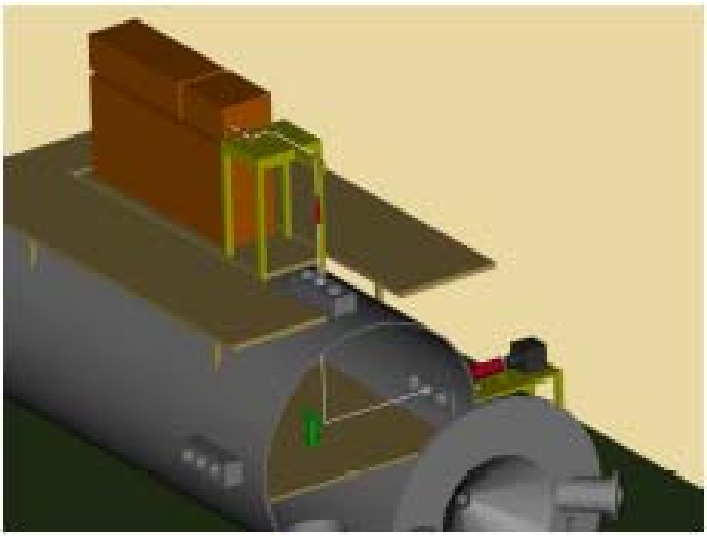

Figure 70: Experimental setup for LIF measurements.

a planar LIF (PLIF) measurement, the excitation laser beam is optically spread into a thin sheet, and the resulting fluorescence from the illuminated plane is imaged through an appropriate filter onto a two-dimensional detector.

For many species of interest, such as H, O, N, Kr, and Xe, particle densities can only be calculated from fluorescence intensities if laser excitation is induced from the atomic ground state. However, to overcome the energy gap between the ground state and the lowest energetic excited states, laser photons far below 200 nm are required. To circumvent the various problems of generation of laser radiation at such low wavelengths, the energy for the excitation of an excited level is obtained by simultaneous absorption of two laser photons. In Fig. 70, several excitation schemes including appropriate fluorescence transitions are shown for some atomic species.

In applications with respect to research fields in spaceflight engineering, atomic species of O, N, and Xe are of particular interest. At present, Xe is used as a promising fuel in ion thrusters. Fig. 71 displays a series of measurements in the plume of a RIT-10 ion thruster. In a spectral scan, the laser wavelength is tuned over the spectral range of the (two-photon) absorption line, which is defined by broadening mechanisms such as the laser bandwith and the Doppler broadening of the laser induced transition. In the absence of saturation effects, the fluorescence intensity is a measure for the particle density. Two-photon

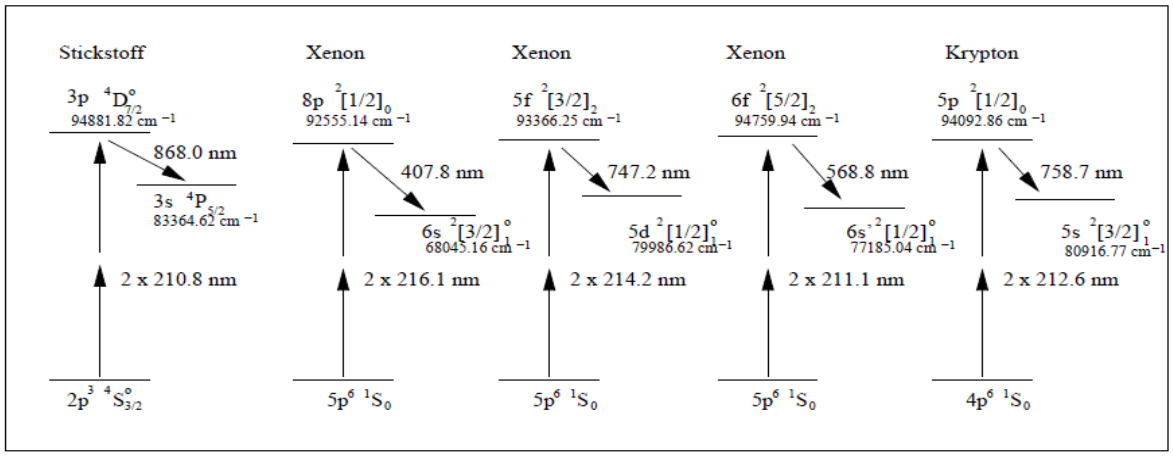

Figure 71: Fig. 1: Two-photon transition schemes in N, Xe and Kr. Initial levels denote the ground state of the respective atom.

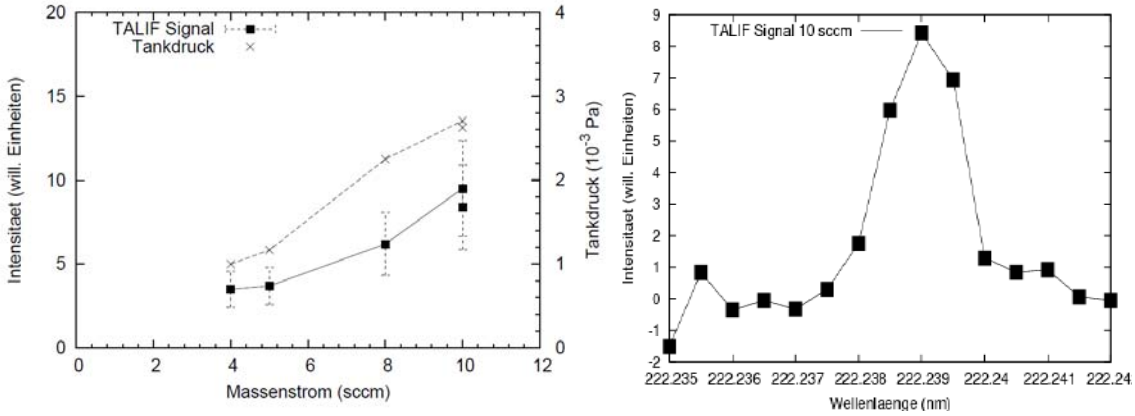

Figure 72: *Left:* Absorption line of the excitation of the 6p' $[1/2]_0$ level in the plume (here: cold gas flow) of a RIT-10 ion thruster.
***Right*: Fluorescence intensity (as a measure of the particle density) versus mass flow (squares) on the symmetry axes at a distance of ~10 cm of the thruster exit plane. [61].**

spectroscopic experiments in xenon plasma concentrate on neutral particles since singly ionized xenon requires, due to the distribution of the energy levels, laser photons below 200 nm even when two-photon transitions are used, which necessitates significantly more complex experimental setups.

For the experimental simulation of atmospheric re-entry conditions in plasma wind tunnels, there is a need of generators to produce O-, N-, and air plasma flows of high enthalpy. Flow characterization in the free stream as well as near the surface of appropriate heat shield materials can be carried out by two-photon laser spectroscopy in O and N.

In addition, there are several advantages if an in-situ calibration of a two-photon experiment is performed using another two-photon measurement of a reference species in an environment of a defined particle density, provided that relevant atomic transitions in the reference species are known. A defined environment can be realized, during the calibration procedure, by integration of a fluorescence cell in the experimental geometry. In noble gases such as Kr and Xe, two-photon laser induced transitions can be induced, which are spectrally close to the transitions of interest in O and N species of the investigated plasma flow. In Fig. 72, particle density measurements in an O plasma flow obtained using a noble gas calibration are shown for several discharge conditions, and are compared to the calibration technique using Rayleigh scattering.

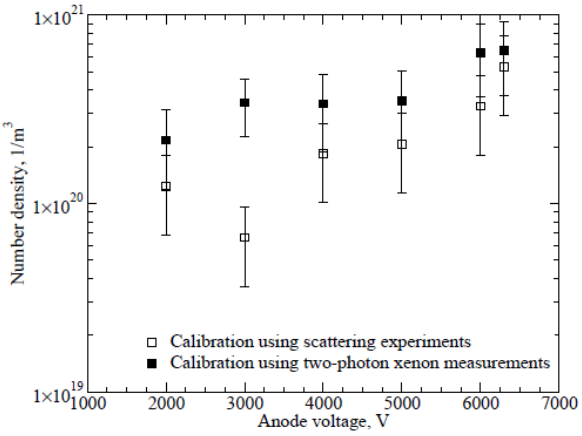

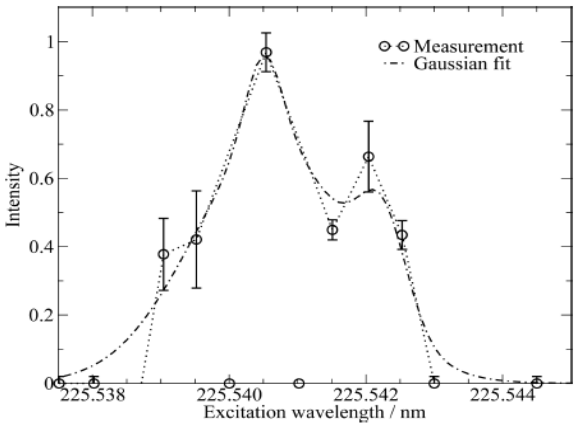

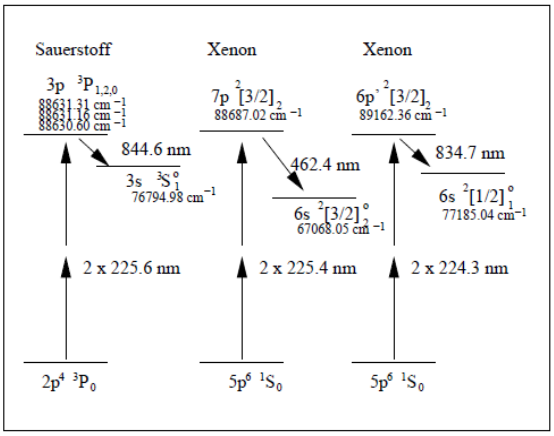

Figure 73:
Upper left: **Two-photon laser induced fluorescence measurements of atomic oxygen in the free stream of an oxygen plasma flow [66].**
Upper right**: Spectral absorption profile of the 2 x 225.6 nm two-photon transition in atomic oxygen. Fine structure components are of the excited levels can be partly resolved [66, 67].**
Left**: The applied excitation scheme in oxygen and two possible calibration schemes in xenon.**

ACKNOWLEDGEMENTS

THE AUTHORS WOULD LIKE TO THANK ALL COLLEAGUES INVOLVED IN THE DEVELOPMENT AND QUALIFICATION OF THE DIAGNOSTIC TECHNIQUES AT THE IRS DURING THE LAST DECADES

4.0 REFERENCES

[1] Beckwith, I. E., Harvey, W. D., Clark, F. L:, Comparisons of Turbulent-Boundary-Layer Measurements at Mach Number 19.5 with Theory and an Assessment of Probe Errors, NASA Technical Note TN D-6192, Langley Research Center; Hampton, VA. 23365, June 1971.

[2] M. Auweter-Kurtz, M. Feigl, M. Winter, "Diagnostic Tools for Plasma Wind Tunnels and Reentry Vehicles at the IRS", RTO Educational Notes 8, course on "Measurement Techniques for High Enthalpy and Plasma Flows", VKI Brussels, 1999.

[3] S. Laure, "Aufbau und Qualifikation von Versuchseinrichtungen zur Erzeugung von Hochenthalpie-Luftströmungen und deren Charakterisierung mittels mechanischer Sonden", Dissertation, Universität Stuttgart, 1998.

[4] H. Habiger, "Elektrostatische Sonden und Fabry-Perot Interferometrie zur Untersuchung von lichtbogenbeheizten Plasmen für Triebwerksanwendungen und Wiedereintrittssimulation", Dissertation, Universität Stuttgart, 1994.

[5] T. Stöckle, M. Auweter-Kurtz, S. Laure, "Material Catalysis in High Enthalpy Air Flows", AIAA-96-1904, 31st AIAA Thermophysics Conference, New Orleans, LA, 1996.

[6] T. Stöckle, S. Fasoulas, M. Auweter-Kurtz, "Heterogeneous Catalytic Recombination Reactions Including Energy Accommodation Considerations in High Enthalpy Gas Flows", AIAA-97-2591, 32nd Thermophysics Conference, Atlanta, 1997.

[7] S. Fasoulas, T. Stöckle, M. Auweter-Kurtz, "Measurement of Specific Enthalpy in Plasma Wind Tunnels Using a Mass Injection Probe", AIAA-97-2496, 32nd Thermophysics Conference, Atlanta, GA, June 1997.

[8] S. Löhle, A. Knapp, G. Herdrich, M. Auweter Kurtz, "Local Enthalpy Estimation in Plasma Flows Using an Improved Mass Injection Probe", AIAA-2009-7301, Hypersonics and Space Planes Conf., Bremen, 2009.

[9] J.N. Moss, "Reacting Viscous-Shock-Layer Solutions with Multi-Component Diffusion and Mass Injection", NASA TR R-411, June 1974.

[10] J.A. Fay, F.R. Riddell, "Theory of Stagnation Point Heat Transfer in Dissociated Air", Journal of Aeronautical Sciences, Vol. 25, No. 2, February 1958.

[11] N.S. Vojvodich, R.B. Pope, "The Influence of Ablation on Stagnation Region Convective Heating for Dissociated and Partially Ionized Boundary Layer Flows", Proceedings of the 1965 Heat Transfer and Fluid Mechanics Institute, Stanford University Press, California 1965;

[12] J.G. Marvin, R.B. Pope, "Laminar Convective Heating and Ablation in the Mars Atmosphere", AIAA Journal, Vol. 5, No. 2, February 1967;

[13] R.B. Pope, "Measurements of Enthalpy in Low Density Arc Heated Flows", AIAA Journal, Vol. 6, No. 1, January 1968.

[14] R.B. Pope, "Stagnation Point Convective Heat Transfer in Frozen Boundary Layers", AIAA Journal, Vol. 6, No. 4, April 1968.

[15] R. Goulard, "On Catalytic Recombination Rates in Hypersonic Stagnation Heat Transfer", Jet Propulsion, Vol. 28, No. 11, November 1958.

[16] G. Herdrich, M. Fertig, Catalysis of Metallic and Ceramic TPS-Materials, Paper 2008-e-18, 26th International Space Symposium on Technology and Science, Hamamatsu, Japan, 1.-8. Juni 2008, Trans. JSASS Space Tech. Japan, Vol. 7, pp.Pe_49-Pe_58 (2009).

[17] S. Pidan, M. Auweter-Kurtz, G. Herdrich, M. Fertig, Recombination Coefficients and Spectral Emissivity of Silicon Carbide-Based Thermal Protection Materials, Paper AIAA 2004-2274, 37th AIAA Thermophysics Conference, Portland, Oregon, USA, Juni/Juli 2004, Journal of Thermophysics and Heat Transfer, pp. 566-571, Vol. 19, No. 4, Okt.-Dez. 2005.

[18] G. Herdrich, M. Fertig, S. Lein, S. Löhle, A. Preci, A. Steinbeck, R. Wernitz, M. Auweter-Kurtz, Hans-Peter Roeser, Current Status of Instrumentation Developments at IRS: In-Situ Investigations and Airborne Measurement Campaigns, Acta Astronautica 66 (2010), pp. 1087–1098.

[19] S. Löhle, C. Eichhorn, A. Steinbeck, S. Lein, G. Herdrich, H.-P. Röser, M. Auweter-Kurtz, Oxygen plasma flow properties deduced from laser-induced fluorescence and probe measurements, Applied Optics Vol. 47, No.13, pp.1837-1845, 2008.

[20] A. Schönemann, M. Auweter-Kurtz, "Mass Spectrometric Investigation of High Enthalpy Plasma Flows", Journal of Thermophysics and Heat Transfer, Vol. 9, NO. 4, pp. 620-628, Oct.-Dec. 1995.

[21] A. Schönemann, "Massenspektrometrie zur Untersuchung lichtbogenbeheizter Plasmen in Niederdruck-Plasmawindkanal", Dissertation, Universität Stuttgart, 1994.

[22] T. Stöckle, M. Winter, M. Auweter-Kurtz, "Simultaneous Spectroscopic and Mass Spectroscopic Investigation of Surface Catalytic Effects in High Enthalpy Gas Flows", AIAA-98-2845, 7th AIAA/ASME Joint Thermophysics and Heat Transfer Conference, Albuquerque, NM, 1998.

[23] P. Dabalà and M. Auweter-Kurtz, "Mass Spectrometric Investigations of Erosion Behavior of Thermal Protection Materials", ESA 2nd European Workshop on Thermal Protection Systems, Stuttgart, October 1995.

[24] A. Schönemann, M. Auweter-Kurtz, "Characterization of Nitrogen and Air Plasma Flows by Mass Spectrometry", ISPC 11, Proceedings of the 11th International Symposium on Plasma Chemistry, Loughborough, UK, 1993, pp. 458-463.

[25] J.H. Batey, "Quadrupole Gas Analyzers", Vacuum 37/8, pp. 659-668, 1987.

[26] P. Dabalà, M. Auweter-Kurtz, "Mass Spectrometric Erosion Measurements of Ceramic Thermal Protection Materials in High Enthalpy Plasma", AIAA-97-2590, 32nd Thermophysics Conference, Atlanta, 1997.

[27] P. Dabalà, M. Auweter-Kurtz, "Investigation of the Erosion Behavior of Graphite and Silicon Carbide by Mass Spectrometry", 12th International Symposium on Plasma Chemistry, Minneapolis, 1995.

[28] Fasoulas, S., "Experimentelle und theoretische Charakterisierung einer hochenthalpen Stickstoffströmung zur Wiedereintrittssimulation", *Dissertation*, IRS, Univ. Stuttgart, Feb. 1995.

[29] Fasoulas, S., "Measurement of Oxygen Partial Pressure in Low Pressure and High Enthalpy Flows",

AIAA.96-2213, 19th Advanced Measurement and Ground Testing Technology, New Orleans, LA, 1996.

[30] Fasoulas, S.; Förstner, S.; Stöckle, T.: "Flight Test of Solid Oxid Micro-Sensors on a Russian Reentry Probe", AIAA 2001-4724, Space 2001 Conference & Exhibition, Albuquerque, NM, 2001.

[31] Schrempp, C.A., "Qualifikation von Festkörperelektrolytsonden zur Bestimmung des Sauerstoffpartialdrucks im Weltraum", Dissertation, IRS, Univ. Stuttgart, Feb. 2000.

[32] Sauer, M., "Entwicklung von Festkörperelektrolytsensoren zur Charakterisierung von Gaspartialdrücken und Massenströmen", Fortschr.-Ber., VDI Reihe 8 Nr. 876. Düsseldorf, 2001.

[33] Förstner, R.: "Entwicklung keramischer Festkörperelektrolytsensoren zur Messung des Restsauerstoffgehalts im Weltraum", Dissertation, Universität Stuttgart, 2003.

[34] Schmiel, T: "Entwicklung, Weltraumqualifikation und erste Ergebnisse eines Sensorinstruments zur Messung von atomaren Sauerstoff im niedrigen Erdorbit", Dissertation, TU Dresden, Sierke-Verlag, 2009.

[35] Ullmann, H., "Keramische Gassensoren", Akademie Verlag, Berlin, 1993.

[36] W. Nernst, "Über die elektrolytische Leitung fester Körper bei sehr hohen Temperaturen", Zeitschrift Elektrochemie, Nr.6, 1899, S. 41-43.

[37] Schmiel, T., Fasoulas, S., Heisig, J., Przybilski, O., "Time Resolved Measurement of Atomic Oxygen in Low Earth Orbit and its Benefits for Future Spacecraft Design", CEAS-2007-128, Proceedings of the 1st DGLR-CEAS European Air and Space Conference, Berlin, 2007.

[38] Hammer, F.: "Entwicklung eines miniaturisierten Festkörperelektrolytsensors aus der Raumfahrt zur Optimierung von Verbrennungsprozessen", Dissertation, Institut für Raumfahrtsysteme, Universität Stuttgart, 2001.

[39] Fasoulas, S. (Editor); Baumann, R.; Gläser, M.; Gritzner, C.; Hammer, F.; Heisig, J.; Kahle, R.; Kirschke, T.; Schmiel, T.; Völkel, M., et al.: Solid State Electrolyte Sensors for the Determination of Oxygen, Carbon Dioxide, and Total Flow Rates Associated to Respiration in Human Subjects, Executive Summary to ESA-ESTEC Contract No. 15450/01/NL/JS CNN 1+2, PRO2-FR-EXEC-SUM-05-02-10, TU Dresden, 2005.

[40] Hammer, F., Schmiel, T., Fasoulas, S., Messerschmid, E.: "From Space to Earth - a Novel Solid Electrolyte Oxygen Sensor System for In-Situ Measurement and Process Control", Advances in applied plasma science, Vol.7, 2009.

[41] S. Fasoulas, U. Hoffmann: Development and Application of a Miniaturised Sensor System for Respiratory Investigations (MAP-RSS), Abstract and Executive Summary to the Final Report to the ESTEC Contract No. 14350/01/NL/SH; TU Dresden; Deutsche Sporthochschule Köln (DSH), march 2008.

[42] Messerschmid, E., Fasoulas, S., "Verfahren und Vorrichtung zur simultanen Messung des Gesamtvolumenstroms und von Gaspartialdrücken", Patent DE000019542379A1, 1997.

[43] S. Fasoulas, et al., "New Miniaturized and Space Qualified Gas Sensors for Fast Response In Situ

Measurements", AIAA 2010-6147, 40th International Conference on Environmental Systems, 2010.

[44] H. Habiger, M. Auweter-Kurtz, "Investigation of High-Enthalpy Air Plasma Flow with Electrostatic Probes", Journal of Thermophysics and Heat Transfer, Vol. 12, No. 2, April-June 1998, S. 198-205; also AIAA-96-1864, 31st AIAA Thermophysics Conference, New Orleans, LA, June 1996.

[45] W. Röck, "Simulation des Eintritts einer Sonde in die Atmosphäre des Saturnmondes Titan in einem Plasmawindkanal", Dissertation, Universität Stuttgart, 1998.

[46] Herzberg, G., "Atomic spectra & atomic structure", Dover Publications , New York, 1944.

[47] Gerthsen, "Physik", Springer Verlag 1999.

[48] Eckbreth, A.C., Laser Diagnostics for Combustion Temperature and Species", Abacus Press, 1988.

[49] Smith, A.J., Gogel, T.H., Vandervelde, P., "Plasma Radiation Database PARADE", Final Report of the ESA/ESTEC TRP, Contract 11148/94/NL/FG, April 1996.

[50] Hellwege, K. H., "Einführung in die Physik der Molekeln", Springer-Verlag Berlin Heidelberg New York, 1989.

[51] Herzberg, G., "Molecular Spectra and Molecular Structure: Vol. I, Spectra of Diatomic Molecules, D. Van Nostrand Company, LTD, 1950.

[52] Laux, C. O., "Optical Diagnostics and Radiative Emission of Air Plasmas", HTGL Report No. T-288, Stanford University, CA, USA, August 1993.

[53] Röck, W., "Simulation des Eintritts einer Sonde in die Atmosphäre des Saturnmondes Titan in einem Plasmawindkanal", Dissertation, Fakultät Luft- und Raumfahrttechnik, Universität Stuttgart, 1998.

[54] Winter, M.W., Emissionsspektroskopische Untersuchung der Umströmung von Probenkörpern in hochenthalpen Plasmaströmungen", Dissertation, Universität Stuttgart, 2007.

[55] Habiger, H., "Elektrostatische Sonden und Fabry-Perot Interferometrie zur Untersuchung von lichtbogenbeheizten Plasmen für Triebwerksanwendungen und Wiedereintrittssimulation", Dissertation, Institut für Raumfahrtsysteme, Fakultät Luft- und Raumfahrttechnik, Universität Stuttgart, 1994.

[56] Löhle, S., Marynowski, T., Mezger, A., Fulge, H., „Spectroscopic Analysis of the Hayabusa Re-entry using airborne and ground based equipment", Workshop on Re-Entry Emission Signatures V", Brisbane, Australia, 2011.

[57] Löhle, S., Lein, S., Eichhorn, C., Herdrich, G., Winter, M., „Spectroscopic Investigation of an Inductively Heated CO_2 Plasma for Mars Entry Simulation" Journal of Technical Physics, in press.

[58] Löhle, S., Wernitz, R., Herdrich, G., Fertig, M., Röser, H.-P., Ritter, H., „Airborne Re-entry Observation Experiment SLIT: UV Spectroscopy during STARDUST and ATV1 Re-entry", CEAS Space Journal, DOI 10.1007/s12567-010-0005-3, 2010.

[59] Demtröder, "Laserspektroskopie", Springer Verlag.

[60] Nomura, S., Löhle, S., Knapp, A., Herdrich, G., Komurasaki, K., "Combined Laser Absorption Spectroscopy and Laser Induced Fluorescence in High Enthalpy Flow", 27th ISTS, Tsukuba, Japan,

2009.

[61] Eichhorn, C., Löhle, S., Fasoulas, S., Auweter-Kurtz, M., Journal of Thermophysics and Heat Transfer , Technical Note (2011), in prep.

[62] S. Löhle, „Untersuchungen von Wiedereintrittsplasmen mit Hilfe laserinduzierter Fluoreszenzmessungen“, Dissertation Universität Stuttgart, 2006.

[63] Goehlich, A., Kawetzki, T., Döbele, H.F., J. Chem. Phys. **108** (1998) 9362.

[64] Niemi, K., Schulz-von der Gathen, V., Döbele, H.F., J. Phys. D **34** (2001) 2330.

[65] Eichhorn, C., Fritzsche, S., Löhle, S., Knapp, A., Auweter-Kurtz, M., Physical Review E **81** (2009) 026401.

[66] Löhle, S., Auweter-Kurtz, M., Journal of Thermophysics and Heat Transfer **21** (2007) 623.

[67] Löhle, S., Eichhorn, C., Steinbeck, A., Lein, S., Herdrich, G., Röser, H.-P., Auweter- Kurtz, M., Applied Optics, **47** (2008) 1837.

[68] Battaglia, J.-L., Cois, O., Puigsegur, L., and Oustaloup, A., “Solving an inverse heat conduction problem using a non-integer identified model,” International Journal of Heat and Mass Transfer, Vol. 44, 2001, pp. 2671–2680

[69] Löhle, S., Battaglia, J.-L, Batsale, J.-C., Enouf, O., Dubard, J., Filtz, J.-R., “Characterization of a heat flux Sensor Using Short Pulse Laser Calibration”, in AIP Review of Scientific Instruments Vol. 78, 10.1063/1.2736388, 2007

[70] Löhle, S., Battaglia, Jullien, P., van Ootegem, B., Couzi, J., Lasserre, J.-P. “Improvement of High Heat Flux Measurements Using a Null-point Calorimeter”, in AIAA Journal of Spacecrafts and Rockets 45, Nr. 1, doi: 10.2514/1.30092, 2007

[71] Löhle, S., Battaglia, J.-L., “Transient Heat Flux Measurements in High Enthalpy Air Plasma Flows Using a Non-Integer System Identification Approach”, 41st AIAA Thermophysics Conference, San Antonio, TX, 2009